

UNCLASSIFIED

AD NUMBER

ADB005778

LIMITATION CHANGES

TO:

Approved for public release; distribution is unlimited. Document partially illegible.

FROM:

Distribution authorized to U.S. Gov't. agencies only; Test and Evaluation; JUN 1974. Other requests shall be referred to Air Force Avionics Laboratory, AFAL/TEA, Wright-Patterson AFB, OH 45433.

AUTHORITY

afal ltr, 27 feb 1979

THIS PAGE IS UNCLASSIFIED

**Best Available  
Copy  
for all Pictures**

THIS REPORT HAS BEEN DELIMITED  
AND CLEARED FOR PUBLIC RELEASE  
UNDER DOD DIRECTIVE 5200.20 AND  
NO RESTRICTIONS ARE IMPOSED UPON  
ITS USE AND DISCLOSURE.

DISTRIBUTION STATEMENT A

APPROVED FOR PUBLIC RELEASE;  
DISTRIBUTION UNLIMITED.

AFAL-TR-74-171

ADB00578

## MAGNETIC BUBBLE MEMORY

*ELECTRONICS RESEARCH DIVISION  
ROCKWELL INTERNATIONAL*

TECHNICAL REPORT AFAL-TR-74-171

JUNE 1974



DDC  
RECEIVED  
AUG 11 1975  
RECEIVED  
D

Distribution limited to U.S. Government agencies only; test and evaluation results reported: June 1974. Other requests for this document must be referred to AFAL/TEA, Wright-Patterson Air Force Base, Ohio 45433.

AIR FORCE AVIONICS LABORATORY  
AIR FORCE SYSTEMS COMMAND  
WRIGHT-PATTERSON AIR FORCE BASE, OHIO 45433



#### NOTICE

When Government drawings, specifications, or other data are used for any purpose other than in connection with a definitely related Government procurement operation, the United States Government thereby incurs no responsibility nor any obligation whatsoever; and the fact that the government may have formulated, furnished, or in any way supplied the said drawings, specifications, or other data, is not to be regarded by implication or otherwise as in any manner licensing the holder or any other person or corporation, or conveying any rights or permission to manufacture, use, or sell any patented invention that may in any way be related thereto.

Copies of this report should not be returned unless return is required by security considerations, contractual obligations, or notice on a specific document.

AIR FORCE/56780/22 July 1975 — 50

# MAGNETIC BUBBLE MEMORY

L. R. Tocci et al  
Electronics Research Division  
Rockwell International

DDC  
RECEIVED  
AUG 11 1975  
RECEIVED  
D

Distribution limited to U.S. Government agencies only.  
test and evaluation results reported: June 1974.  
Other requests for this document must be referred  
to AFAL/TEA, Wright-Patterson AFB, Ohio 45433.

## FOREWORD

The First Annual Report on the Magnetic Bubble Memory Program was prepared by the Electronics Research Division, Autonetics Group, Electronics Operations of Rockwell International, Anaheim, California, under Air Force Contract No. F33615-73-C-1103. It describes the work performed from 2 January 1973 to 1 March 1974. The first year of this program does not support materials or packaging efforts and except for permalloy studies and detector studies does not include device fabrication or device development areas. However, for completeness information on many aspects of bubble technology are included.

This contract is administered by the Memory Technology Group, Advanced Electronics Devices Branch, Electronics Technology Division, Air Force Avionics Laboratory, Air Force System Command, Wright-Patterson Air Force Base, Ohio. Project Engineer is Dr. Millard G. Mier AFAL/TEA. The contract was initiated under Project No. 6096, Task No. 609602. The report was submitted by the authors in April 1974.

The contractor's report number is C73-229.16/501. Publication of this report does not constitute Air Force approval of the reports' findings or conclusions. It is published only for exchange and stimulation of ideas.

The other major authors of this technical report are Mr. R. Bailey (Section 2), Dr. P. K. George (Section 5) Mr. J. Ypma (Para. 6.3), and Dr. D. Heinz (Appendix A and B). Acknowledgement for other contributions to this report are given to Drs. P. Besser and R. Henry (experimental results, Appendix D) and Mr. T. Steury (Appendix E). Special recognition and thanks is given to Mr. T. Oeffinger who gathered most of the data in Para. 6.1. Acknowledgement is also given to the other members of the Magnetic Devices Group, Dr. T. Chen, A. Campbell, J. Williams, D. Welch, and L. Garner for their support and contributions to this work and to the members of the Magnetic Circuits and Magnetic Systems Groups. Finally, special thanks is given to Mr. J. L. Archer for his support and direction.

This technical report has been reviewed and is approved for publication

PROJECT ENGINEER

*Dr. Millard G. Mier*

MILLARD G. MIER  
Research Physicist  
Memory Technology Group  
Advanced Electronic Devices Branch  
Electronic Technology Division

For the Commander

*Robert D. Larson*

ROBERT D. LARSON  
Chief, Advanced Electronic Devices Branch  
Electronic Technology Division  
Air Force Avionics Laboratory



UNCLASSIFIED

SECURITY CLASSIFICATION OF THIS PAGE (When Data Entered)

REPORT DOCUMENTATION PAGE		READ INSTRUCTIONS BEFORE COMPLETING FORM
1. REPORT NUMBER AFAL-TR-74-171	2. GOVT ACCESSION NO.	3. RECIPIENT'S CATALOG NUMBER
4. TITLE (and Subtitle)  MAGNETIC BUBBLE MEMORY		5. TYPE OF REPORT & PERIOD COVERED Interim Technical Report No. 1 2 Jan 73 - 1 Mar 74
		6. PERFORMING ORG. REPORT NUMBER C73-299.16/501
7. AUTHOR(s) L. R. Tocci et al		8. CONTRACT OR GRANT NUMBER(s) F33615-73-C-1103
9. PERFORMING ORGANIZATION NAME AND ADDRESS Electronics Research Division Rockwell International Anaheim, California		10. PROGRAM ELEMENT, PROJECT, TASK AREA & WORK UNIT NUMBERS  6096-02-15
11. CONTROLLING OFFICE NAME AND ADDRESS Air Force Avionics Laboratory AFAL/TEA-3 Wright-Patterson AFB, Ohio 45433		12. REPORT DATE June 1974
14. MONITORING AGENCY NAME & ADDRESS (if different from Controlling Office) SAME		13. NUMBER OF PAGES 116 pages
		15. SECURITY CLASS. (of this report) UNCLASSIFIED
16. DISTRIBUTION STATEMENT (of this Report) Distribution limited to U. S. Government agencies only; test and evaluation results reported: <del>September 1974</del> June 1974. Other requests for this document must be referred to AFAL/TEA, Wright-Patterson AFB, Ohio 45433		
17. DISTRIBUTION STATEMENT (of the abstract entered in Block 20, if different from Report)  SAME		
18. SUPPLEMENTARY NOTES		
19. KEY WORDS (Continue on reverse side if necessary and identify by block number) Bubble Domain      Temperature Annealing Bubble Memory      Epitaxial Garnet Magnetic Memory      Cylindrical Domain Bubble Device      Mass Memory		
20. ABSTRACT (Continue on reverse side if necessary and identify by block number) This report describes the progress made during the first year of this program and covers two major areas of investigation. The first one is a study of the temperature stress/anneal effects on the permalloy thin films that are used for the bubble propagation and detection elements. It has been found that the magnetic, electrical, and physical properties of the film vary significantly with temperature stress/anneal and deposition parameters. It is an objective of this study to optimize the film deposition parameters and to be able to (continued back)		

UNCLASSIFIED

SECURITY CLASSIFICATION OF THIS PAGE(When Data Entered)

to predict the failure modes for bubble devices by providing knowledge of the magnetic behavior of the thin films to accelerated thermal stress. Paralleling this effort is a task to develop passivation techniques as an in-process approach to protect the bubble device against corrosive environments. Emulsitone was tried unsuccessfully as a passivation film. Presently Dow Corning 709 is being tested.

The second major area of investigation is the development of bias field temperature compensating techniques using temperature dependent magnets. The temperature coefficient of the magnet is chosen and/or tailored to match the temperature coefficient of the bias field required to maintain a constant bubble diameter. In order that bubble strip-out and collapse do not cause the temperature limits, the characteristic length  $l$  of the material must be relatively temperature independent. In this case the temperature limits will be determined by the decreasing mobility and increasing coercivity at the low temperature limit and by decreasing wall energy at the high temperature limit. A 10 K bit bubble device (24  $\mu$ m period) fabricated on YEuTmGaIG has been operated at 100 kHz from -10°C to 75°C.

A review of bubble memory package concepts and techniques is given which covers many packaging areas that are being studied by Rockwell International.

A comparison of several thick and thin chevron bubble sensors is also made. Thin detectors have the highest sensitivity per bubble stretch; however, the detector current is limited by Joule heating. Of the thick types the full conductor shorted chevron was found to have the highest sensitivity. For two active bubble sensors in a bridge detecting 180 deg apart half conductor shorted chevron detectors are used which have slightly smaller sensitivities.

Except for the detector comparison no device development was performed on this program. Also no effort was made to develop or improve bubble materials for device applications.

UNCLASSIFIED

SECURITY CLASSIFICATION OF THIS PAGE(When Data Entered)

## CONTENTS

<u>Section</u>	<u>Page</u>
1. Introduction .....	1
2. Permalloy Temperature Stress/Anneal and Passivation Studies .....	3
2.1 Purpose of Stress/Anneal Studies .....	3
2.2 Annealing Results .....	3
2.3 X-Ray Analysis .....	4
2.4 X-Ray Standard .....	7
2.5 Permalloy Passivation .....	8
3. Temperature Compensation Techniques .....	17
3.1 Material Considerations .....	17
3.1.1 Temperature Dependence of Bubble Materials .....	17
3.1.2 Constant Diameter Considerations .....	19
3.2 Temperature Dependent Shunt Technique .....	20
3.3 Temperature Dependent Magnets .....	25
3.3.1 Temperature Effects on the Remnance .....	26
3.3.2 Available Magnets .....	26
4. Bubble Memory Packaging Techniques .....	33
4.1 Chip Substrate .....	33
4.2 Chip Bonding .....	34
4.3 Lead Bonding .....	36
4.4 Hermiticity .....	38
4.5 Laser Dicing .....	38
4.6 Rotating Field Network .....	38
4.7 Bias Field Structure .....	42
4.8 Package Concepts .....	42
5. Detector Study .....	49
5.1 Detector Output Tailoring .....	49
5.2 Detector Sensitivity .....	55
6. Bubble Memory Devices and Exerciser .....	57
6.1 Magnetic Bubble Memory Chip .....	57
6.1.1 Chip Description .....	57
6.1.2 Device Fabrication .....	62
6.1.3 Device Operating Characteristics .....	63



## CONTENTS (Cont)

<u>Section</u>	<u>Page</u>
6.2 Temperature Compensated Bias/Drive Structure .....	73
6.2.1 PM Bias Structure .....	76
6.2.2 In-Plane Field Coil .....	79
6.3 Bubble Memory Exerciser .....	87
6.3.1 Timing Generator .....	87
6.3.2 Data Processor .....	92
6.3.3 Interface Unit .....	94
7. References .....	95
Appendix A. Bubble Material Overview .....	97
Appendix B. Bubble Material Considerations for Constant Bubble Diameter .	101
Appendix C. Method of Determining the Magnetic Field of a Parallel Plate Structure .....	105
Appendix D. Temperature Properties of YEuTm <sub>65</sub> GaIG .....	109

## ILLUSTRATIONS

<u>Figure</u>		<u>Page</u>
2-1.	Magnetization and Resistivity of 2000 Å Permalloy (0.81 Fe -0.19 Fe) Films; as Deposited and Post-Anneal vs Sputter Deposit Rate . . . . .	5
2-2.	Logrithm of the Normalized Resistivity and Magnetization vs Annealling Temperature. . . . .	6
2-3.	Normal and Totally Deteriorated BSR Circuit . . . . .	9
2-4.	Enlarged Transmission Photomicrograph of Chevron Stretcher Detector Region of a BSR Circuit. . . . .	9
2-5.	Same Area as Figure 2-4 in Reflection. . . . .	10
2-6.	Dark Field Photomicrograph of Circuit in Figure 2-3. . . . .	11
2-7.	Transmission Photomicrograph of Circuit in Figure 2-3 . . . . .	11
2-8.	Iron K $\alpha$ X-ray Image of Totally Deteriorated Circuit . . . . .	12
2-9.	Nickel K $\alpha$ X-ray Image of Same Area as in Figure 2-8 . . . . .	12
2-10.	Chlorine K $\alpha$ X-ray Damage of Same Pattern Area as in Figure 2-8. . . . .	13
2-11.	Crazing Effects of Emulsitone Film Overcoating on Bubble Device Circuit on Garnet . . . . .	15
2-12.	Crazing Effects of Emulsitone . . . . .	15
2-13.	Crazing Effects of Emulsitone Film Overcoating of Bubble Circuit on Glass. . . . .	16
3-1.	Collapse and Stripout Limitations to Constant Bubble Diameter Compensation. . . . .	18
3-2.	Permeability Temperature Dependence of Carpenter "32" Type 1 Material . . . . .	21
3-3.	Stability Margin Temperature Dependence of YGdT <sub>m</sub> GaIG . . . . .	23
3-4.	Bubble Velocity vs Drive Field for YGdT <sub>m</sub> GaIG at 0°C and 50°C. . . . .	24
3-5.	Wall Energy Temperature Dependence for YGdT <sub>m</sub> GaIG. . . . .	24
3-6.	Bubble Diameter Temperature Dependence for YGdT <sub>m</sub> GaIG. . . . .	25
3-7.	Material Effects on Remnance <sup>(4)</sup> . . . . .	28
3-8.	Temperature Dependence of RARENET . . . . .	29
3-9.	Temperature Dependence of Some Barium Ferrite Compositions . . . . .	30
3-10.	Comparison of the RARENET Magnet and EuTm <sub>65</sub> Bubble Material Temperature Variation . . . . .	31
4-1.	Polyimid Beam Frame Package. . . . .	35
4-2.	Multi-Layer Polyimid Board . . . . .	36
4-3.	Flying Wedge (Ball-Wedge), Ribbon (Strap-Bond), and Stitch Bonding (Lap-Lap) Bonding Techniques . . . . .	37
4-4.	Flat Ferrite Coils . . . . .	39
4-5.	Ferrite Pole Structure . . . . .	40
4-6.	Strip Line Coils . . . . .	43
4-7.	PM Parallel Plate Bias Structure . . . . .	44
4-8.	Closed PM Bias Structure . . . . .	44
4-9.	Package Concept - 1 . . . . .	45
4-10.	Package Concept - 2 . . . . .	47

# ILLUSTRATIONS (Cont)

<u>Figure</u>		<u>Page</u>
5-1.	Experimental Results for the Conductor Shorted Chevron Detector of Figure 5-2 . . . . .	50
5-2.	Conductor Shorted Chevron Detector . . . . .	51
5-3.	Modified Conductor Shorted Chevron Detector . . . . .	51
5-4.	Magnetoresistance Output of Modified Conductor Shorted Chevron Detector at Low and High Drive Fields. . . . .	52
5-5.	Magnetoresistance Output of Modified Conductor Shorted Chevron Detector at Low and High Drive Fields . . . . .	52
5-6.	Magnetoresistance Output of Modified Conductor Shorted Chevron Detectors (Placed in the Same Bridge) Showing Output Variation Between Detectors of Registers One and Two. . . . .	53
5-7.	Magnetoresistance Output of Modified Conductor Shorted Chevron Detectors (Placed in the Same Bridge) Showing the Output Variation with Applied Field (Bits are in both Registers) . . . . .	54
5-8.	Magnetoresistance Output of Modified Conductor Shorted Chevron Detectors (Placed in same Bridge) Showing the Interaction Between Outputs from Different Registers (at High Drive Field) . . . . .	54
6-1.	10 K Bit Bubble Shift Register (24 $\mu$ m Period) . . . . .	58
6-2.	Device Board Detector Electronics . . . . .	62
6-3.	Device Board with 10 Kb Chip . . . . .	63
6-4.	Electromagnetic Z-Bias/Drive Structure . . . . .	64
6-5.	Consecutive Bit Propagation Margins. . . . .	65
6-6.	Consecutive Bit Propagation Margins vs Temperature . . . . .	65
6-7.	Operating Margin vs Temperature of a Device from a Different Bubble Wafer . . . . .	66
6-8.	Generator Pulse Amplitude and Pulsewidth Phase Margins . . . . .	67
6-9.	Annihilator Pulse Amplitude and Pulsewidth Phase Margins . . . . .	69
6-10.	Conductor Shorted Chevron Detector Output Signal; Bubble and No-Bubble. . . . .	70
6-11.	Detector Signal at Various Stages of Signal Processing. . . . .	71
6-12.	Detector Signal vs Current. . . . .	72
6-13.	Detector Signal vs Bias Field. . . . .	72
6-14.	Detector Signal vs Drive Field . . . . .	73
6-15.	Propagation Margin vs Start-up and Shutdown Direction . . . . .	74
6-16.	PM Bias/Drive Structure. . . . .	75
6-17.	PM Bias/Drive Structure with Top Cover and Plate Removed . . . . .	75
6-18.	PM Bias Assembly with Top Plate . . . . .	77
6-19.	Field Variation for Various Shunt Pin Arrangements . . . . .	78
6-20.	Shunt Pin Locations . . . . .	79
6-21.	In-Plane Field Component of the Bias Field . . . . .	80
6-22.	Coarse/Fine Tuning . . . . .	81
6-23.	Bias Field Variation with Decoupling Ferrite Plates . . . . .	82
6-24.	In-Plane Component of the Bias Field with Ferrite Plates . . . . .	83
6-25.	Temperature Variation of this PM Structure Bias Field . . . . .	85
6-26.	Coil Impedance vs Frequency . . . . .	86
6-27.	Front Panel Layout of the Clock Generator Bubble Domain Memory Exercisor . . . . .	88

## ILLUSTRATIONS (Cont)

<u>Figure</u>		<u>Page</u>
6-28.	Front Panel Layout of the Interface Unit . . . . .	89
6-29.	Front Panel Layout of the Data Processor Section . . . . .	90
6-30.	Bubble Domain Device Memory Exerciser Block Diagram . . . . .	91
6-31.	Bubble Domain Memory Exercisor . . . . .	92



## TABLES

<u>Tables</u>	<u>Page</u>
3-1. Maintaining a Constant Bubble Diameter . . . . .	19
3-2. Temperature Properties of Carpenter "32" . . . . .	22
3-3. Temperature Dependent Magnets . . . . .	27
4-1. Closed PM Bias Structure Field Uniformity . . . . .	44
5-1. Detector Sensitivity Study . . . . .	55
6-1. Designed and Measured Bias Parameters . . . . .	76
6-2. In-Plane Field Coil Characteristics . . . . .	84

## SECTION 1.

### INTRODUCTION

The Magnetic Bubble Memory Program is a three year program sponsored by the U.S. Air Force Avionics Laboratory to develop magnetic bubble memory technology and demonstrate its feasibility for use in Air Force memory applications. The program is divided into technology development and hardware with development emphasized in the beginning of the program. As a relatively new and promising technology the interest by the Air Force to be at the forefront of its development is understandable and commendable. Memory systems using magnetic bubbles will have several advantages which make them very desirable as replacements for present drum and disk memories, and in special cases, tape recorder memories. The foremost advantage is their reliability as a result of being totally electronic in nature having no moving mechanical components. Also, because of the very high intrinsic bit capacity of the memory material ( $>10^6$  bits/in<sup>2</sup>) large scale memories ( $10^6 - 10^9$  bits) will be relatively compact and low power. As a result of their compactness and simplicity the cost/bit is expected to be low after full production lines are established. Military users are especially excited about the nonvolatility of magnetic bubble memories and their inherent resistance to high levels of radiation.

This report covers the work performed during the first year (Phase I) of this program. It focuses primarily on technology development and has two main efforts. First is the study of temperature stress/anneal effects on permalloy (Section 2). Permalloy, which is a soft magnetic field film, is the primary element of the field access bubble device. It is used not only for the propagation patterns but also for the magnetoresistive bubble sensor. Thus, the effects of temperature, deposition techniques and parameters, and passivation techniques, which are all part of this effort are very important in determining the magnetic properties of the permalloy films.

The second major effort is the development of temperature compensating techniques to improve the operating temperature range of magnetic bubble memories (Section 3, and Para 6.2). Although temperature dependent shunts are discussed the technique using temperature dependent magnets in the bias structure is the one developed. The reason for this is that most of the better bubble garnet materials have negative temperature coefficients. The technique is limited because it can only compensate for bubble diameter variation by compensating the bias field. The bubble diameter is directly proportional to the characteristic length. Other bubble material parameters which affect the temperature operation of bubble device are the mobility  $\mu_w$ , the wall energy  $\sigma_w$ , and the coercivity. The improvement of the material temperature dependent properties is not part of this program.

Secondary efforts covered in this report are a review of bubble packaging (Section 4). Since RI has a significant level of effort in this area sponsored by in-house programs and others, this review covers primarily these efforts. Also included in this report is some initial results of detector studies which are to be carried out in Phase II of this program (Section 5).



Lastly, this report discusses the bubble hardware fabricated on this program and delivered to the Air Force (Section 6). The hardware consists of ten 10K bit bubble devices fabricated on YEuTm.<sub>65</sub> GaIG bubble material having 6 $\mu$ m bubble diameters and bias/drive structures employing electromagnetic bias coils or temperature compensated permanent magnet bias structures. A magnetic bubble domain exerciser capable of operating single or quadrature shift registers or major minor loops is also provided on this phase of the program.

## SECTION 2

### PERMALLOY TEMPERATURE STRESS/ANNEAL AND PASSIVATION STUDIES

#### 2.1 PURPOSE OF STRESS/ANNEAL STUDIES

The objective of this study phase is to investigate the stability parameters of the soft magnetic thin films of permalloy (81% Ni +19% Fe) which are the heart of the bubble domain device circuit. The measurement of the stability of the permalloy films is necessary for two reasons: (1) the stability will be dependent upon the process parameters of the deposition of the thin permalloy films and of the subsequent pattern forming techniques used to place the magnetic circuit on the bubble domain device. Stability measurements will enable the optimization of the film deposition and pattern forming parameters, and (2) stability data will enable the prediction of failure modes for these devices by providing knowledge of the magnetic behaviour of the thin film material during accelerated stress experiments. The performance behaviour of the film magnetic parameters is required data for extrapolation to the performance of the microscopic permalloy circuit element behaviour.

This phase of the study is to perform accelerated stress tests and to observe the degradation of the permalloy films. The problem in the analysis of the parameter performance data from accelerated stress tests is to predict the effect of the individual parameters' degradation on the total device performance under normal stress conditions. This prediction will be based on an extrapolation of data generated in several acceleration stress tests, each run at different stress levels. Extrapolation always leads to the question of whether true extrapolation has been achieved. It is important to ascertain that this extrapolation does not contain a failure mechanism which is unimportant or non-existent in a normal stress condition. These stress experiments will consist of annealing steps designed to isolate the more sensitive degradable magnetic parameters of the permalloy films, derive the relationships between the behaviour of the physical properties of the film and its magnetic properties and relate the magnetic parameters' degradation in the film state to the behaviour of the actual operating devices on accelerated stress test series.

The permalloy stability experiments are designed to include all the pertinent magnetic (e.g.  $H_c$ ,  $4\pi M$ , magnetoresistivity), electrical (resistivity ( $\rho$ )) and physical parameters (crystallinity, microstrain, orientation). In addition to temperature step stress anneal studies, passivation feasibility of the permalloy film elements will be investigated (Para 2.5). Initially, the passivation experiments will include resistance to air ambient oxidation at elevated temperatures and a corrosion resistance test to determine the effectivity of the selected passivation technique to resist permalloy degradation in an accelerated corrosive atmosphere.

#### 2.2 ANNEALLING RESULTS

Initially, six groups of permalloy films (2000Å) were sputter deposited at ambient temperature on 7059 glass substrates at various deposition rates (2Å/sec to 10Å/sec). These films were characterized mechanically, electrically and magnetically in the as-deposited state and after each anneal step in a step anneal program. The films were annealed in a nitrogen ambient for a 20-hour period over the temperature range of 150 C to 350 C in 50 C intervals. The results of the anneal experiment are

shown in Figures 2-1 and 2-2. (The coercivity and anisotropy fields exceeded the measurement capability of our M-H loop apparatus, ~20 Oe, after the 250 C anneal step).

Note that these films still show a dependence upon the deposition rate through the final 350 C anneal step as shown in Figure 2-1. Figure 2-2 is an Arrhenius plot of the logarithm of the saturation magnetization ( $M_{si}$ ) and equivalent bulk resistivity ( $\rho_i$ ) normalized to their as-deposited values vs the anneal temperature. These plots represent averages, at each anneal step, of all six films. The temperature range up to 300 C shows that a single activation process exists vs the film anneal temperature. This is probably a defect anneal mechanism. For the saturation magnetization, the activation energy (average) is ~0.08 eV up to 300 C. Above 300 C a distinctly new mechanism is evident. This is thought to be a microsegregation and film restructuring taking place. In future experiments temperatures above 300 C will not be used since this is not a foreseeable normal environment for the permalloy circuit elements.

### 2.3 X-RAY ANALYSIS

Preliminary X-ray analysis of permalloy films was begun in an attempt to determine the functional dependence of the magnetic parameter on thickness vs stability. The analyses, using X-ray techniques, closely parallels that of Gangulee.<sup>1,2</sup> Two thick (500 Å) film sets of permalloy were sputter deposited on 7059 glass. One set (No. 320) was deposited at a low rate (3 Å/sec) and ambient temperature, and the other (No. 322) deposited at a high rate (10 Å/sec) and elevated substrate temperature (350 C).

The results of the preliminary X-ray diffraction analysis of these films can be summarized as follows:

1. In the as-deposited state, samples No. 320 and No. 322 shown marked differences in their diffraction peak heights. There are also differences in the peak breadths (peak width at the background line) but this is difficult to quantify because of a relatively high background X-ray intensity.
2. After annealing (350 C for 60 hr) the X-ray spectra show increased diffraction peak heights and possibly a reduction in peak breadth. However, the patterns of these two samples remain as easily distinguishable as they were prior to annealing.

The differences in peak height may indicate differences in preferred orientation or in the ratio of crystalline to amorphous volume fractions. The breadth of the peak will indicate microstrain, stacking fault density (including twinning), and particle size effects. A detailed analysis of peak shapes is required to distinguish between the various possible structural origins of these qualitative data. The marked differences between the patterns (both pre- and post-anneal) give a high degree of confidence that peak analysis would yield meaningful results. In order to perform this analysis, the background X-ray intensity must be reduced.

1. A. Gangulee, "The Structure of Electroplated and Vapor-Deposited Copper Films," J. A. P., 43 (1972).
2. A. Gangulee, "The Structure of Electroplated and Vapor-Deposited Copper Films. II Effects of Annealing," J. A. P. 43 (1972).

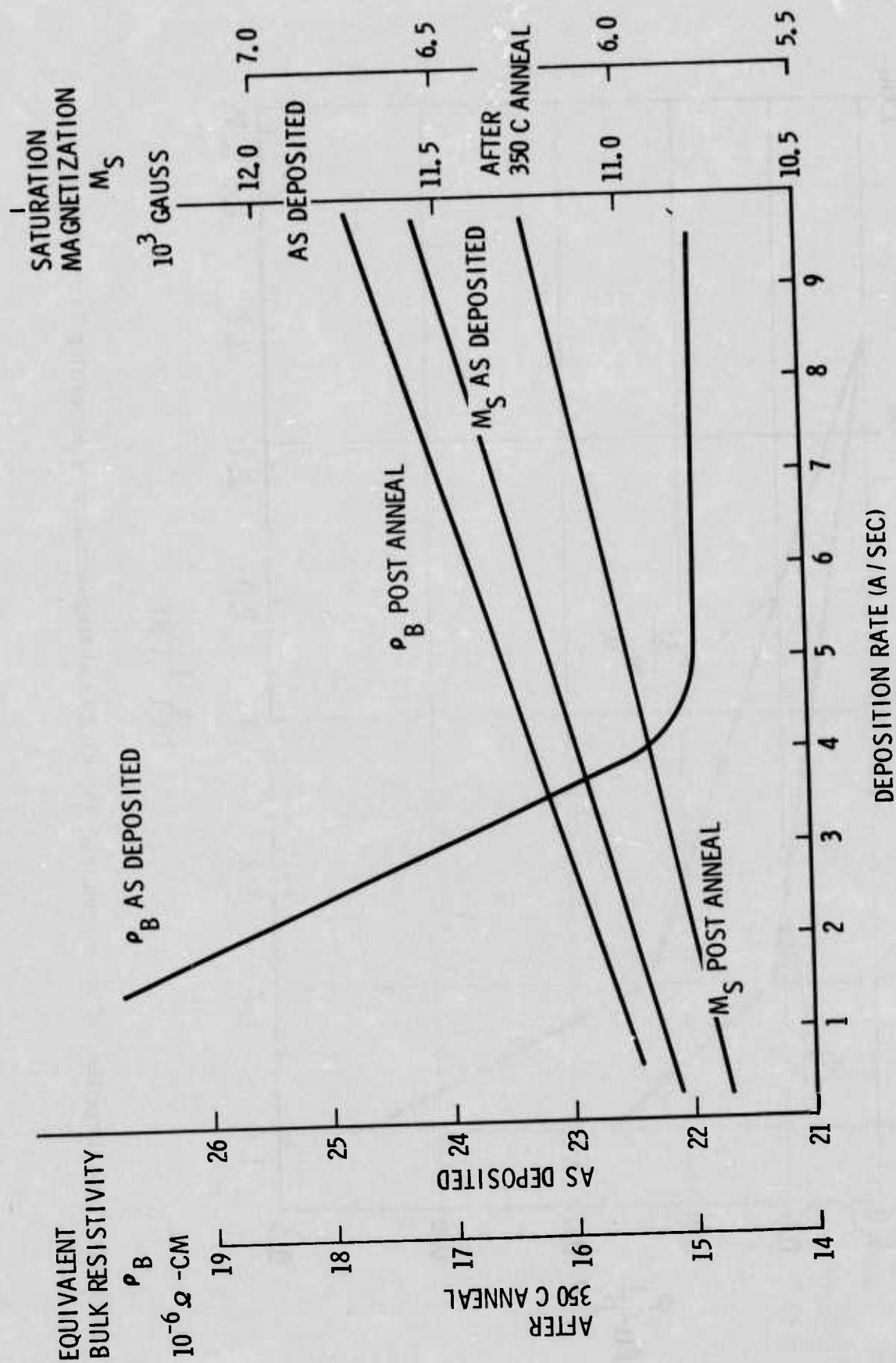


Figure 2-1. Magnetization and Resistivity of 2000 Å Permalloy (0.81 Fe - 0.19 Fe) Films; as Deposited and Post-Anneal vs Sputter Deposit Rate

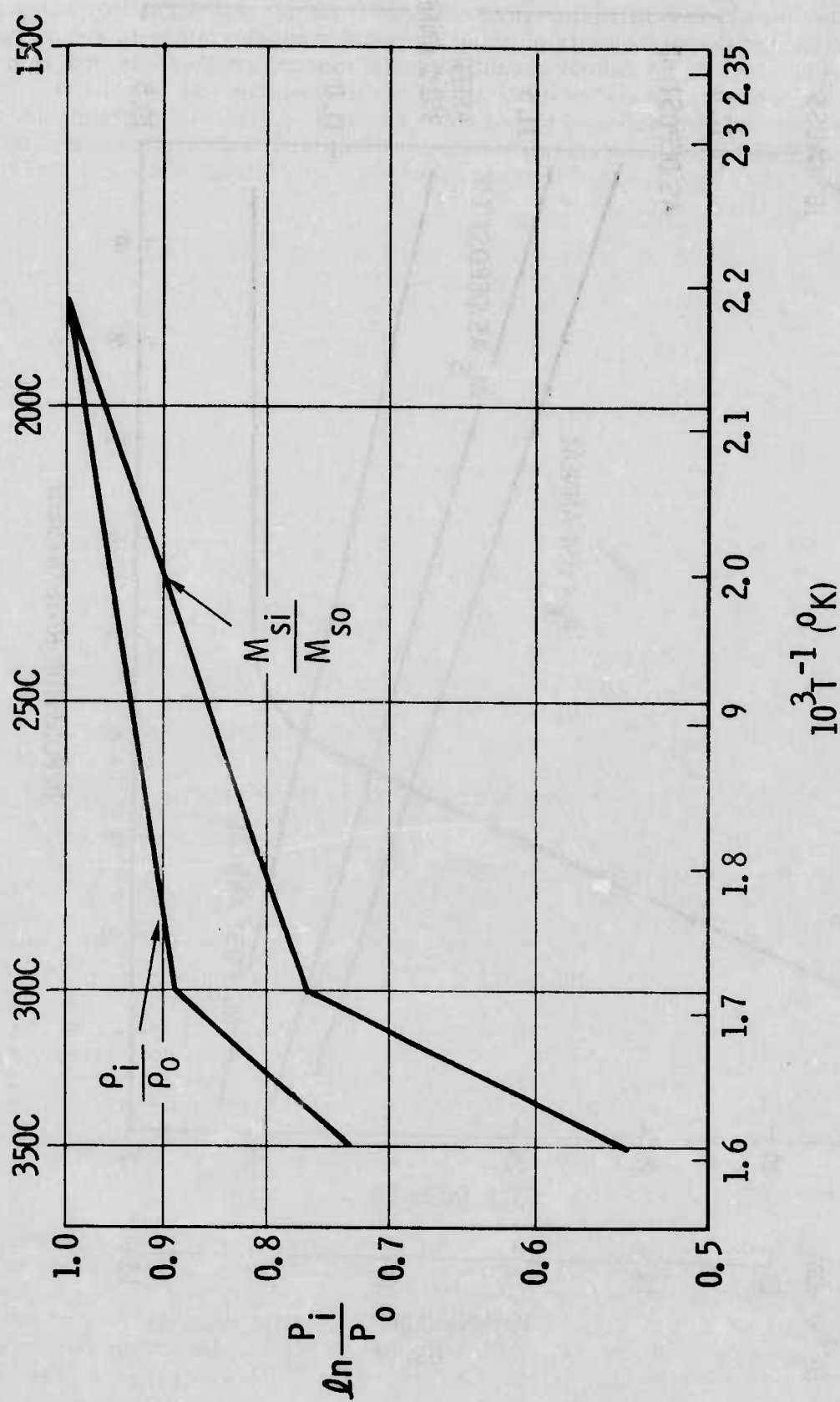


Figure 2-2. Logarithm of the Normalized Resistivity and Magnetization vs Annealing Temperature



Preliminary X-ray diffraction data obtained from several permalloy samples have demonstrated the advisability of using a crystal monochromator to reduce background intensity levels. A curved graphite crystal monochromator was ordered. While awaiting delivery, a review of data analysis procedures was conducted. These procedures involved correction of the data for removal of systematic errors and the subsequent calculation of the several parameters required to determine macrostrain, microstrains, stacking fault probabilities, particle size distributions, and preferred orientation effects.

The peak analysis will be applied in conjunction with isochronal and isothermal anneal experiments in order to quantify the nature of the anneal effects on permalloy films. These series will begin as soon as the X-ray techniques have been satisfactorily established.

The computer program for Fourier analysis of the diffraction peaks has been written and has been tested. The program successfully performs the basic Fourier analysis.

#### 2.4 X-RAY STANDARD

To follow structural changes with the annealing of sputtered NiFe films, it is necessary to have a suitable reference standard. Although glass is used conventionally, a specific substrate material has not been determined; therefore, films of permalloy approximately 2.4 microns thick, were sputter deposited on different substrates. The substrate materials under investigation were glass, silicon (111) with a 5000 Å thermal oxide, gadolinium gallium garnet (111) and sapphire (1102). After the initial deposition the films were annealed at 290°C in vacuum for 13 hr. After each annealing cycle, the structure of the films were characterized from X-ray diffraction data obtained with a conventional Norelco X-ray diffractometer using copper radiation monochromatized with a curved graphite crystal. A series of diffraction peaks, both first and second order reflections, were obtained for these films. The individual peaks were scanned at speed of 1/4° (2θ) per min in order to detect any changes in the shape of the peaks. The samples were then vacuum annealed at 290 C three more times and the X-ray analysis repeated after each individual annealing treatment for a total of 147 hours. The permalloy films were examined after each annealing treatment. With the exception of sapphire, an X-ray pattern of a polycrystalline material was obtained on each of the other substrates. After the second annealing period, there appeared to be no change in the shape of the lines (as determined by visually comparing the shape before and after each annealing cycle). On the sapphire substrate, the absence of X-ray diffraction peaks could indicate either a totally amorphous film or a perfect single crystal film. The single crystal film can be ruled out since the magnetic properties of this film on sapphire were identical to the rest of the permalloy films on other substrates. A single crystal film would imply excessively high coercivity. One weak peak that appears could correspond to the (111) reflection of the NiFe film.

Conventional Laue back reflection photographs were taken of three of the samples after the fourth annealing cycle. (The silicon specimen was eliminated because the sample was broken during the final annealing cycle). Polycrystalline (111) rings were obtained from films on both the glass and gadolinium garnet substrates. The uniformity of the rings denotes a high degree of crystalline isotropy, in other words no preferred in-plane orientation. The single crystal pattern of the GGG substrate can also be seen.



The pattern obtained on the sapphire sample showed a small segment of an incomplete ring which could indicate that there is preferred orientation in the sample after annealing. Once suitable standards are obtained, the broadening and shifting of the diffraction peaks of test samples will be analyzed by Fourier methods to determine the nature and distribution of defects as a function of deposition conditions and thermal treatments. The nature of the permalloy films as deposited in our laboratory can be summarized as being mono-crystalline with a strong preference for the (111) to be normal to the film plane. The film crystallites however, possess complete random orientation in the plane of the film.

When it is established that a suitable reference standard has been achieved, permalloy films (4000 Å) with widely different magnetic properties will be examined on the diffractometer during a series of isochronal anneal steps. The films will be sputtered at deposition rates ranging from 1.5 to 7 Å/sec. and deposited onto substrates at temperatures ranging from 100-300°C.

Detailed annealing experiments will be performed in the range 100-300°C intervals, each anneal being 12 hours duration, on the permalloy films. Results of the diffractometer measurements will be correlated with magnetic and electrical measurements.

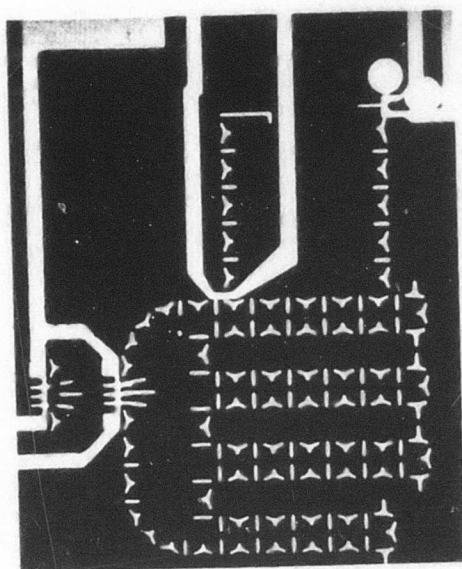
## 2.5 PERMALLOY PASSIVATION

The purpose of this portion of the permalloy effort is to address the question of how to achieve an isolation of the NiFe (permalloy) circuit film pattern from deleterious effects of a gaseous ambient. It is evident that a vacuum or a nonreactive ambient, e.g. argon, would provide isolation from corrosive attack on the permalloy by e.g. oxygen. However, this would require a hermetic package seal. The emphasis here is to investigate the feasibility of an in-process fabrication technique which would serve the dual purpose of protecting the bubble device from physical damage as well as chemical corrosion.

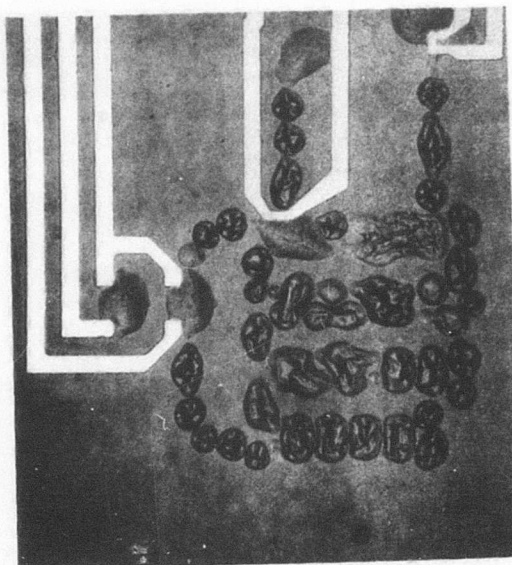
In several instances, there was observed on nonpassivated bubble permalloy propagation circuits a phenomena where the permalloy elements became jelly-like in appearance and essentially transparent. It appeared to spread in the permalloy element, in time, as if spreading like a disease. Eventually the entire element lost its metallic appearance. It did not seem to be any large area effect since neighboring elements of a contaminated element could survive for a much longer period, intact, indeed even surrounded by completely "diseased" elements.

An example this plague can be seen in the bubble circuit shown in Figure 2-3. Figure 2-4 and 2-5 show enlarged photomicrographs of a chevron stretcher detector. Notice from the transmission photo in Figure 2-4 that the effect appears to start at the boundary of an element and progress toward the center. Note also that there are several uncontaminated elements in a sea of contaminated permalloy.

This deterioration was termed as the permalloy "plague". When observed, the "plague" would usually have occurred within several days to a week after the circuit fabrication had been completed. It also appeared to be accelerated in the presence of sunlight such as might happen when a circuit was left on a desk near a window for



(a) Normal BSR Circuit



(b) Totally "Plagued" BSR Circuit

Figure 2-3. Normal and Totally Deteriorated BSR Circuit  
(Reflection Photomicrograph)



Figure 2-4. Enlarged Transmission Photomicrograph of Chevron  
Stretcher Detector Region of a BSR Circuit



Figure 2-5. Same Area as Figure 2-4 in Reflection

several days. Initially it was noticed that the "plague" occurred only on devices fabricated on garnet. This led to the theory that the sputter deposited  $\text{SiO}_2$  was the culprit since other than the  $\text{SiO}_2$ , the circuit fabrication technology is the same for garnet and glass. However, subsequent experiments produced the "plague" result on glass hence dispelling this theory.

The normal sample bubble circuit shown in Figure 2-6 was processed on glass, without the  $\text{SiO}_2$  spacer film but otherwise treated as if it were on garnet. This circuit eventually exhibited the "plague" and suffered total deterioration as shown in Figure 2-7. The permalloy pattern track path is clearly evident but any resemblance to the permalloy elements has completely disappeared. Figure 2-8 is a dark field photo of the Figure 2-7 pattern showing that the "plague" is a 3-dimensional feature. (The scattered cloud effect in the background of Figure 2-6 is caused by the 7059 glass on which the circuit is deposited.) Figure 2-7 is a transmission photomicrograph of Figure 2-7. Observe that the "plague" material is at least translucent and the deterioration is indeed complete.

The completely deteriorated permalloy pattern of that shown in Figure 2-7 was analyzed using an electron beam microprobe. The significant results are shown in Figures 2-8, 2-9, and 2-10. These photomicrographs of the back scattered X-rays are not quantitative. All possible, logical impurities were candidates, however, only chlorine was found. Note that the Cl pattern is confined to the propagation track.



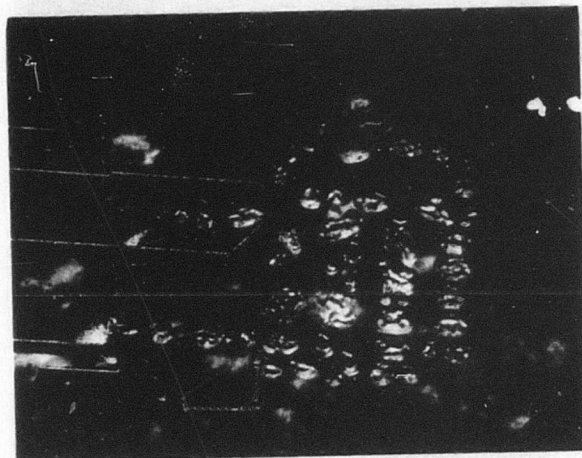


Figure 2-6. Dark Field Photomicrograph of Circuit in Figure 2-3.

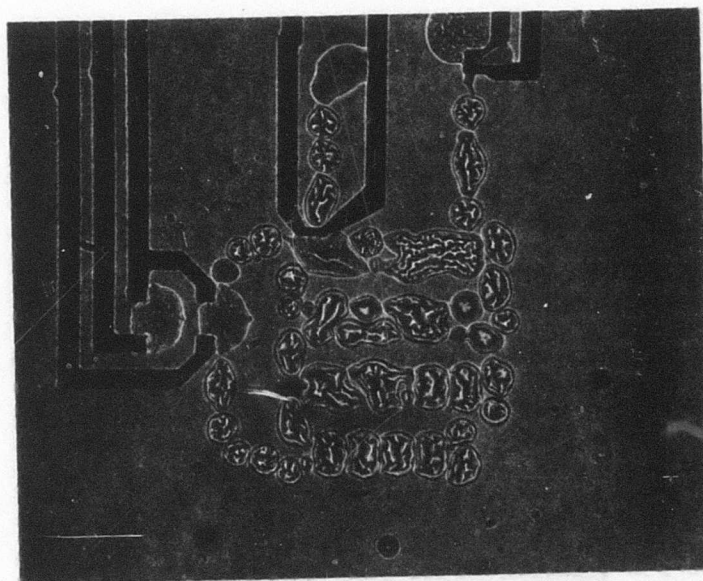


Figure 2-7. Transmission Photomicrograph of Circuit in Figure 2-3

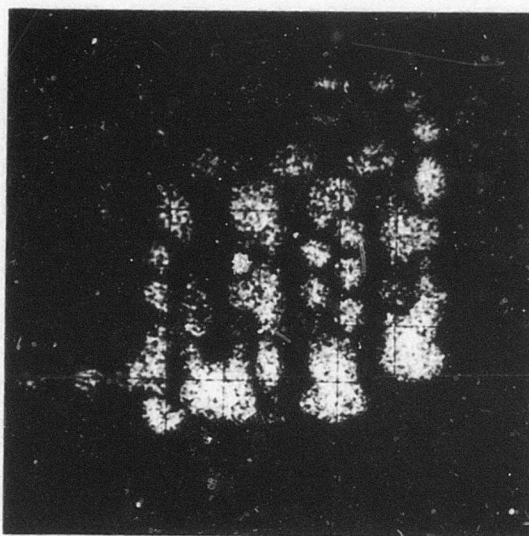


Figure 2-8. Iron  $K_{\alpha}$  X-ray Image of Totally Deteriorated Circuit (Identical to Figure 2-3)

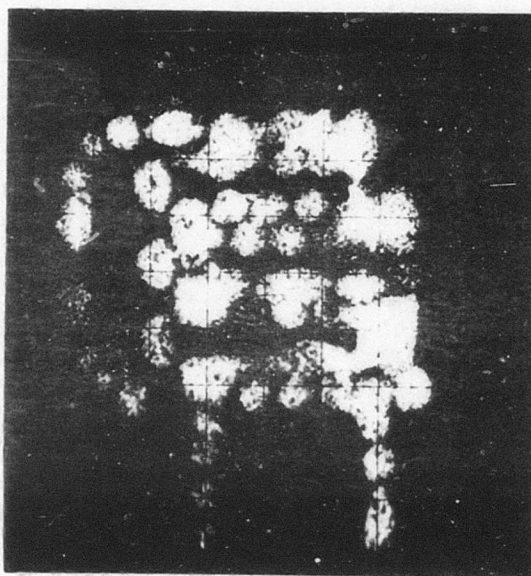
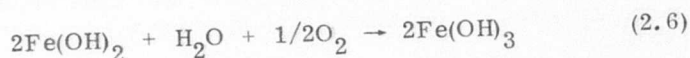
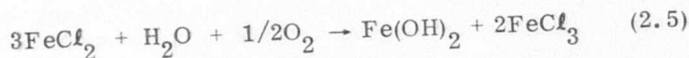
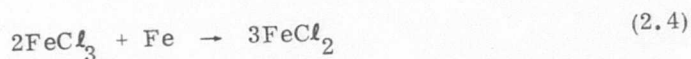
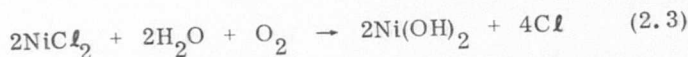
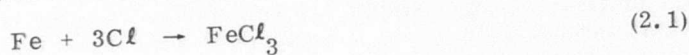


Figure 2-9. Nickel  $K_{\alpha}$  X-ray Image of Same Area as in Figure 2-8



Figure 2-10. Chlorine  $K_{\alpha}$  X-ray Damage of Same Pattern Area as in Figure 2-8

Semi-quantitative data concludes that the amount of  $Cl$  present is  $\leq 1$  percent of the  $Fe+Ni$  species. There are no  $Fe$  or  $Ni$  compounds of  $Cl$  which can react to completion comprising only  $\sim 1$  percent  $Cl$ . However, it is possible for the chlorine to act as a catalyst. The following scheme is proposed as the plague mechanism:



Eq (2.3) and (2.6) are terminal reactions insofar as the  $Ni(OH)_2$  and  $Fe(OH)_3$  are stable products. Eq (2.3) releases the  $Cl$  to be recirculated through the process starting at step (2.1). Eq (2.5) provides a source of ferric chloride to continue the consumption of the iron component.



The oxygen, water and hydroxide radical are available through the air and moisture vapor in the air. The chemical reaction is a relatively slow process but note that the Cl component can be cycled through the reaction equation until the free Ni and Fe components are completely exhausted. At this point, the Cl is not needed, and is merely trapped. This same substrate was heat treated at 150°C for 24 hours, in air, and reprobed for Cl. The Cl was completely absent, yet the "plague" had not changed in appearance. Chemical references state that  $\text{NiCl}_2$ ,  $\text{FeCl}_2$ ,  $\text{FeCl}_3$ ,  $\text{NiI}_2$ ,  $\text{FeI}_2$  are soluble in alcohol warm solutions of each and no effect was noted. However,  $\text{Ni(OH)}_2$  and  $\text{Fe(OH)}_2$  are readily attacked by acids. A plagued pattern was cleanly removed by dilute  $\text{HNO}_3$ .

The source of the chlorine was concluded to be the trichloroethylene used as a solvent at various times in the substrate process scheme. It was used specifically in the vapor degreaser to remove the wax used to mount the substrates, as might be necessary for a dicing operation. The hot trichloroethylene vapor need only dissociate to a minute fraction to provide the chlorine quantity observed in the microprobe results. In any event, this is only recognizable source of chlorine in the process. Subsequently, the use of TCE was discontinued where permalloy films are present. The elimination of all possible sources of chlorine has coincided with the absence of occurrences of the "plague".

The plague described here is one instance where the bubble circuit requires protection or passivation from external conditions. This part of the program is directed toward developing passivation techniques for bubble circuits. Emulsitone is one of the possible passivation materials. Our attempts to use Emulsitone as a passivation agent were not successful. Figures 2-11 through 2-13 are typical examples of the results. These figures shown permalloy circuits on garnet and glass upon which an Emulsitone film had been spun and cured at 100°C for 60 min. The films were applied at 2000 rpm and resulted in a 1400 Å thick oxide. At this stage the films still looked good with no evidence of the crazing. However, after dicing, subsequent die cleaning (to remove the protective photoresist layer) with acetone resulted in the effects shown in Figures 2-11 through 2-13. It is conjectured that the small thermal shock due to immersion in the acetone resulted in the crazing of the Emulsitone oxide. Obviously, the films cure in a high tensile stress state. That such an innocuous step as acetone immersion could produce this result has led us to abandon any further attempts to use Emulsitone as a passivating agent.

For the present, the passivation study will be limited to the use of Dow Corning 709. The permalloy films will be subjected to an isothermal step stress at 100°C in air and corrosion step stress in a saturated atmosphere above a solution of 0.1 N HCl maintained at 90°C. The HCl solution was chosen because of the highly reactive nature of the Cl and  $\text{H}_2\text{O}$  vapor with the permalloy at elevated temperatures, as noted in the previous discussion. Of course, samples of unpassivated permalloy films will provide the necessary experimental control conditions against which to gauge the behaviour of the passivated films.

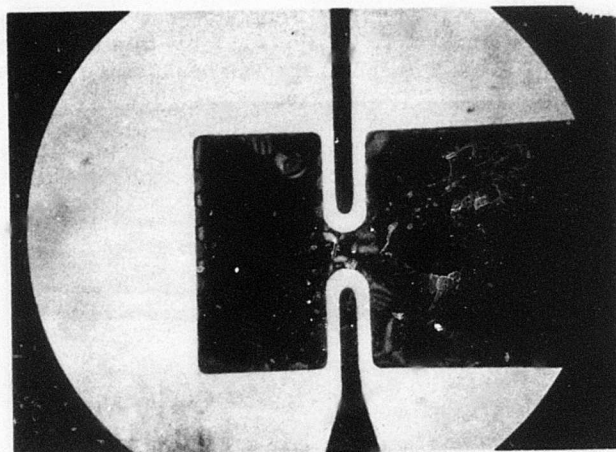


Figure 2-11. Crazing Effects of Emulsitone Film Overcoating  
on Bubble Device Circuit on Garnet

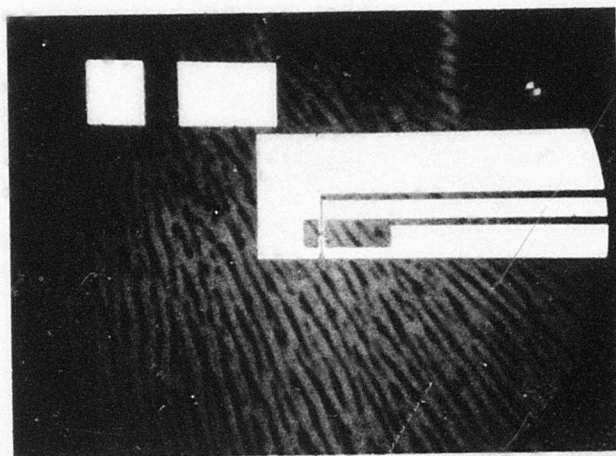


Figure 2-12. Crazing Effects of Emulsitone (Same as Figure 2-11)

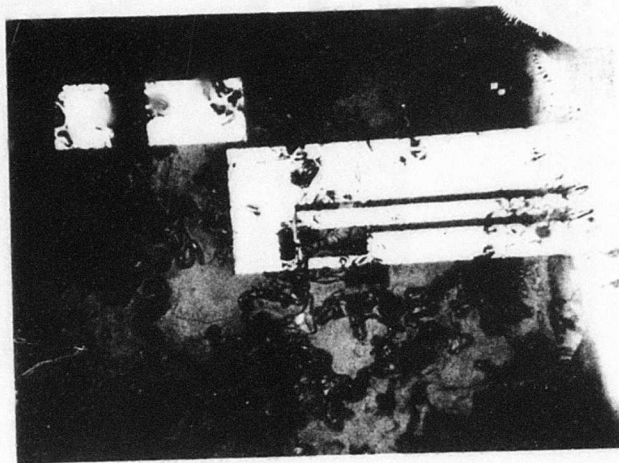


Figure 2-13. Crazing Effects of Emulsitone Film Overcoating  
of Bubble Circuit on Glass

### SECTION 3. TEMPERATURE COMPENSATION TECHNIQUES

In military applications magnetic bubble memories will be required to operate over wide temperature ranges while maintaining nonvolatility under zero power conditions. Permanent magnet bias structures can be used to maintain the dc bias field necessary for nonvolatility; however, without temperature compensating techniques the temperature variations of present bubble materials (especially bubble size variations) limit device operation to narrower temperature limits than would be obtained if the diameter remains constant. It is a goal of this program to develop the temperature compensating techniques which maintain a constant bubble diameter and increase the temperature operating range. The desired device operating temperature range is  $25^{\circ}\text{C} \pm 50^{\circ}\text{C}$ ; however, as bias field compensation can only compensate for bubble diameter variation and not other material parameter variations (Appendix A and B) operating ranges this wide will only be attainable as improvements in material temperature dependences are made.

Two zero power temperature compensating techniques which were considered were the temperature dependent shunt and the temperature dependent magnet techniques. The shunt technique can principally be used with bubble materials having positive temperature coefficients while the T-dependent magnet approach is principally used with negative temperature coefficient materials. The two techniques, of course, could be combined to give added flexibility in tailoring the temperature coefficient of the bias structure. Tailoring can also be accomplished by combining magnets having different temperature coefficients.

Although it appears that less temperature dependent materials will not have positive temperature coefficients the shunt technique will be described for completeness. However, before the bias compensation techniques are discussed some material considerations which effect the device temperature operating limits will be presented.

#### 3.1 MATERIAL CONSIDERATIONS

Bubble material parameters are temperature dependent and will affect the operating range of bubble devices. In this section an overview of the temperature dependence of bubble materials is given. A more complete discussion with experimental results focusing on the composition  $\text{YEuTm}_{.65}\text{GaTG}$  is presented in Appendix D. Also presented in this section is a summary of the material considerations which apply to temperature stable device operation.

##### 3.1.1 Temperature Dependence of Bubble Materials

For a particular device pattern period the bubble diameter must be maintained close to its optimum value which is in the neighborhood of one-quarter of the pattern period. In general the domain diameter is temperature dependent (Figure D-1, Appendix D) being determined by the characteristic length and the ratio of the bias field and the magnetization. If the diameter drifts too far from its optimum values the device operating margin will narrow resulting in increased error rates.

For a particular material a bias field variation exists which can maintain a constant bubble diameter with temperature (Figure D-3, Appendix D). The temperature range over which the bias field can be compensated is limited by the temperature



variation of the collapse and stripout bubble diameters (Figure 3-1). If the bubble size is at the center of this margin at temperature  $T_0$ , the upper temperature limit is determined by bubble collapse at  $T_u$ . Similarly the lower temperature limit  $T_l$  is determined by bubble stripout. Device operation will degrade when the collapse and stripout points are approached, thus the operating temperature range may even be smaller than that shown in Figure 3-1.

Even though the diameter variation can be compensated by varying the bias field it is essential to improve the basic temperature variation of the bubble stability margins. When this is achieved as in the case of YEuTm compounds (Appendix D) the temperature operation becomes limited by other materials parameters which cannot be compensated for by simple bias field compensation techniques. As Figure D-6, Appendix D, illustrates the bubble velocity for a given drive field decreases as the temperature decreases. Thus the possibility exists that at the lower temperature the material may become mobility limited for a given device operating data rate. This failure determines the lower temperature limit. The high temperature limit is determined by the wall energy which decreases as the temperature increases. As can best be determined at the present time wall energies of 0.1 ergs/cc or greater are required for reliable device operation. Thus when the wall energy falls below this value the possibility of spontaneous domain nucleation or stripping on the permalloy pattern may occur. To obtain temperature operating margins beyond that obtainable using temperature compensation, materials with less temperature sensitive parameters will have to be developed. This task is complicated not only by higher mobility requirements but also by dynamic conversion effects which are not well understood at the present time (see Appendix A).

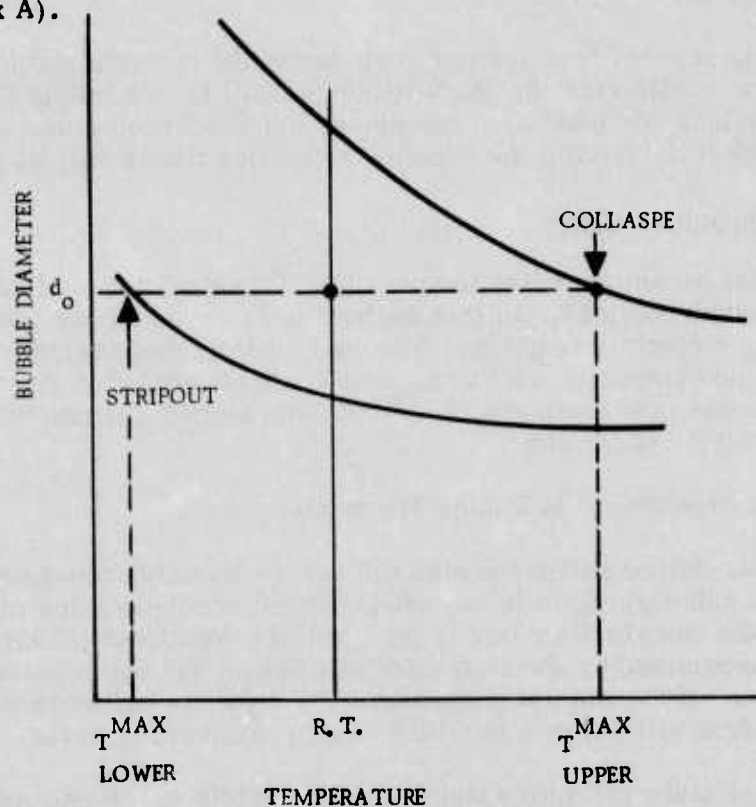


Figure 3-1. Collapse and Stripout Limitations to Constant Bubble Diameter Compensation

### 3.1.2 Constant Diameter Considerations

This section which is a summary of the results obtained in Appendix B is important in understanding the material considerations necessary to effectively implement bias field compensation.

Bias field compensating techniques can only compensate for diameter fluctuations as a result of temperature variations. Eq 3.1 gives the condition for stable cylindrical bubble domains

$$\frac{\ell}{h} + \frac{H}{4\pi M} \left(\frac{d}{h}\right) - F\left(\frac{d}{h}\right) = 0 \quad (3.1)$$

where  $F(d/h)$  is the magnetostatic force function<sup>(3)</sup>,  $\ell$  is the characteristic length, and  $d$  is the domain diameter in a film of thickness  $h$  under a bias  $H$ . All the parameters in this equation except  $h$  are temperature dependent. After differentiating this equation with respect to temperature four different constraints can be imposed which lead to certain conditions that must be met to obtain a constant bubble diameter condition. These constraints are I constant bias, II constant characteristic length, III constant magnetization and IV no parameters held constant. The characteristic length is defined as

$$\ell = \frac{\sigma_w}{4\pi M^2} \quad (3.2)$$

where  $\sigma_w$  is the wall energy and  $4\pi M$  is the magnetization. Thus by matching the temperature variation of the wall energy and magnetization,  $\ell$  can be made constant with temperature. The magnetization in Case III above is only constant over a small temperature range depending on the value of the Neel temperature  $T_N$ .

Table 3-1 summarizes this analysis.

Table 3-1. Maintaining a Constant Bubble Diameter

Case	Constraint	Condition	Result
I	$H=\text{const}; H_T=0^*$	$M_T = \frac{\sigma_w}{MHd + 2\sigma_w} \sigma_w T$	$M_T$ must be negative
II	$\ell=\text{const}; \ell_T=0$ which implies $\sigma_{wt} = 2M_T$	$H_T = M_T$	$M_T$ must be negative
III	$4\pi M = \text{const}; M_T=0$	$H_T = -\frac{4\pi M}{Hd} \ell$	$H_T$ is too large to be met by permanent magnets alone
IV	none held const	$H_T = \left(1 + \frac{2\sigma_w}{MHd}\right) M_T - \left(\frac{\sigma_w}{MHd}\right) \sigma_w T$	$M_T$ must be negative

\*These variables are defined as  $G_T = \frac{1}{G} \frac{dG}{dT}$

<sup>3</sup> A. A. Thiele, "The Theory of Cylindrical Magnetic Domains," B.S.T.J. 48 3287 (1969).

For Case I no external bias compensation is required to maintain constant bubble diameter. Since the characteristic length is still quite temperature dependent for this case the bubble stability range will be temperature dependent. Thus the device temperature range will be limited by the collapse and stripout of the bubble which determine the bubble stability margins (refer to Figure 3-1).

In Case III where the magnetization is held constant the bias field is required to have a temperature coefficient on the order of  $+0.25$  to  $+0.55\%/^{\circ}\text{C}$ . Bias magnet materials presently available in general do not have temperature coefficients in this range and thus this case cannot be implemented. Another drawback is that the magnetization in most bubble materials cannot be made constant over any wide temperature range.

Case II is perhaps the most desirable from the standpoint of temperature compensation techniques and device operation. Since the characteristic length is constant the bubble stability range remains constant providing the widest temperature operating range with respect to the collapse and stripout limitations. Thus with temperature compensation the primary mechanisms for failure in this case will usually be a result of the mobility drop off at low temperatures and the wall energy drop off at high temperatures.

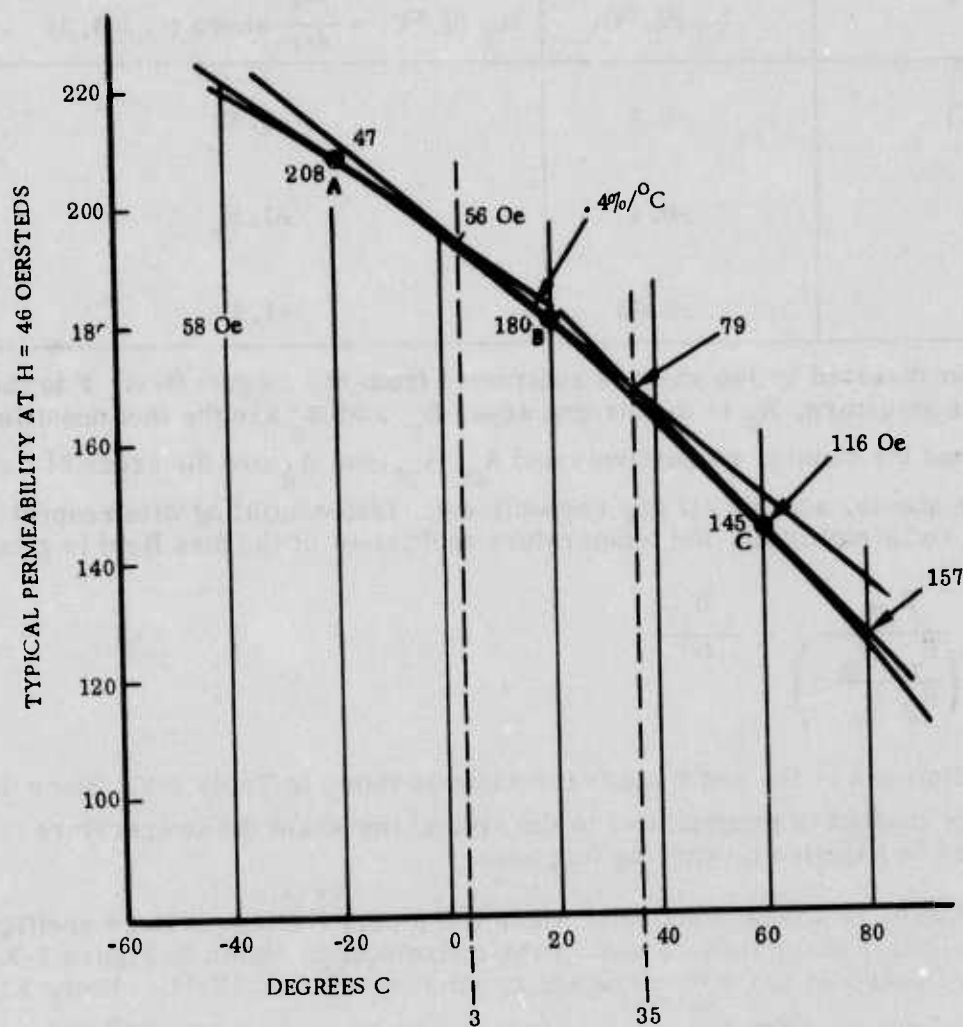
Case IV none of the parameters are held constant. Although this is typically the case for most materials it is desirable to approach Case II as closely as possible assuming that the mobility and wall energy do not become the limiting factors before collapse and stripout.

### 3.2 TEMPERATURE DEPENDENT SHUNT TECHNIQUE

This technique would principally be used to temperature compensate positive temperature coefficient bubble materials; although it could be also used with the temperature dependent magnet technique to provide additional means of bias field temperature coefficient tailoring. The technique is used in precision meter movements such as watt-hour meters and speedometers to provide thermal stability. The shunt materials are usually Ni-Fe alloys with nickel contents in the range of 29% to 33%. These alloy compositions have Curie temperatures in the range of  $150^{\circ}$  to  $200^{\circ}\text{C}$  which give them their good temperature dependent properties. Figure 3-2 shows the temperature dependence of the permeability for Carpenter "32" Type 1 material for an applied field of 46 Oe. The material for this applied field is essentially saturated. The temperature coefficient for the permeability at points A, B, and C of Figure 3-2 are given in Table 3-2.

As the temperature coefficients of these materials are negative, using them as shunts results in a positive temperature coefficient for the magnetic field (assuming the magnets are temperature independent). The shunt bypasses a certain amount of flux away from the field region. As the temperature increases the amount of flux shunted decreases thus increasing the strength of the magnetic field. Assuming the shunt is saturated the magnetic field in the air gap of the bias structure is given by (Eq C.6, Appendix C)

$$H_g = \frac{1}{FA_g} (B_m A_m - B_s A_s) \quad (3.3)$$



$$A: \frac{220 - 182}{(-40 - 20)208} = \frac{38}{(-60)208} = -.3\%/^{\circ}\text{C} (.83\%/^{\circ}\text{C})$$

$$B: \frac{210 - 152}{(-20 - 60)180} = \frac{58}{(-80)180} = .4\%/^{\circ}\text{C} (1.1\%/^{\circ}\text{C}) [.7 \text{ Oe}/^{\circ}\text{C}]$$

$$C: \frac{185 - 128}{(20 - 80)145} = \frac{57}{(-60)145} = .65\%/^{\circ}\text{C} (1.8\%/^{\circ}\text{C}) [2.1 \text{ Oe}/^{\circ}\text{C}]$$

MATCH AT RT

$$H_T = \frac{-B_T}{(\cdot)} = 0(\cdot) = \frac{+.4\%/^{\circ}\text{C}}{1.1\%/^{\circ}\text{C}} = .36$$

Figure 3-2. Permeability Temperature Dependence of Carpenter "32" Type 1 Material



Table 3-2. Temperature Properties of Carpenter "32"

	$\mu_T$ (%/°C)	$H_T$ (%/°C) = $\frac{-B_T}{(\cdot)}$ where $(\cdot) = 0.36$
A (-20°C)	-0.3	+0.83
B (20°C)	-0.4	+1.1
C (60°C)	-0.65	+1.8

where the flux diverted by the shunt is subtracted from the magnet flux.  $F$  is the form factor for the structure,  $A_g$  is the air gap area,  $B_m$  and  $B_s$  are the flux densities of the magnets and the shunts, respectively and  $A_m$ ,  $A_s$ , and  $A_g$  are the areas of the magnets, the shunts, and the air gap respectively. Differentiating with respect to temperature and simplifying, the temperature coefficient of the bias field is given by

$$H_T = - \frac{B_s T}{\left( \frac{B_m A_m}{B_s A_s} - 1 \right)} = \frac{-B_s T}{(\cdot)} \quad (3.4)$$

where the definitions of  $H_T$  and  $B_s T$  are the same as those in Table 3-2. Since the amount of flux shunted is proportional to the area of the shunt the temperature coefficient can be adjusted by varying this area.

TmGd:GaYIG is a bubble material which has a positive temperature coefficient. The bias required to maintain a constant bubble diameter is shown in Figure 3-3. It is essentially linear and has a temperature coefficient  $H_T^M \sim +1.1\%/^{\circ}\text{C}$ . Using Eq 3.4 where  $B_s T = \mu_T$  and equating  $H_T^M$  and  $H_T$  at point A of Figure 3.3 ( $T = 20^{\circ}\text{C}$ ) the quantity  $(\cdot) = 0.36$ .

The temperature coefficient of the bias field employing this shunt material is also shown in Table 3-2. The temperature variation of the bias field is plotted in Figure 3-3 (dashed curve) assuming the bias field is  $\sim 70$  Oe at room temperature. The expected operating temperature range for a bubble device using this material is estimated to be  $-5^{\circ}\text{C}$  to  $35^{\circ}\text{C}$ . These limits appear to be controlled solely by the bubble diameter since the mobility (Figure 3-4) at the low temperature limit seems adequate for a  $24\mu\text{m}$  period at 100 KHz and the wall energy is well above  $0.1$  ergs/cm<sup>2</sup> at the high end (Figure 3-5). The temperature dependence of the bubble diameter is shown in Figure 3-6. At the high temperature limit the bubble approaches collapse and at the low temperature limit the bubble diameter enlarges which could cause data errors due to bubble repulsion.

Although this temperature compensation technique appears to be viable the more temperature stable bubble materials have negative temperature coefficients thus this technique would probably not be used in a bubble memory unless additional shaping of the temperature compensation coefficient is required to attain the maximum operating temperature range.

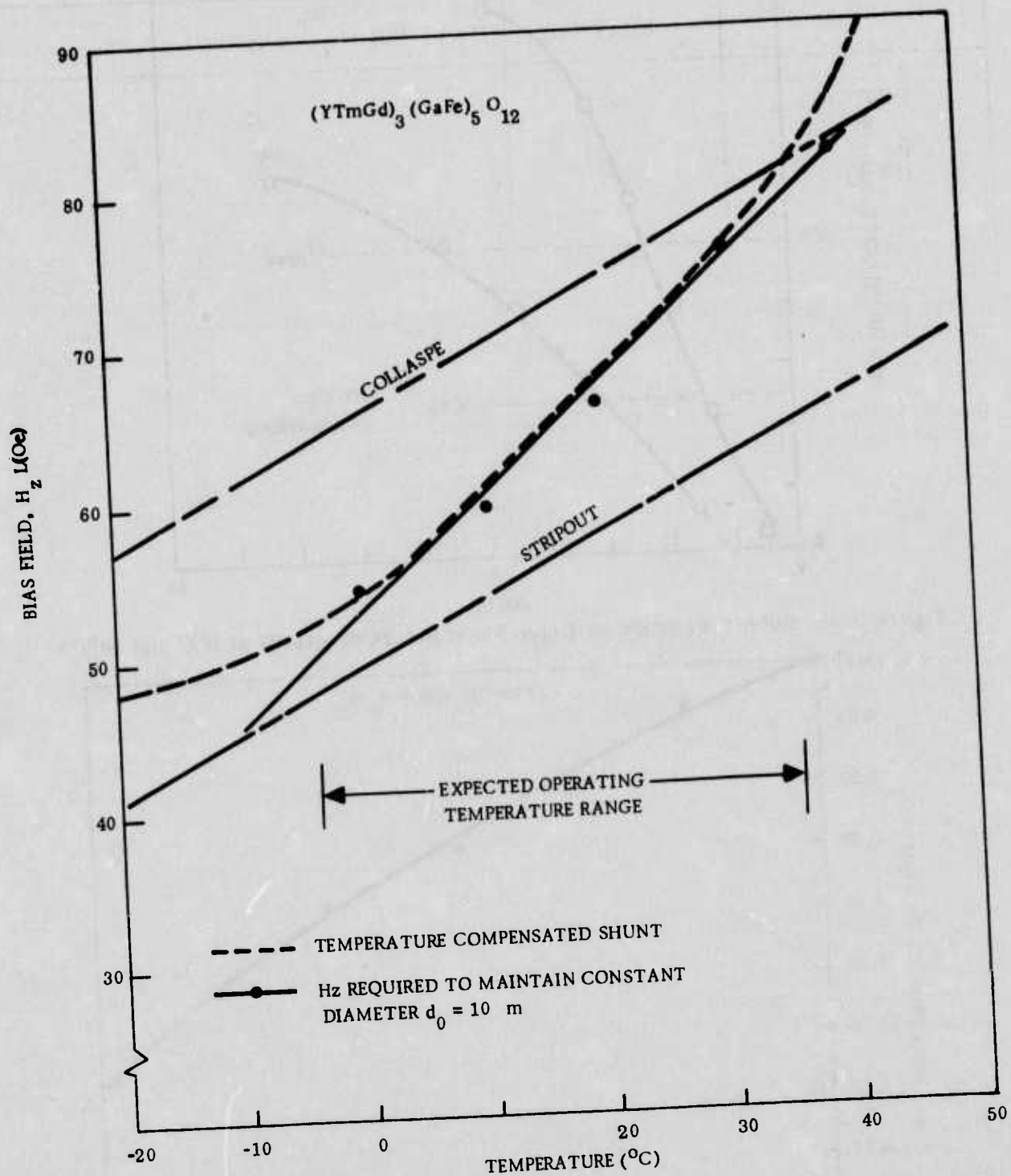


Figure 3-3. Stability Margin Temperature Dependence of YGdTmGaIG. Solid Line Indicates the Bias Field Necessary to Maintain a Constant Bubble Diameter. Dashed Curve Indicates the Estimated Temperature Variation of the Bias Field Using a Temperature Dependent Shunt.

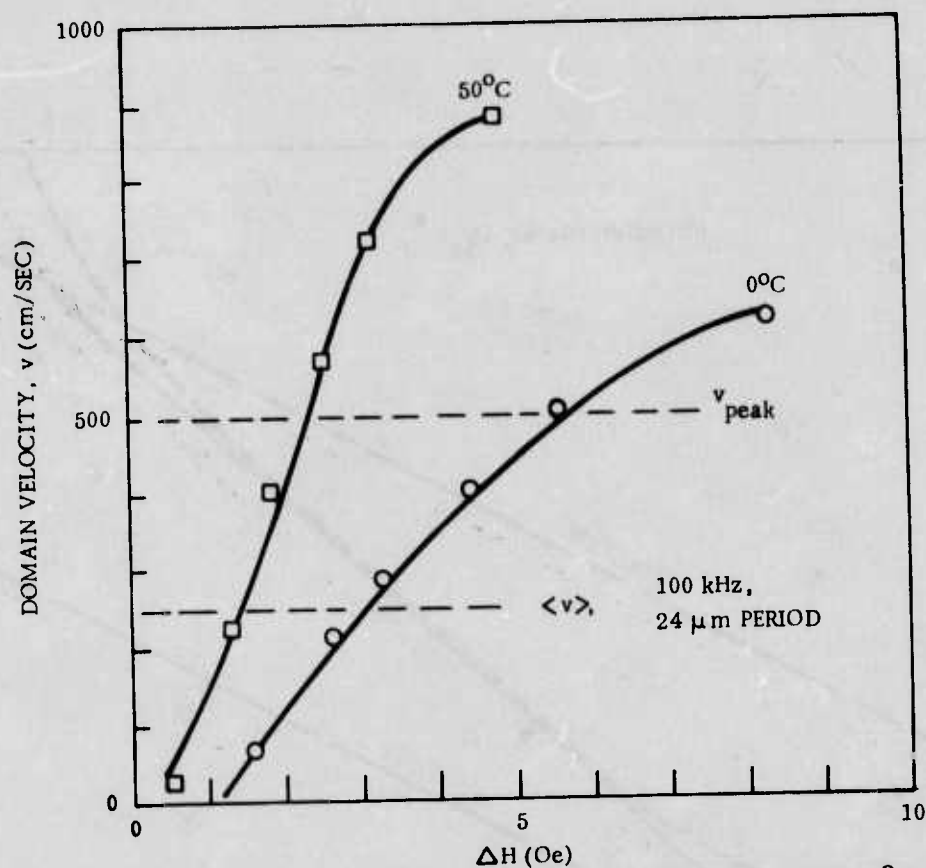


Figure 3-4. Bubble Velocity vs Drive Field for YGdT<sub>m</sub>GaIG at 0°C and 50°C

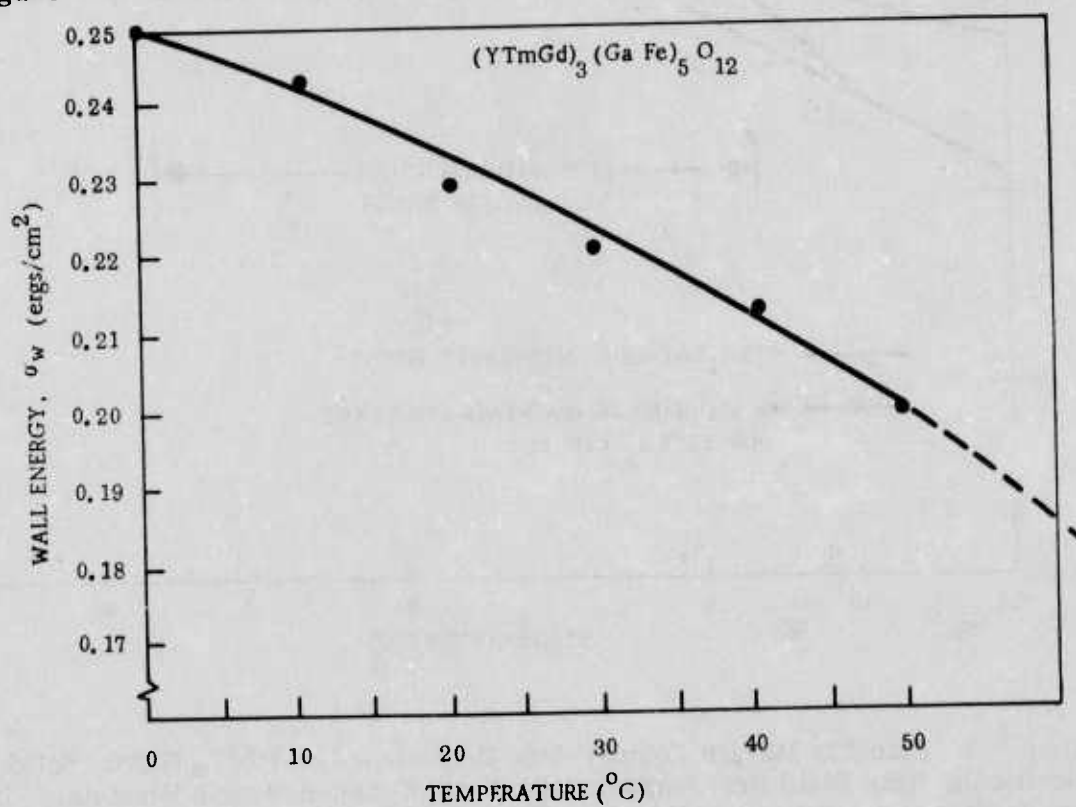


Figure 3-5. Wall Energy Temperature Dependence for YGdT<sub>m</sub>GaIG

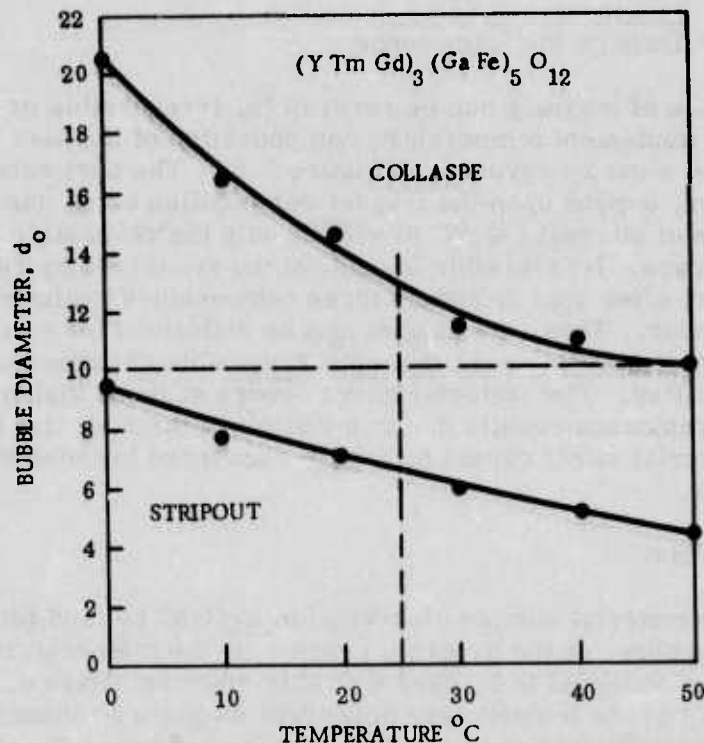


Figure 3-6. Bubble Diameter Temperature Dependence for YGdTmGaIG

### 3.3 TEMPERATURE DEPENDENT MAGNETS

In this approach temperature dependent magnets are used to temperature compensate the magnetic bias field for bubble materials having a negative temperature coefficient. Permanent magnets can be obtained in various compositions each of which have different temperature properties. This technique is simple to implement especially if a magnet composition can be found which closely matches the temperature coefficient of the bubble material over the desired operating range. If no standard composition can be found either a special composition has to be made with the proper temperature coefficient or two different magnets, one having a higher temperature coefficient and the other lower, with the amount of flux from each adjusted so that the resultant temperature coefficient is the one desired. The latter approach is by far the easiest of these two to implement. An alternative approach would be to use a temperature dependent shunt in conjunction with a temperature dependent magnet.

As magnets usually have a relatively high Curie temperatures the magnet temperature variation is fairly linear over the desired temperature range whereas that for the bubble material may not be. Additional shaping the bias field temperature variation may be required in order to match that of the material over a wide temperature range. This additional shaping will not be covered in this technical report.



### 3.3.1 Temperature Effects on the Remanence

Thermal variation of magnets can be reversible, irreversible or undergo a material effect<sup>4</sup>. To implement temperature compensation of the bias field the thermal variation of the magnet must be reversible (Figure 3-5). The particular thermal effects encountered, of course, depend upon the magnet composition being used. However, in the temperature range of interest ( $-25^{\circ}\text{C}$  to  $+75^{\circ}\text{C}$ ) only the reversible and irreversible effects need be of concern. Irreversible losses can be recovered by remagnetization (Figure 3-6), however, after approximately three temperature cycles no additional irreversible losses occur. Thus, the magnet can be stabilized for a certain temperature range by temperature cycling such that only reversible changes in the magnetization are encountered thereafter. The material effect occurs at much higher temperatures where a reduction in remanence results due to a change in the material itself (Figure 3-7). Losses due to the material effect cannot be totally recovered because the material is not the same as before.

### 3.3.2 Available Magnets

Since the bubble material composition  $\text{YEuTm}_{.65}\text{GaIG}$  is used for the deliverable bubble devices for this phase of the program (Para 6.1) the temperature compensated bias structure has been designed to be used with this material (Para 6.2). Thus the temperature coefficient of the temperature dependent magnets is chosen to match the (average) temperature coefficient of this bubble material which is  $T_c \approx -0.09$  percent/ $^{\circ}\text{C}$  (see Figure D-3, Appendix D).

Some easily attainable commercial magnets and their temperature coefficients are shown in Table 3-3. Represented are ferrous, ferrite, and rare earth permanent magnets. The ferrous magnets have relatively low temperature coefficients which can be either positive or negative. These magnets by themselves are not suitable for temperature compensation of the  $\text{EuTm}_{.65}$  material. The ferrite magnets on the other hand have temperature coefficients a little too large to be used with this composition. From the Table RARENET appears to be the closest match for this bubble material composition. The measured temperature variation of this magnet is shown in Figure 3-8 and was found to be very linear from  $-20^{\circ}\text{C}$  to  $100^{\circ}\text{C}$ . The other magnets tested (Figure 3-9) were barium ferrite compositions which were also very linear with temperature over this range.

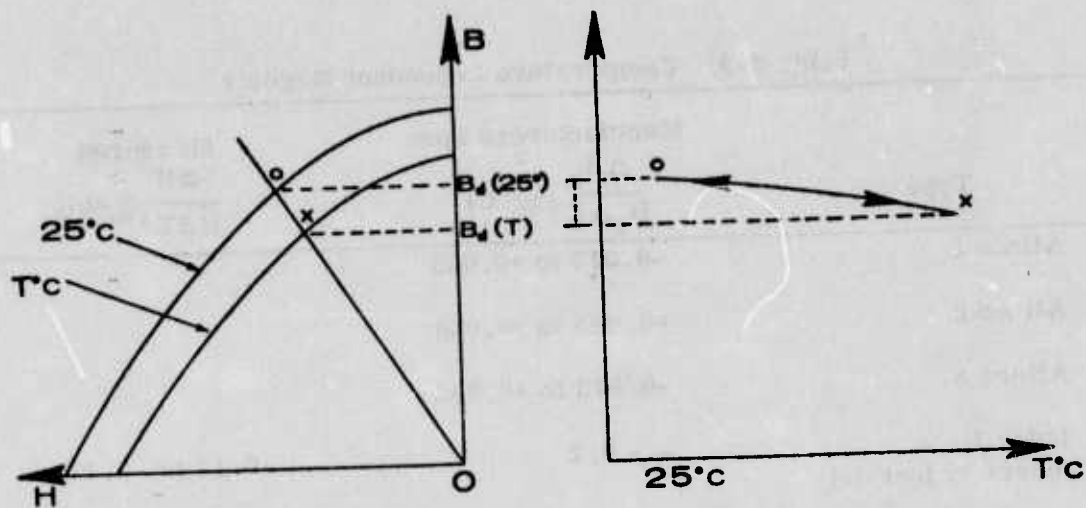
Although the measured RARENET magnet  $T_c$  (Figure 3-8) is approximately 20 percent higher than the average  $T_c$  of the bubble material listed in Table 3-3, Figure 3-10 shows that suitable temperature compensation should be obtained using this magnet. The bias field required to maintain a stable bubble diameter is not linear having a  $T_c$  at  $0^{\circ}\text{C}$  of  $-0.004$  percent/ $^{\circ}\text{C}$  and  $T_c$  at  $75^{\circ}\text{C}$  of  $-0.2$  percent/ $^{\circ}\text{C}$ . The value  $-0.09$  percent/ $^{\circ}\text{C}$  in Table 3-3 is only an average value over the range  $0^{\circ}\text{C}$  to  $75^{\circ}\text{C}$ . Over the range  $0^{\circ}$  to  $50^{\circ}\text{C}$  the bubble diameter variation is only about  $0.5 \mu\text{m}$ , a variation easily tolerated by bubble circuits. However, over the range  $-25^{\circ}\text{C}$  to  $+75^{\circ}\text{C}$ , the diameter varies approximately  $1.2 \mu\text{m}$ , being as much as  $1 \mu\text{m}$  smaller than the room temperature value. It is questionable that the device could operate reliably at the temperature extreme  $-25^{\circ}\text{C}$  even if no problems were encountered due to the lower

<sup>4</sup> R. K. Tenzer, "Temperature Effects on the Remanence of Permanent Magnets," ASD-TDR-63-500 Aeronautical System Division, Air Force Systems Command, Wright-Patterson Air Force Base, Ohio.

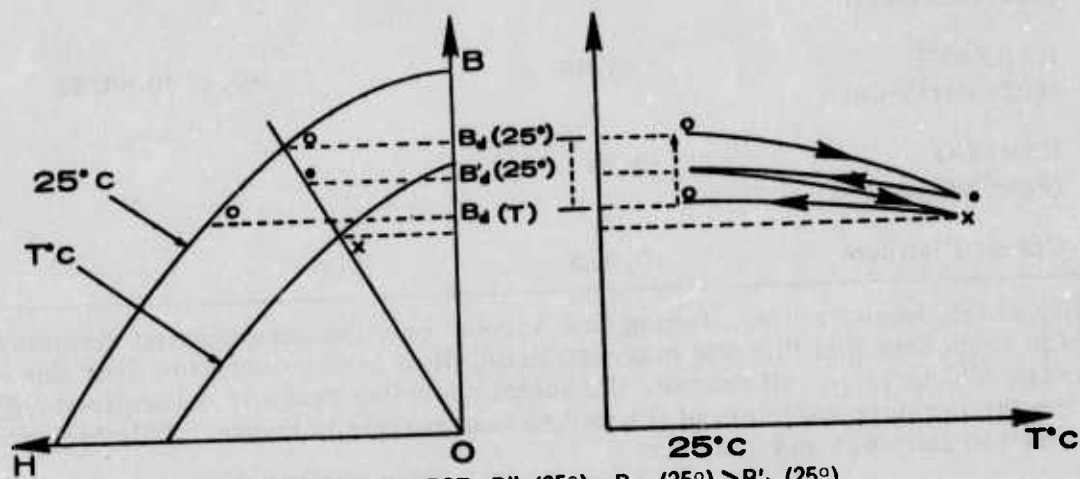
Table 3-3. Temperature Dependent Magnets

Type	Manufacturers Spec $\frac{\Delta B_r}{B_r \Delta T} (\%/^{\circ}\text{C})$	Measured $\frac{\Delta H}{H \Delta T} (\%/^{\circ}\text{C})$
Alinco 5	-0.013 to +0.033	
Alinco 6	-0.045 to +0.046	
Alinco 8	-0.013 to +0.033	
Index 1 (barrium ferrate)	~ - 0.2	-0.14 to -0.17
Plastiform (barrium ferrite)	-0.19	-0.18
RARENET (rare earth-Co)	-0.09	-0.11 to -0.12
RARECO (Sm-Co)	-0.04	
Cobalt Platinum	-0.015	

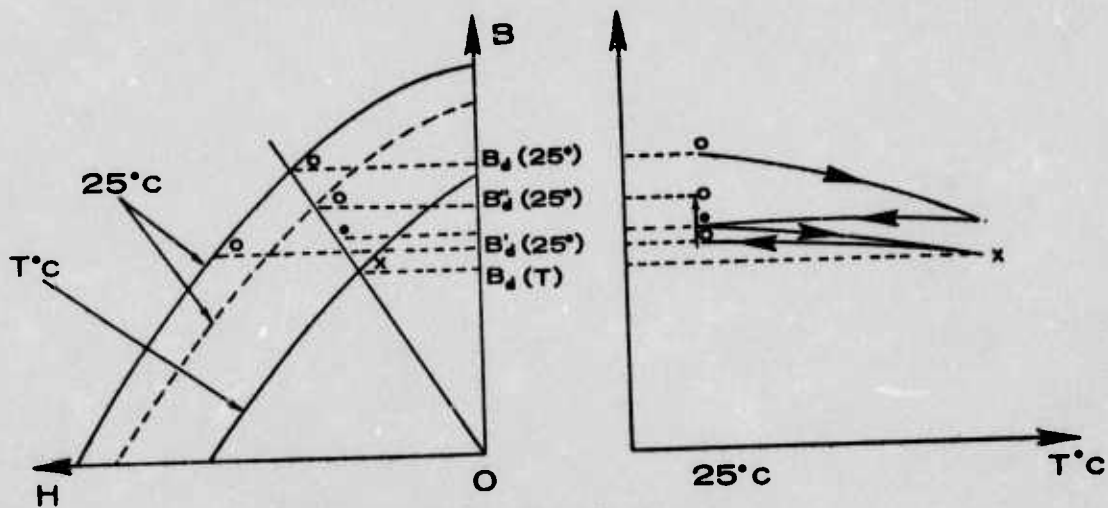
mobility at this temperature. Taking into account only the compensated diameter variation it appears that this PM magnet should allow device operation over the temperature range  $0^{\circ}\text{C}$  to  $75^{\circ}\text{C}$ . Of course, the actual operating range is determined only after the temperature variation of the device bias margin is known. This factor is considered in Para 6.1 and 6.2.



(a) REVERSIBLE EFFECT:  $B_H'(25^\circ) = B_H'(25^\circ) = B_A(25^\circ)$



(b) IRREVERSIBLE EFFECT:  $B_H'(25^\circ) = B_A(25^\circ) > B_H'(25^\circ)$



(c) MATERIAL EFFECT:  $B_H'(25^\circ) \neq B_A(25^\circ)$

Figure 3-7. Material Effects on Remnance<sup>(4)</sup>

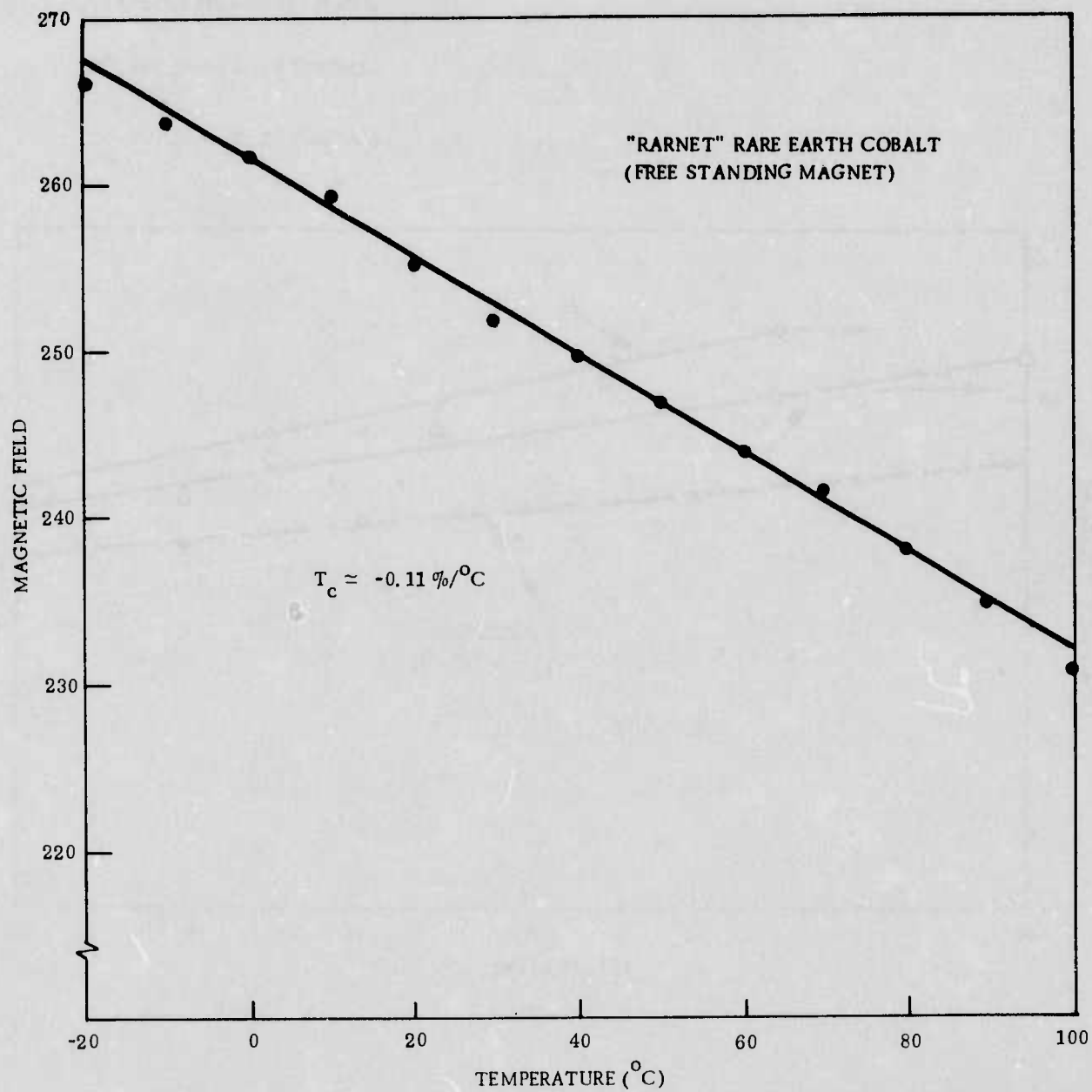


Figure 3-8. Temperature Dependence of RARNET



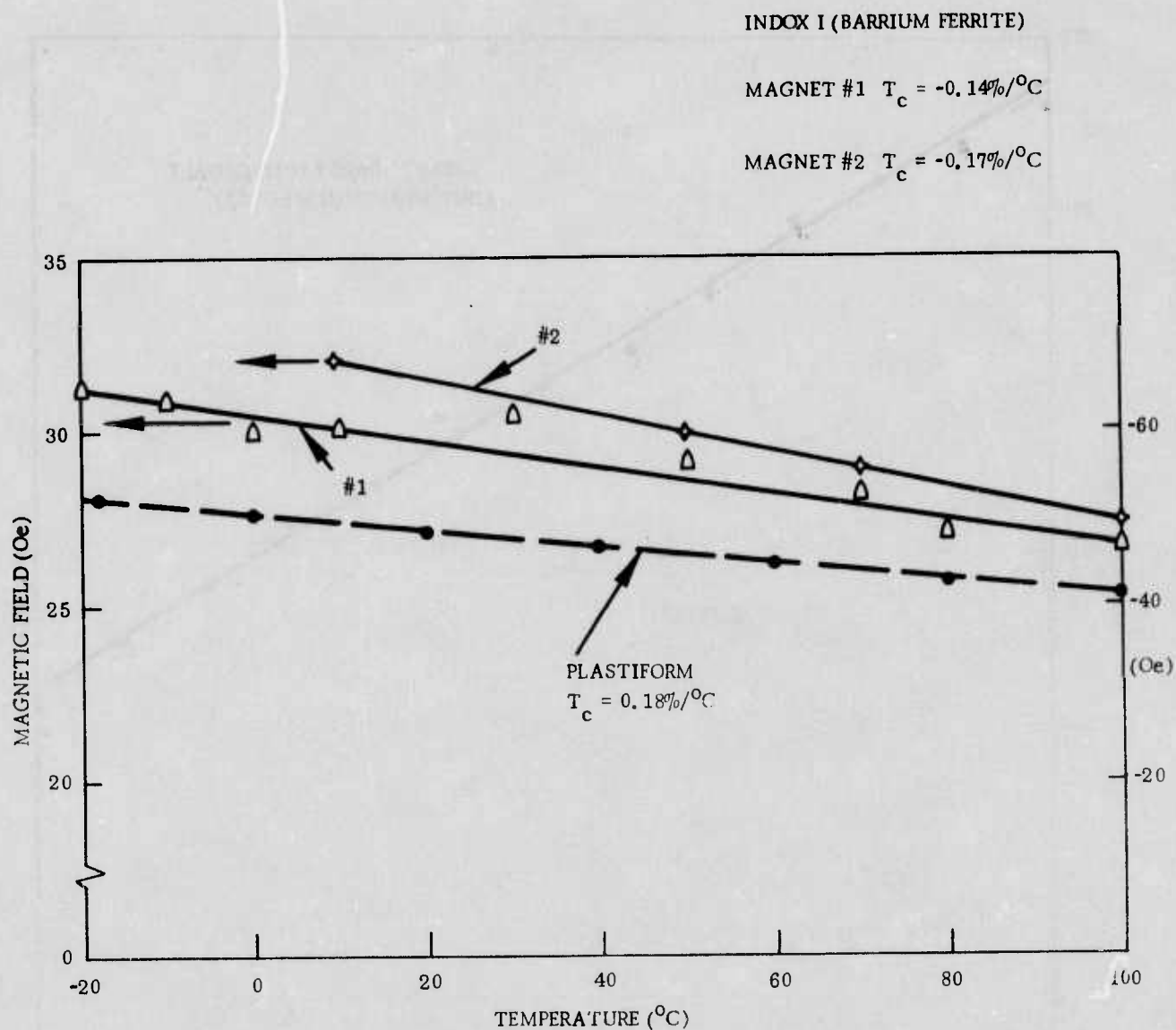


Figure 3-9. Temperature Dependence of Some Barium Ferrite Compositions

3-4-11 Y<sub>1.7</sub> Tm<sub>.65</sub> Eu<sub>.65</sub> Ga<sub>1.06</sub>  
 $\langle T_c \rangle \approx -0.09\%/^{\circ}\text{C}$  (0<sup>o</sup>C TO 50<sup>o</sup>C)

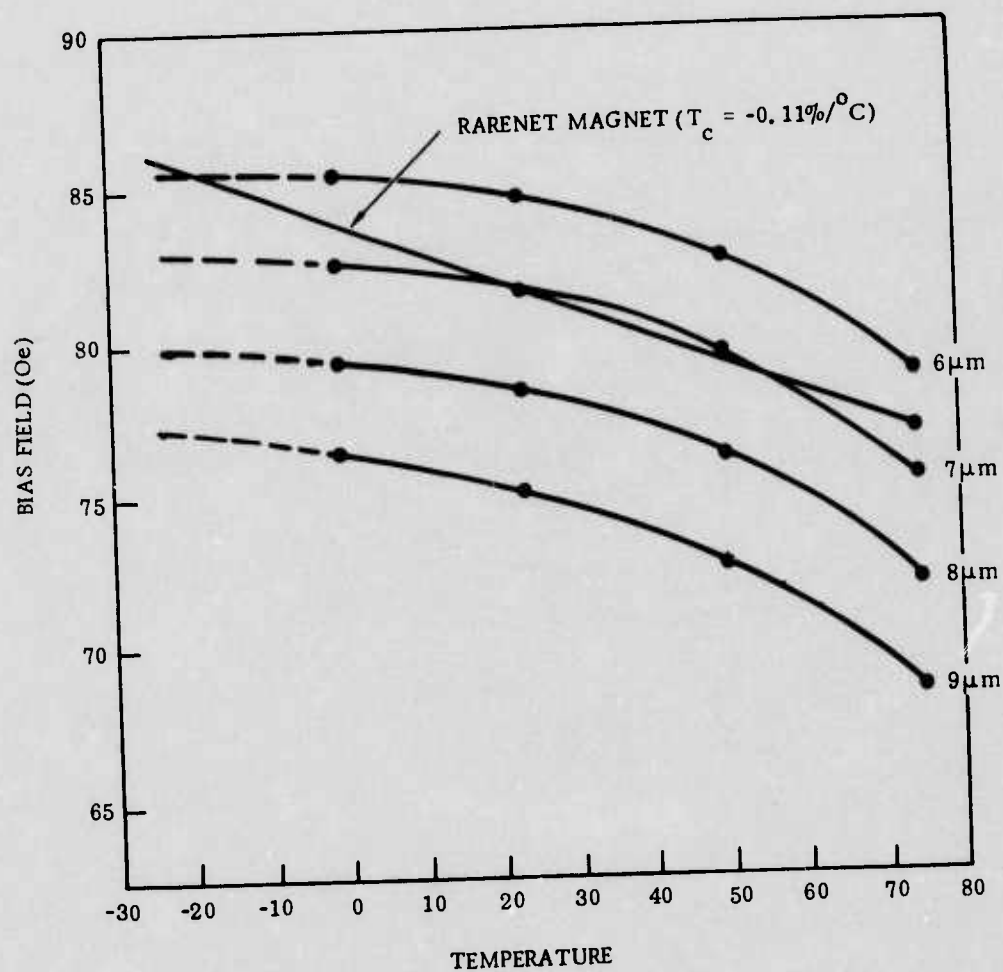


Figure 3-10. Comparison of the RARENET Magnet and EuTm<sub>.65</sub> Bubble Material Temperature Variation

## SECTION 4

### BUBBLE MEMORY PACKAGING TECHNIQUES

In preparation for bubble memory system hardware which is scheduled to be designed and constructed later on in this program, a review of bubble memory packaging techniques has been made. Packaging in regard to bubble devices will include the substrate which supports the device chips and any associated IC chips, the drive coils which provide the in-plane field, and the bias assembly which provides the perpendicular d-c magnetic bias field. In many instances the techniques used for semiconductor packaging are directly applicable to bubble domain memory packaging. However, bubble packages have certain other requirements (e.g., magnetic fields and their effects) for which packaging techniques must be developed.

The packaging techniques used for a particular bubble memory system will, in general, depend on the organization of the memory. Thus to arrive at a suitable package, the organization of memory must be known. In this case, since the particular need and the organization has not been established, no fixed set of ground rules will be assumed. However, this is in keeping with the package review format which will be followed here.

In general, the ground rules include weight, volume, and power restrictions (besides the organizational requirements) which are very important in determining the particular package configuration. Tradeoffs must be carried out to determine the bits/chip, chips/substrate, chips/coil, or coils/module. This involves weighing the power, weight, and volume vs reliability, ease of fabrication, maintainability, cost, and the chip organization.

Since Rockwell International has several aggressive packaging programs most of the material covered here is a direct result of these programs. Other overall packaging concepts have been reported by other investigators, however these will not be covered here in view of their specific coverage elsewhere.<sup>5, 6, 7</sup>

#### 4.1 CHIP SUBSTRATE

The primary requirements of a package to be used for bubble domain devices are: (1) magnetic fields - the package design, material content and assembly techniques must be such as to not distort the magnetic fields needed for proper device operation. All other requirements must be subordinate to this, (2) rigidity - this is necessary to maintain the critical magnetic field alignments and mechanical strength, (3) integrity - the chip circuits must be protected from harmful gas ambients, e.g., water vapor, ammonia, salt, and (4) thermal conductance - it is important that thermal gradients be minimized in the garnet chip area, as well as to maintain the package temperature within specified operating limits.

<sup>5</sup> A. A. Rifkin, "A Practical Approach to Packaging Magnetic Bubble Devices," IEEE Trans Magnetic MAG 9, 429 (1973).

<sup>6</sup> P. C. Michaelis and P. I. Bonyhard, "Magnetic Bubble Mass Memory - Module Design and Operation," IEEE Trans Magnetic MAG 9, 436 (1973).

<sup>7</sup> G. S. Almasi, W. G. Bouricilus, and W. C. Carter, "Reliability and Organization of a 10<sup>8</sup>-Bit Bubble Domain Memory," AIP Conf Proc., Magnetism and Magnetic Materials - 1971, p 225, Amer. Inst. of Physics, New York, 1972.

One substrate material which can be used for magnetic bubble chips is electronic grade ceramic (alumina or beryllia). Another substrate material is polyimide film with a stiffener which will be discussed later. Ceramic satisfies the requirements on distortion of the magnetic fields, rigidity, and adequate thermal conductance and thermal uniformity. The choice between beryllia and alumina depends upon several other factors. Alumina, though not as good a thermal conductor as beryllia, has the distinct advantage that buried metallization layers can be obtained. This would be important where a large number of bubble chips are to be contained in a single package. Beryllia, though it possesses the advantage of being a superior thermal conductor, cannot at present contain buried layer metallization since the cofiring temperature is too high. The ceramic package industry has been addressing this problem and when multi-layer beryllia packages are available, complex magnetic bubble arrays may possibly use beryllia. However, for present technology, alumina packages with buried metallization are being used for bubble device packaging.

A package design utilizing a conductor bearing polyimide film has been proposed recently on another Rockwell bubble program (Figure 4-1). The conductor can be etched into configurations suitable for use as device conductor lines, bonding pads, and possibly even flat field coils. A polyimide stripline package has been fabricated with the terminal conductor extending over an opening in the film in which the die is to be placed. The extended conductors make contact with the bond pads of the die and require only one bonding connection. This is called a beam frame method and is very similar to a beam lead technique, however the beams are in the package instead of the die. Beam lead die could also be used with the polyimide approach. The package in the region of the die can be stiffened by an inexpensive alumina plate which would also provide heatsinking. The polyimide package can also be its own flexible cable being folded around the external coil structure in order to make connection to external electronics.

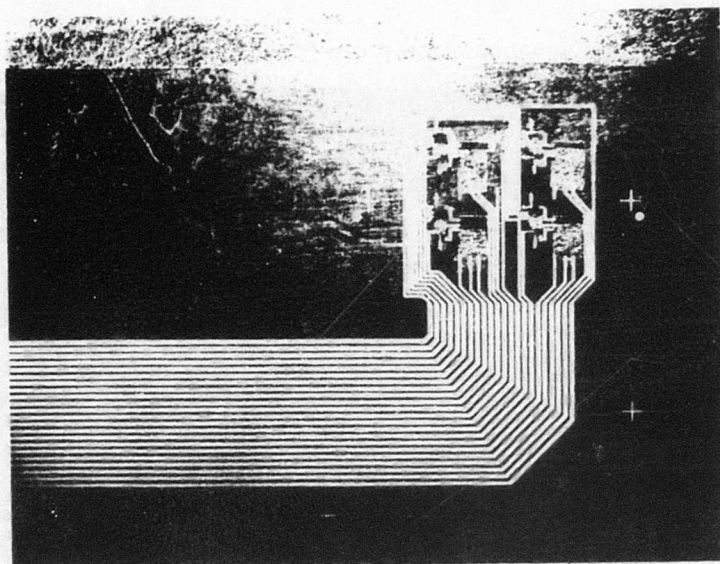
Also being investigated at Rockwell is a multilayer polyimide package (Figure 4-2) which could be used instead of multilayer alumina boards. Substrate costs could be reduced by as much as a factor of 20 using the multilayer polyimide package approach; however, the advantage of thermal conductivity must be sacrificed. Presently a 60 mil thick 3 layer polyimide test board has been fabricated as a package feasibility vehicle.

The metallization scheme used for the chip package conducting paths and chip mounting pads must be nonferromagnetic and sufficiently thin that the rotating magnetic field power loss due to eddy currents is negligible. For a 10  $\mu\text{m}$  gold film, the eddy current loss at 150 kHz for a 30 Oe rotating field is estimated to be about 10  $\mu\text{W}/\text{cm}^2$ . The common metallization schemes used for ceramic packages are tungsten/gold or molybdenum/gold which both meet the requirements of being nonferromagnetic conductors.

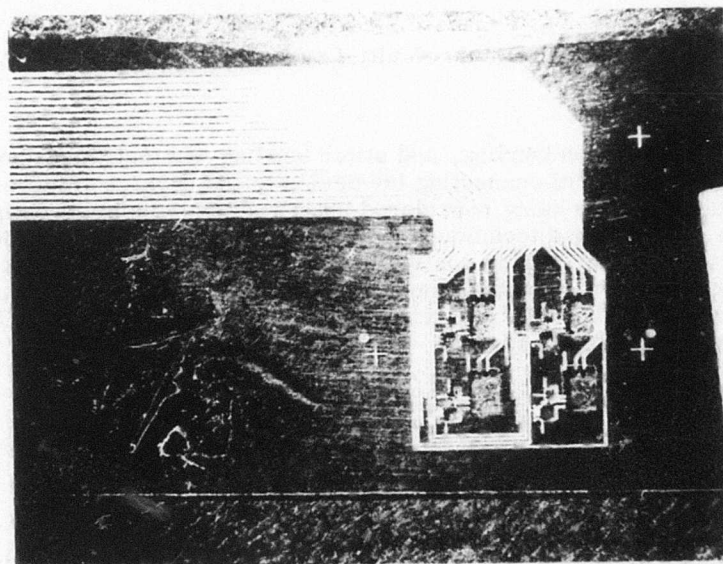
## 4.2 CHIP BONDING

Chip bonding to the package can be done using several techniques presently used extensively for semiconductors. The easiest method is to use an epoxy adhesive. At the present time this technique seems to be sufficient. Eutectic bonding can also be used, however it is more difficult and requires the application of heat which could adversely affect the devices in certain cases (Para 2.1). Solder flow techniques also fall into this category.





(a) Bottom View



(b) Top View

Figure 4-1. Polyimide Beam Frame Package.  
Square Openings are for Four Chips. Leads Extend over Edges for Connections.

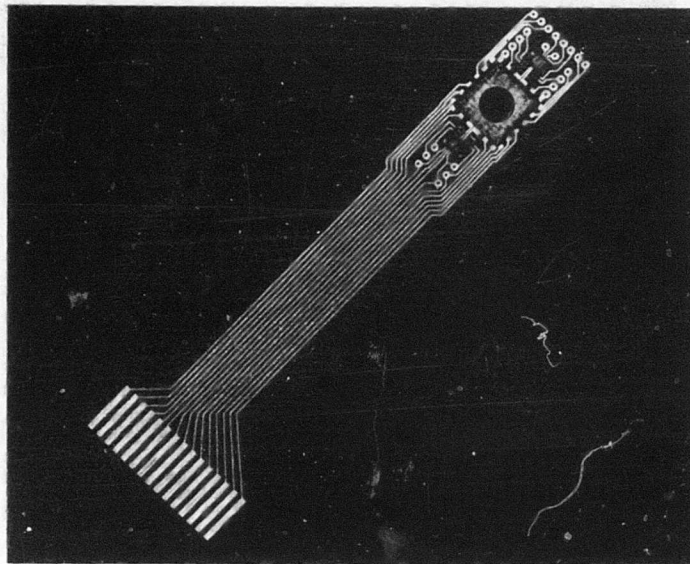


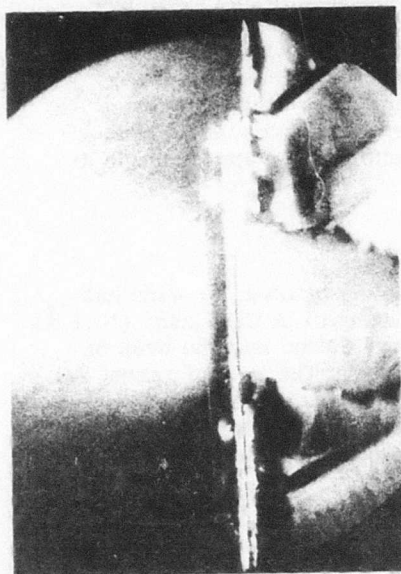
Figure 4-2. Multi-Layer Polyimide Board

#### 4.3 LEAD BONDING

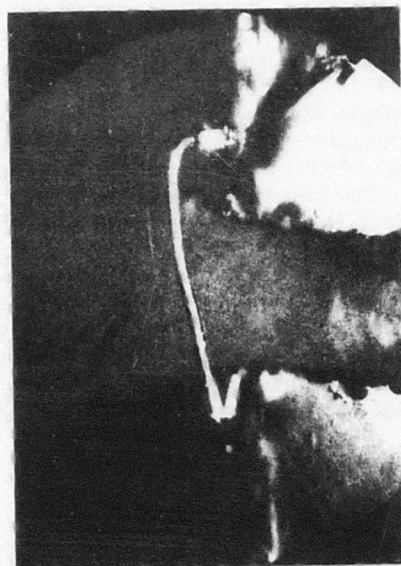
Flying lead, ribbon bonding, and stitch bonding are techniques now being investigated for electrical connecting the device to the package (Figure 4-3). Beam lead techniques are also being considered but not actively being investigated at the present time. Flying lead techniques using small (0.001-0.002 in.) round wire should be avoided. The looping configuration of the lead works against the need for planar attachment due to  $d\phi/dt$  pickup from the rotating magnetic field. Measured results for  $d\phi/dt$  for these three bond configurations as a result of the bonding method were as follows at 150 kHz.

1. Ball wedge bond = 208  $\mu V$
2. Wedge-wedge wire = 66  $\mu V$
3. Wedge-wedge ribbon = 13.2  $\mu V$

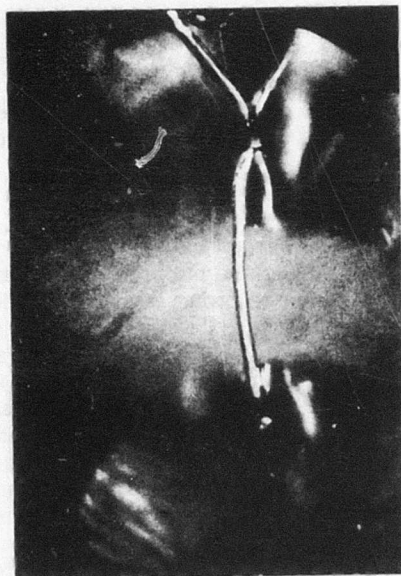
The three configurations included (1) ball bond-wedge bond of a 1 mil diameter Au wire, (2) wedge-wedge bond of a 1 mil diameter Au wire, and (3) wedge-wedge bond of a 1x5 mil Au ribbon. At the present time wedge-wedge ribbon bonding is the best technique available. However, beam lead techniques would be the most desirable from the standpoint of eliminating  $d\phi/dt$  pickup and withstanding shock and vibration. This technique will require a considerable amount of effort to develop it for use with bubble devices.



STRAP BOND  
(WEDGE-WEDGE RIBBON)  
AREA = 6.6  $\square$  MIL  
 $\frac{d\phi}{dt}$  PICKUP = 13.24  $\mu$ V



BALL-WEDGE  
BOND  
AREA = 104.4  $\square$  MIL  
 $\frac{d\phi}{dt}$  PICKUP = 208.84  $\mu$ V



LAP-LAP WIRE  
BOND (STITCH)  
AREA = 33  $\square$  MIL  
 $\frac{d\phi}{dt}$  PICKUP = 66  $\mu$ V

Figure 4-3. Flying Wedge (Ball-Wedge), Ribbon (Strap-Bond), and Stitch Bonding (Lap-Lap) Bonding Techniques



The polyimide package approach allows a pseudo-beam lead bonding technique to be used. The connecting pads and other electrical connections can be etched in the polyimide film. The sample can then be overlayed on the pseudo-beam leads and bonded using standard thermo-compression techniques.

#### 4.4 HERMITICITY

In some cases a sealed ceramic system will be required to maintain a stable noncorrosive ambient for the bubble circuit film elements. As stated in Para 2.5 passivation techniques are being investigated to protect bubble circuits as an alternative to hermetic sealing. The use of either alumina or beryllia for the package material offers the choice of a hermetic, glass frit, or epoxy cement seal. The hermetic seal (metal-to-metal) system for sealing cannot be employed because the temperature required to form the seal is damaging to the permalloy circuit. Low temperature solder seals needlessly complicate the package fabrication costs and process. The low temperature glass frits currently available in the industry could bring the processing temperature down to acceptable levels. In particular, the use of a perimeter sealer employing a "back contact heat sink" would maintain the temperature of the garnet dice themselves at a lower temperature than the seal ring area. Another possible sealing process for the glass seal is the belt furnace. Here, the sealing fixture is preferentially designed to perform the same function as the back contact heat sink of the perimeter sealer.

#### 4.5 LASER DICING

Laser dicing as opposed to mechanical dicing or sawing by blade or wire has been found to be the best technique for dicing fabricated wafers. A CO<sub>2</sub> laser (10.6 Å) has been successfully used to dice garnets. The beam penetration into the back of the wafer was about 40 percent of the 30 mil wafer thickness. The loss of garnet due to mechanical and thermal damage is only about 2 mils. Thus, device arrays can be packed very tightly on the wafer to utilize the maximum area. This method will be the best candidate for large volume bubble device production.

#### 4.6 ROTATING FIELD NETWORK

The in-plane rotating magnetic field network provides the drive for the permalloy propagation structures. The rotating fields can be generated by flat air core coils, flat ferrite coils (in pairs) (Figure 4-4), and ferrite pole structures (Figure 4-5). The last two techniques provide open structures however the last technique suffers from a very poor volume efficiency because of the very small region of field uniformity. The ferrite pole approach also does not provide any significant decrease in the power dissipation as might first be assumed (using high  $\mu$  material) because of the relatively high demagnetizing effects of the thin ferrite slabs. The ferrite in the second approach is used to decouple the windings on either side of the ferrite from each other, thus improving the field sensitivity and uniformity, and also volume efficiency. The flat air core and flat ferrite coils are at present the best approaches for generating the in-plane fields.



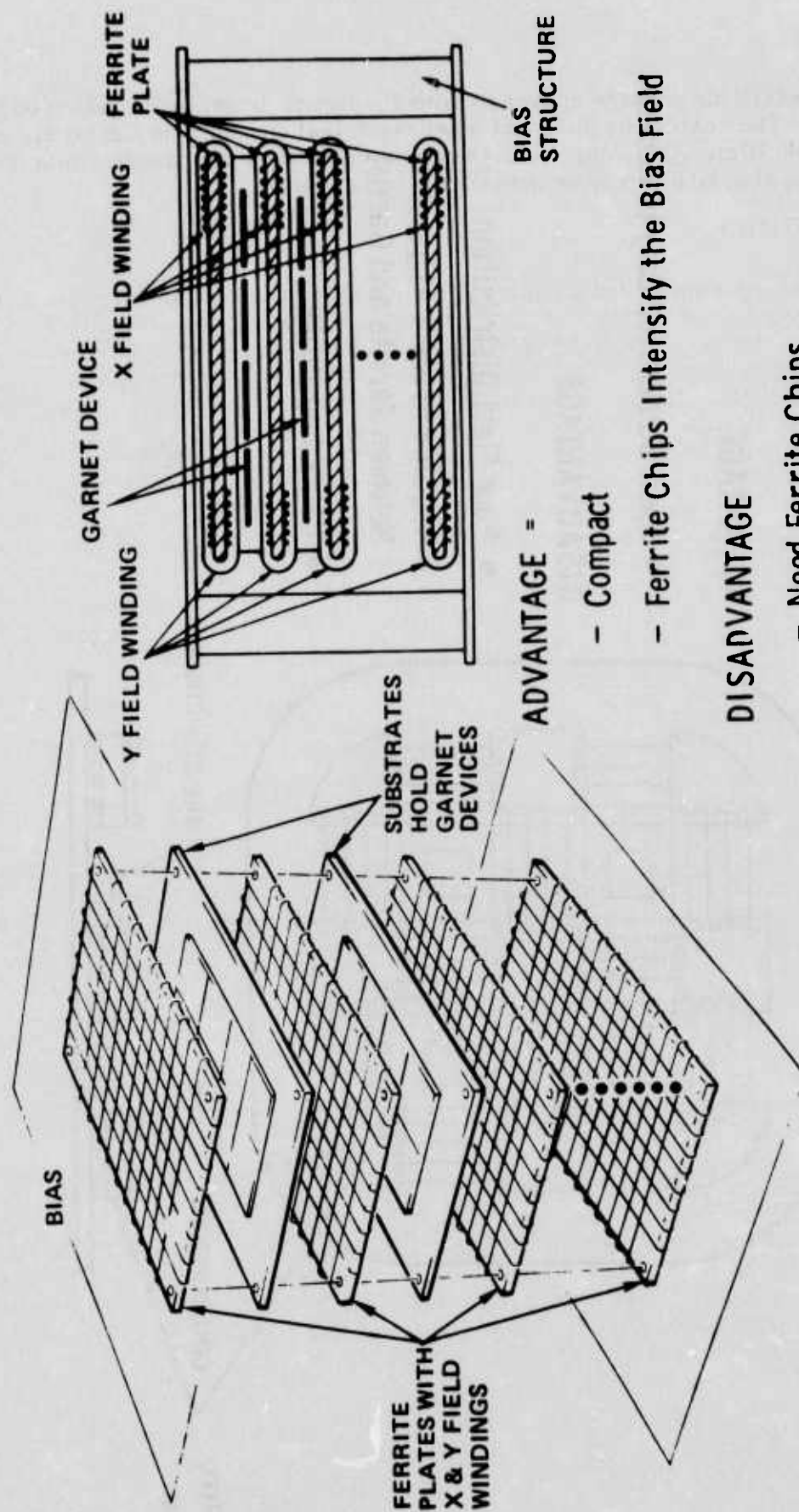
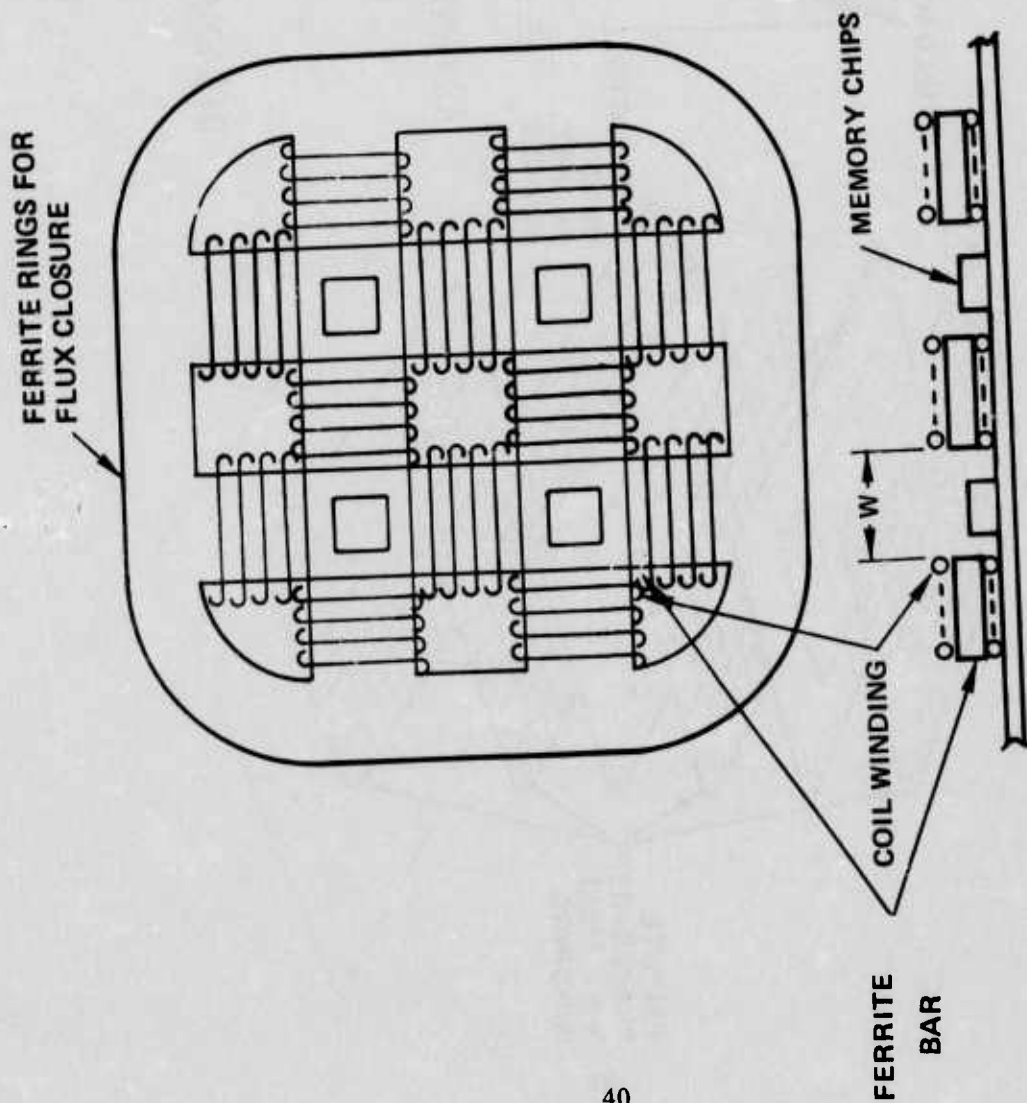


Figure 4-4. Flat Ferrite Coils



#### ADVANTAGE:

- Open Structure, Easy to Access

#### DISADVANTAGE

- Poor Field Distribution
- Require Precise Alignment Between Ferrite and Garnet
- Heavy and Bulky

Figure 4-5. Ferrite Pole Structure

The important factors that must be considered in designing the rotating field network are power dissipation (or resonance resistance), inductance, field uniformity, and the method of construction. The power dissipation and thus the resonance resistance and the inductance depend on the number of turns and the volume of the coil structure. Thus the power and inductance can be minimized by reducing the number of turns and the volume of the coil while meeting the field magnitude and volume requirements of the intended package. The resonant resistance also depends on the interwire coupling effect which occurs at high frequencies ( $>300$  kHz). This effect can be minimized by using the minimum number of turns and using only a single layer. Litz wire which is a braided wire gives the coil a better Q than solid wire does because of a decreased effects of eddy current losses at high frequencies. If a wire wound coil is used, the final selection on the wire size is determined primarily by the driver design.

Since the in-plane field coils are mounted in the bias structure, additional loss will also be induced by the coupling between X, Y coils and bias plates. The resonance resistance measurement indicates that when the mu metal plates are placed directly on top of the in-plane coil, the coil loss increased by more than 100 percent at 150 kHz (300 percent at 1 MHz). This loss can be reduced by increasing the spacing between the coil and the bias plate; however, this is not practical when the package size is limited. A better way for decoupling is by inserting a thin ferrite plate between the coil structure and the bias plates. Initial measurements indicate that using a 0.05 in. thick ferrite antenna strip as a spacer, the increase in coil loss at 150 kHz can be reduced to less than 20 percent. Under this arrangement, the flux leakage outside the coil is also reduced, thus minimizing the coupling between neighboring coil assemblies. Placing magnetic material outside the coil also increases the coil inductance and the inside flux density, but in both cases, these increases are small being less than 10 percent. Thin conductor foil can also be used as shielding material. It is more flexible and much cheaper than ferrite plates, however, measurements using a 0.001 in. copper foil indicate that the shielding effect is not effective below 1 MHz. Also, the eddy current loss is too high compared with the coil loss. This arrangement decreases the coil inductance and field sensitivity at high frequency.

The inductance of the X and Y coils is important from the standpoint of instantaneous turn-on and shut-off of the rotating field at the high frequencies. Since the coils are normally operated in resonance the turn-on of the rotating field can be accomplished by voltage precharging the resonant capacitor or current precharging the coil. In order to minimize the voltage required to perform these precharge conditions at high frequencies the coil inductance must be kept minimum ( $V_{pc} = \omega_0 L_c I_c$ ).

For a flat coil where the thickness of the coil is much less than the length or width the region of uniform field is in general, one thickness dimension from the sides and end of the coil and one wire layer thickness from the top and bottom of the coil. The uniformity of the in-plane field is not critical ( $\sim 10$  percent) since the drive field must only be greater than some minimum value to provide reliable propagation. The orthogonality of the X and Y fields need only be such that the major/minor axes of the resulting elliptical field be within  $\sim 10$  percent. Also the largest discrepancy in phase angle between the rotating field within the device region can be as much as 10 to 15 deg without significantly degrading device operation. The most important field variation is that of the z-component of the in-plane field. If this varies more than  $\pm 0.5$  percent of the in-plane magnitude it could cause a severe reduction in the bias margin.

Coils can also be constructed by using strip lines rather than wires, (Figure 4-6). One approach, using a copper coated polyimide film (1 oz copper on 1 mil polyimide insulation films) is presently being investigated in this lab. It is equivalent to a coil winding with a small number of turns per layer but many numbers of layers. It was hoped that with this arrangement, the current redistribution effect due to the flux linkage would be less than that of the conventional wire winding thus minimizing the high frequency loss. Preliminary measurement on a 20 layer (2 turn coil) shows that  $R_{res}$  increases about three times in going from 100 kHz to 1 MHz. This is better than the wire wound coil. In order to increase the field sensitivity and field uniformity, more turns and less spacing between turns are required. This has been accomplished by etching parallel conductors (0.80 in. wide, .20 in. separation) on a polyimide stripe film. A continuous coil is achieved by wrapping the strip around the coil form and interconnecting the conductors by the solder reflow technique. This approach can greatly simplify the coil winding if acceptable performance can be achieved. The main problem at present is how to fabricate thicker but still flexible copper strips required to reduce the coil loss.

#### 4.7 BIAS FIELD STRUCTURE

In order to minimize power and to obtain nonvolatility the bias field is provided by a permanent magnet structure. Since the bias field must be uniform over a relatively large area, depending on the number of bits-per-structure, the field is shaped by parallel high permeability plates acting as large pole pieces. For maximum volume efficiency the magnets are placed between the plates (Figure 4-7). This approach has relatively high leakage flux which for some circumstances may be undesirable when magnetic contamination of nearby equipment must be avoided. Leakage fields from the bias structure can be minimized by the closed structure shown in Figure 4-8 which reduces the leakage flux by 42 dB right next to the outside surface (1 Oe for nominal bias fields inside).

The bias fields are very uniform inside the parallel plate PM structure one plate separation distance away from the edge and one magnetic diameter (or width) away from the inside face of the magnetic. Table 4-1 gives the nominal field uniformities within these limits.

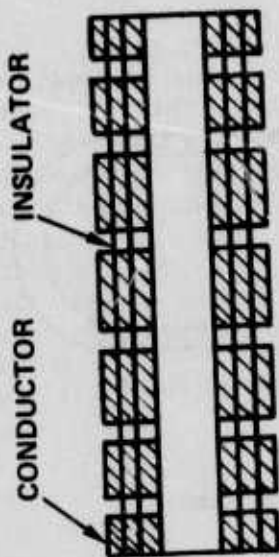
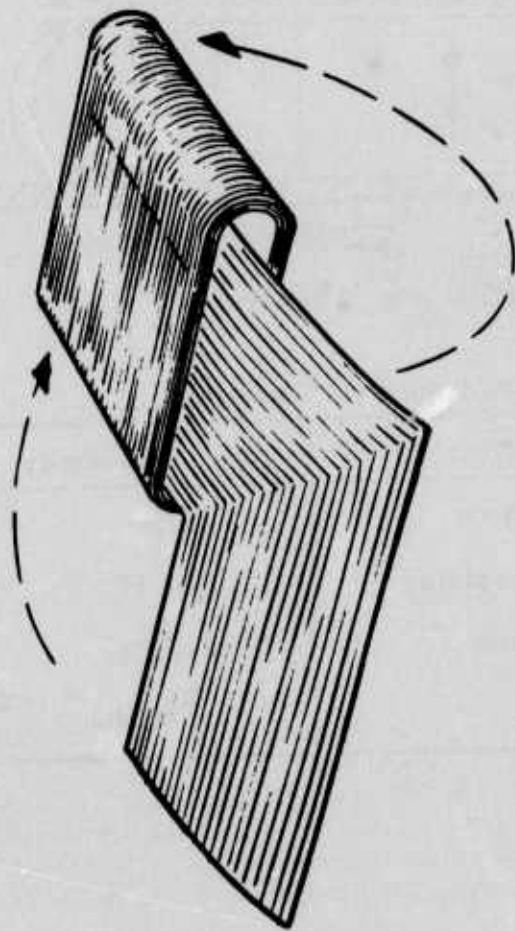
Bias field tuning can be provided by variable or fixed shunts. Fixed shunts used for coarse tuning can be designed for 3-10 Oe/shunt and fine tuning using screws can be designed a fraction of an oersted per turn. Standard magnetic circuit calculation techniques can be used to design the structure (Para 6.2 and Appendix C).

Temperature compensation can be provided by using temperature dependent shunts (Para 3.2) or temperature dependent magnets (Para 3.3).

#### 4.8 PACKAGE CONCEPTS

Figure 4-9 shows an exploded view of one bubble memory package currently under development at Rockwell International. It consists of two chip multilayer alumina substrates separated by a spacer ring and support pedestals which allow up to nine die packages to be mounted on each of the boards. Connections to the chips from the chip substrate metallizations can be made either by pulse or ultra-sonic wire or strap bonding methods. Alternative flip-chip bonding techniques are currently





#### ADVANTAGES:

Simple – Easy to Wind

Less High Frequency Loss

Better Field Uniformity by Using Non-Uniform Conductor Strip

#### DISADVANTAGE

Less Conductor-to-Insulator Ratio

Figure 4-6. Strip Line Coils

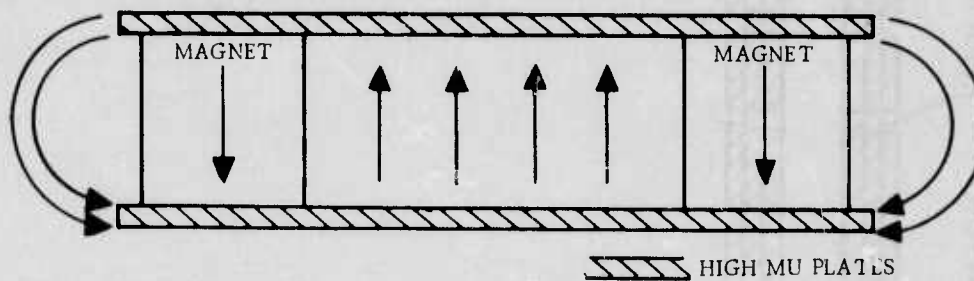


Figure 4-7. PM Parallel Plate Bias Structure

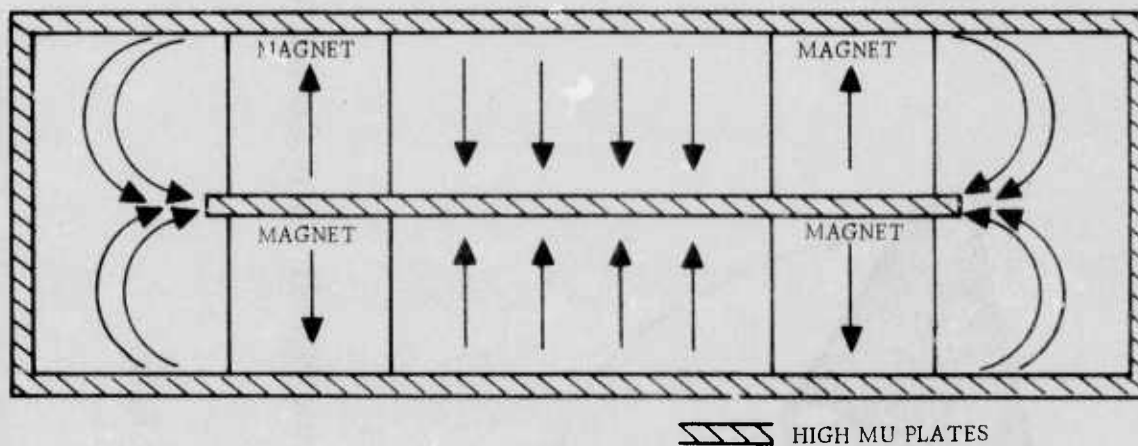
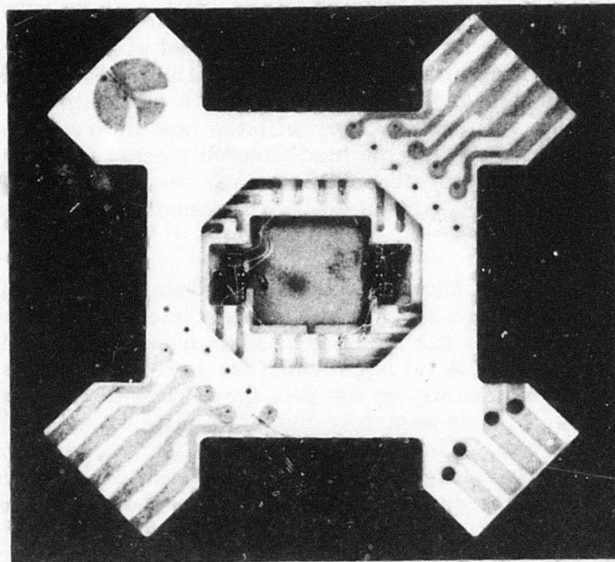


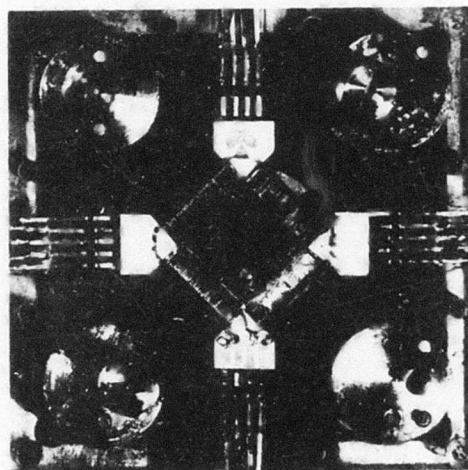
Figure 4-8. Closed PM Bias Structure

Table 4-1. PM Bias Structure Field Uniformity

Field Component	Direction	Uniformity
$H_z$	Center Plane	$< \pm 1\%$
$H_z$	Normal to plates	$< \pm 0.2\%$
$H_{in-plane}$	Center plane	$< \pm 0.5\%$
		$\langle H_{in-plane} \rangle = 0$



(a)



(b)

Figure 4-9. Package Concept - 1

being studied. Interconnection from the chip substrates to the outside world is accomplished through a flexible tape cable which is folded around the coil windings to the external PC board. The coil structure is compatible with both the chip substrates and a permanent magnet bias assembly as shown in the figure. The package is assembled by sliding one coil over another with the tape interconnect in-between and then sliding the whole module into the bias assembly package. This package provides a uniform field region large enough for many chips including associated electronics and also provides easy access to the chip substrates for repair or replacement.

Figure 4-10 shows what is known as butterfly package which is currently being used in connection with experimental work at Rockwell International's Electronics Research Division. The package has a buried conductor scheme fabricated by an in-house alumina tape process. A lid is provided for hermetic sealing. The X and Y drive field coils are wound directly on the package. The die placement area for the present package design is approximately 200 x 200 mils which could be enlarged slightly to accommodate a chip up to 250 mils square. The package also has area enough to support any associated electronics. Two of these packages may also be placed back-to-back winding the drive coil around both of them and doubling the package capacity. The only difficulty that might be encountered in this case is making the interconnection from the module to a breadboard. The package is completed by placing it in a permanent magnet bias structure. One or several packages may be used in a single structure.



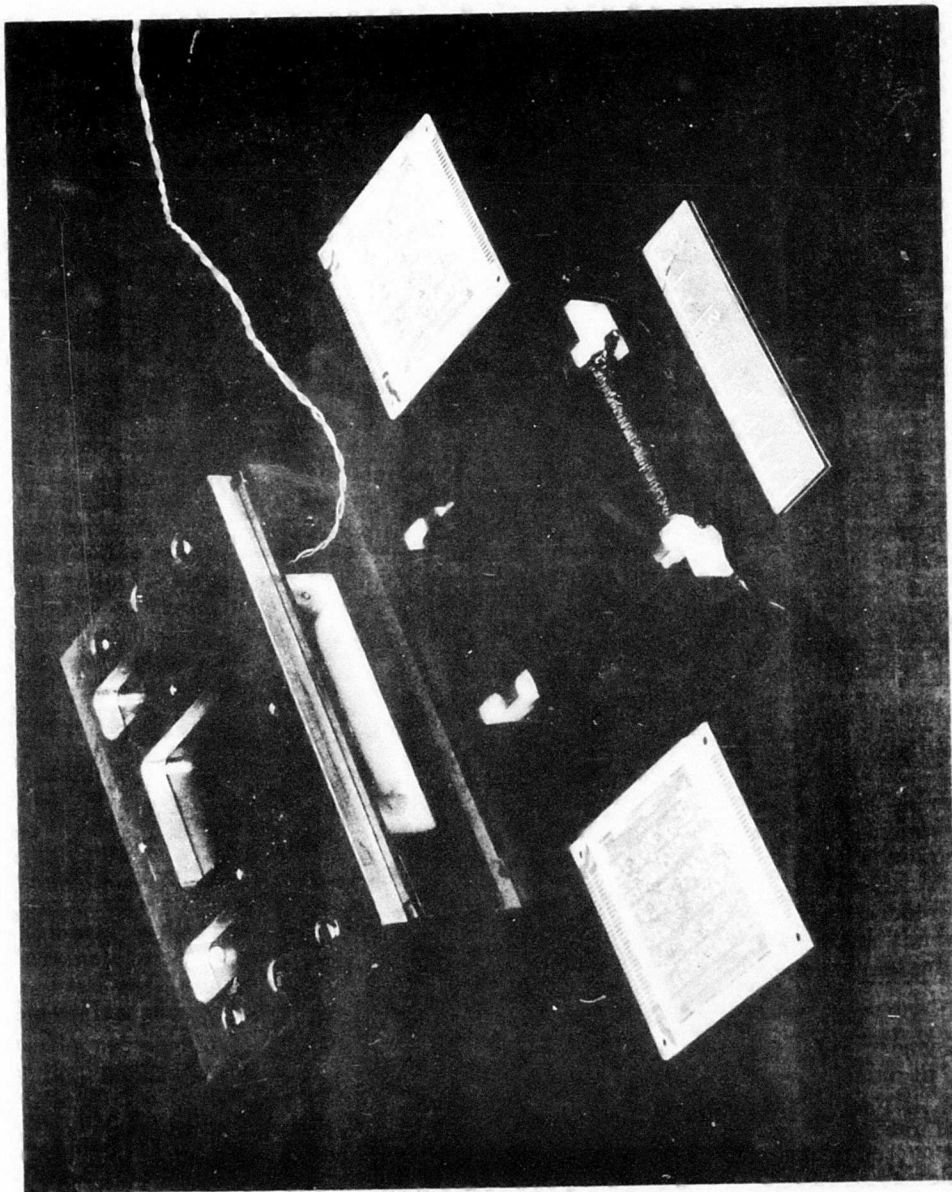


Figure 4-10. Package Concept - 2

## SECTION 5

### DETECTOR STUDY

During the second phase of this program a detector study task was begun to investigate detector element design and electronic techniques in order to improve the sensitivity and reliability magnetic bubble detection. In this section some of the initial results of this study are presented.

#### 5.1 DETECTOR OUTPUT TAILORING

The double-bump output (Figure 5-1) from the conductor shorted chevron detector<sup>8</sup> (Figure 5-2) spans nearly one period in time which is undesirable if one is thinking of multiplexing the outputs of two registers (each propagating consecutive bits) together. The double-bumps arise, by and large, from the uniaxial nature of the chevron which allows the bubble field to be effective in polarizing the structure when sitting at the two end positions. The bubble field, however, is rather short range which means that it will tend to polarize the leg of the chevron it is on more than the other one. This is confirmed by theoretical calculations and means that a magneto-resistance bump due to the presence of a bubble is produced by only half of the chevron. While this is not exactly correct because of accompanying magnetization fall-off in the other leg, it suggests that possibly the detector output could be tailored to produce one bump instead of two, thereby allowing the multiplexing of two registers 180 deg out of phase. As will be seen this can be accomplished by moving the gold shorts of Figure 5-2 into the center of the chevrons as shown in Figure 5-3. While this detector does not work exactly as anticipated it can indeed be used to multiplex registers rotated 180 deg relative to one another.

Extensive magnetoresistance measurements have been made on the conductor shorted chevron stretcher detector shown in Figure 5-3. The output of the detector was measured in a bridge in which the dummy was simply a resistor and in which the dummy was a detector in another register. Measurements were made at both 15 kHz and 100 kHz to determine whether a significant frequency dependence of the output existed. The only observed change could be attributed to the increase in drive-field required to operate at 100 kHz. Figure 5-4 shows the output of the detector at two different drive field values (25 and 40 Oe) showing how the basic double-bump waveform of Figure 5-1 is modified by shorting at the center of the chevrons. The lower plot is for  $H_{\text{drive}} = 40$  Oe and, as will be seen, surprisingly gives the best output when two active detectors are placed in a bridge. The peaks of the double-bump occur when the strip first enters the detector and just leaves it. The second peak is reduced from the first because the current through the detector flows only through the right half of the chevrons and therefore, only a residual output is seen as the strip exists to the left. Figure 5-4 shows that the background magnetoresistance increases relative to that produced by the bubble as the drive field is increased. Figure 5-5 shows the output from a supposedly similar detector cut from the same wafer as that shown in Figure 5-4. Aside from the slight misalignment of the sample in the coil which appears as an unevenness of the background peaks the outputs of both detectors are similar in form. Figure 5-6 shows the the output from each when they are placed in

<sup>8</sup> T.T. Chen, P.K. George, L.R. Tocci, and J.L. Archer, "Study of the Thick Film Chevron Detector," Paper 28-5 presented at the 19th Conf. on Magnetism and Magnetic Materials, Boston 1973.

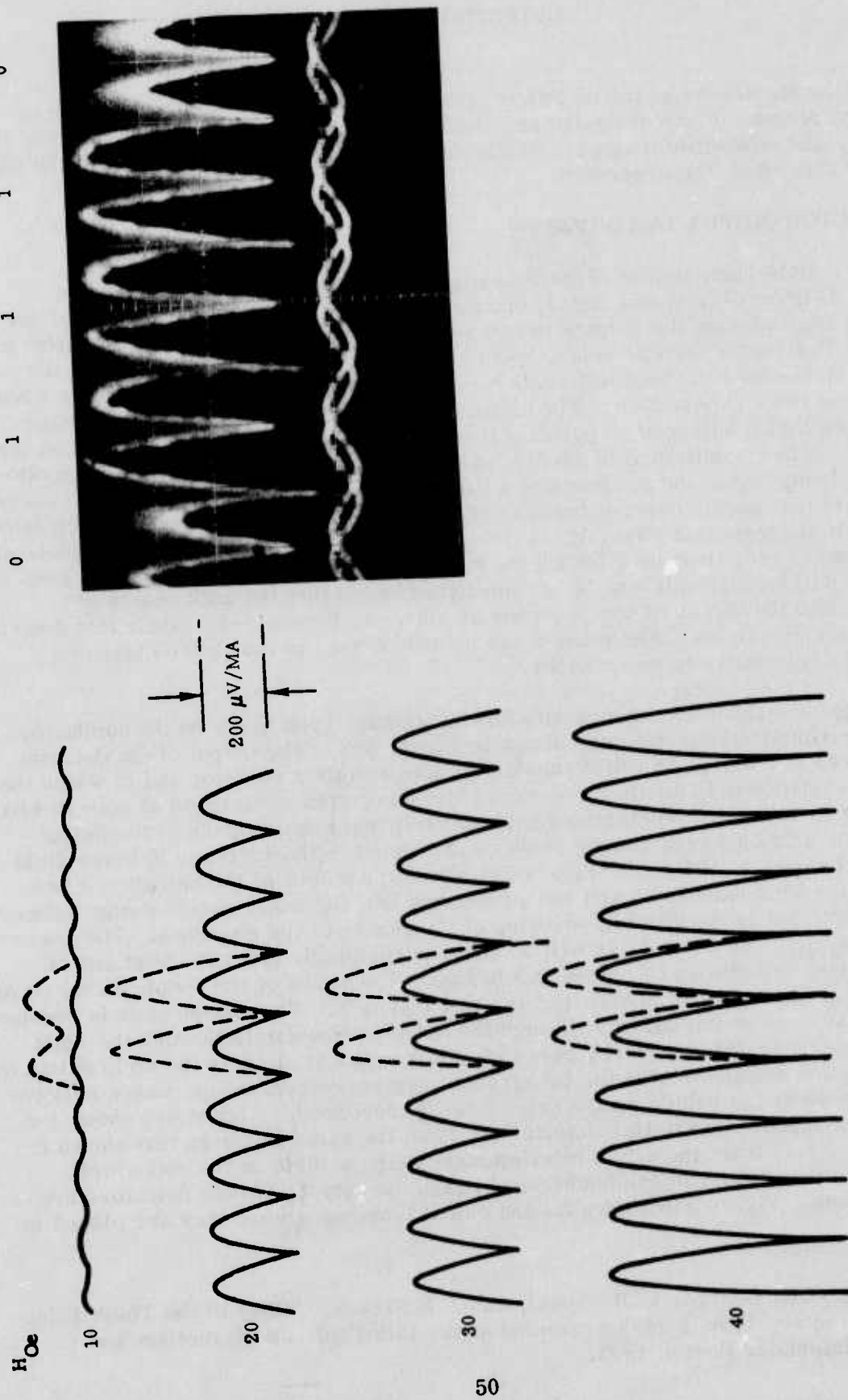


Figure 5-1. Experimental Results for the Conductor Shorted Chevron Detector of Figure 5-2



Figure 5-2. Conductor Shorted Chevron Detector



Figure 5-3. Modified Conductor Shorted Chevron Detector



MODIFIED CONDUCTOR SHORTED CHEVRON  
(REGISTER 1)

~15 kHz continuous  
1.0 + 1.5 amp drive coil 3  
8ma bridge current  $H_o = 25 \text{ Oe}$   
200 $\mu\text{s}/\text{cm}$   
20mv/cm  
amplifier gain 40-50  
 $d\phi/dt < 5\text{mv}$  40 Oe  
30 kHz cut-off

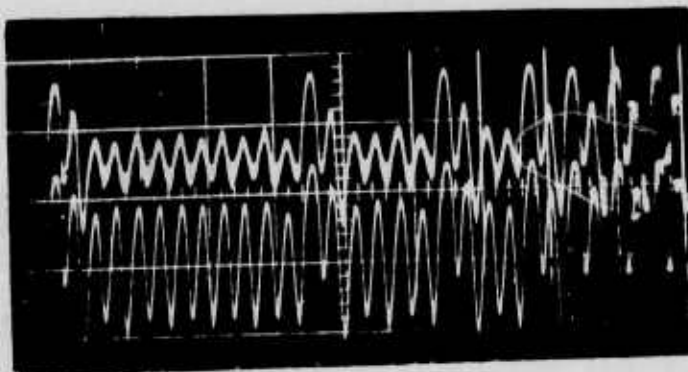


Figure 5-4. Magnetoresistance Output of Modified Conductor Shorted Chevron Detector at Low and High Drive Fields.  
Register One with Carbon Resistor Dummy

MODIFIED CONDUCTOR SHORTED CHEVRON  
(REGISTER 2)

~15 kHz continuous  
1.0 + 1.5 amp drive coil 3  
8ma bridge current  $25 \text{ Oe}$   
200 $\mu\text{s}/\text{cm}$   
20mv/cm  
amplifier gain 40-50  
 $d\phi/dt < 5\text{mv}$  40 Oe  
30 kHz cut-off

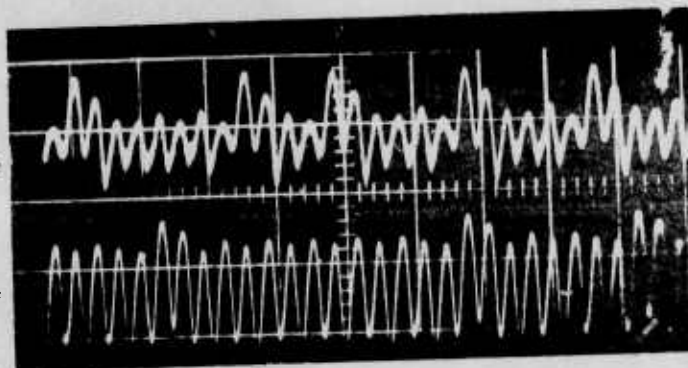


Figure 5-5. Magnetoresistance Output of Modified Conductor Shorted Chevron Detector at Low and High Drive Fields.  
Register Two with Carbon Resistor Dummy

MODIFIED CONDUCTOR SHORTED CHEVRON  
(REGISTERS 1&2)

~15 kHz continuous  
1.0 amp drive coil 3  
8ma bridge current  
200 $\mu$ s/cm  
20mv/cm  
amplifier gain 40-50  
 $d\phi/dt < 5$ mv  
30 kHz cut-off

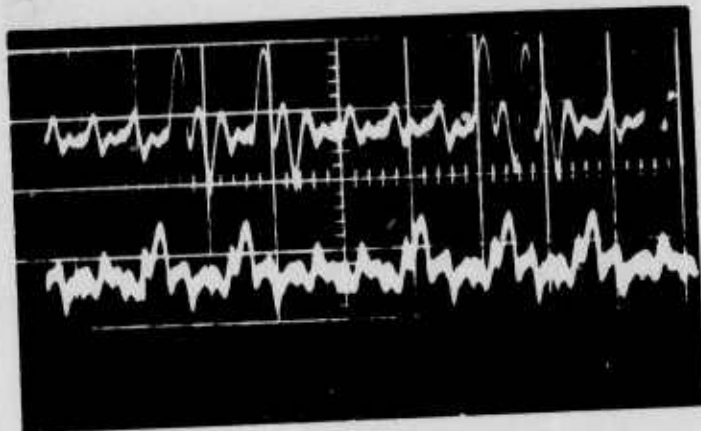


Figure 5-6. Magnetoresistance Output of Modified Conductor Shorted Chevron Detectors (Placed in the Same Bridge) Showing Output Variation Between Detectors of Registers One and Two (Bits are only in one Register at a time)

the same bridge and in the same coil. As can be seen, the output from one register is significantly larger than the other, although the general form of both outputs are quite similar, the difference in form largely being a result of the background magnetoresistance mismatch. If both detectors were exactly matched the small background signal would appear as a straight horizontal line between bit outputs. Figure 5-7 shows that insofar as multiplexed detector goes operation at higher drive fields tends to surprisingly improve the form of the signal output. The lower trace on Figure 5-7 corresponds to 40 Oe while the upper trace to 25 Oe. The signals from the two registers appear of opposite polarity on each of the traces. At 25 Oe drive field the tail of the output of one register produces an opposite going spike (origin unknown) which tends to mask the prominent peak of the other register. As can be seen at 40 Oe this effect is virtually nonexistent principally due to the elimination of the negative going spike (see Figures 5-4 and 5-5) due to the increase in background magnetoresistance. Finally, in Figure 5-8, the output of Registers one and two is shown in a 180 deg configuration in which one register is full and the other only partially full. As can be seen, although there is some interaction between bits in different registers, multiplexed operation appears feasible. The lower signal is that for no bubbles in the registers and represents the magnetoresistance imbalance combined with imbalanced  $d\phi/dt$  noise as these data were taken at 100 kHz using  $d\phi/dt$  noise cancellation.

MODIFIED CONDUCTOR SHORTED CHEVRON  
(REGISTER 1&2)

~15 kHz continuous  
1.0 + 1.5 amp drive coil 3  
8ma bridge current  
200 $\mu$ s/cm  
20mv/cm  
amplifier gain 40-50  
 $d\phi/dt < 5$ mv  
30 kHz cut-off

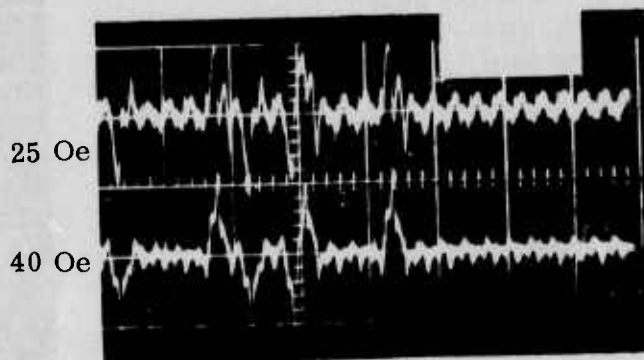


Figure 5-7. Magnetoresistance Output of Modified Conductor Shorted Chevron Detectors (Placed in the Same Bridge) Showing the Output Variation with Applied Field (Bits are in both Registers)

MODIFIED CONDUCTOR SHORTED CHEVRON  
(REGISTER 1&2)

~100 kHz continuous  
1.5 amp drive coil 3  
10 ma bridge current  
20 $\mu$ s/cm  
20mv/cm  
amplifier gain 40-50  
 $d\phi/dt < 5$ mv

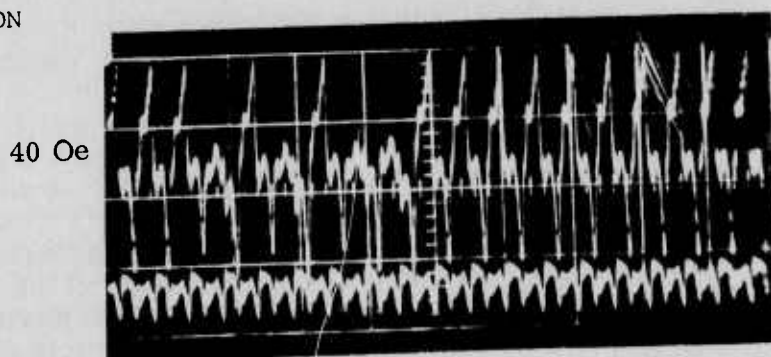


Figure 5-8. Magnetoresistance Output of Modified Conductor Shorted Chevron Detectors (Placed in same Bridge) Showing the Interaction Between Outputs from Different Registers (at High Drive Field). One Register is entirely full and the other only partially full.

## 5.2 DETECTOR SENSITIVITY

The placement of the gold contact leads, as shown in Figure 5-3, is expected to produce some reduction in detector sensitivity because the detector resistance is just about cut in half. In this section we compare the sensitivity of the detector of Figure 5-3 to the full conductor shorted chevron detector, Figure 5-2, to the thick-thin stretcher detector<sup>9, 10</sup> and to two all thick detectors (the fishbone and the one-level zig-zag).<sup>11</sup> Most of the detectors considered had about a 10 element stretch and could carry about 8 ma without seriously disturbing propagation with the exception of the thick-thin detector which was limited to less than 3 ma due to detector heating. The results of this study, based upon measurements made at 5 kHz using the bridge with a dummy resistor, are summarized in Table 5-1. Since some measurements were on detectors with more than a 10 element stretch it has been necessary to correct the data for comparison purposes. Those for which the data are uncertain in the latter sense we indicated by est in the table.

Table 5-1. Detector Sensitivity Study

Detector (10 Element Stretch)	Resistance (period)	Maximum Current	Permalloy Thickness	Sensitivity
Thick-Thin Fishbone <sup>9, 10</sup>	122 (24)	3 ma	300 to 400 Å	475 $\mu\text{v}/\text{ma}$
Two Full Conductor Shorted <sup>8</sup>	75 (28)	8 ma	4000 Å	178 $\mu\text{v}/\text{ma}$
Level Half Conductor Shorted	46 (28)	8 ma	4000 Å	116 $\mu\text{v}/\text{ma}$
One Fishbone <sup>12</sup>	20 (24)	8 ma	4000 Å	50 $\mu\text{v}/\text{ma}$ est
Level Full Zig-Zag <sup>13</sup>	60 (24)	8 ma	4000 Å	120 $\mu\text{v}/\text{ma}$ est

<sup>9</sup> J. L. Archer, L. Tocci, P. K. George and T. T. Chen, "Magnetic Bubble Domain Devices," IEEE Trans on Mag. 8, 695 (1972).

<sup>10</sup> L. R. Tocci, P. K. George and J. L. Archer, "High Speed Characteristics of a Chevron Stretcher Detector," AIP Conference Proceedings 10, 197 (1972).

<sup>11</sup> A. H. Bobeck, I. Danylchuk, F. C. Rossol and W. Strauss, "Evolution of Bubble Circuits Processed by a Single Mask Level" IEEE Trans on Mag. 9, 474 (1973) (Paper 26.1 Presented was slightly different than published version and described a serial register with the outside corner).

<sup>12</sup> W. Strauss, A. H. Bobeck and F. J. Ciak, "Characteristics of a Detection-Propagation Structure for Bubble-Domain Devices," AIP Conference Proceedings 10, 202 (1972).

<sup>13</sup> A. H. Bobeck, "Recent Developments in Magnetic Bubble Technology," presented at the National Meeting of the Electrochemical Society, Houston, May 1972.



As can be seen, the sensitivity of the thick-thin detector is overwhelmingly better than any of the others which is to be expected in view of the higher resistance and lower in-plane demagnetizing factor. Also moving the gold contacts to the center nearly halves the sensitivity of the two-level detector as might be expected on the basis of resistance considerations alone. A similar effect is seen in going from the two-level detectors to the one-level detectors which, due to geometry, have less resistance than their two-level counterparts. Because of the maximum current limitations, however, the thick detectors will have about the same output as the thick-thin fishbone. A thick-thin zig-zag detector should have the highest sensitivity and output of all, we estimate about  $1000 \mu\text{V}/\text{mA}$  on the basis of the one-level results. For interests sake, we are in the process of fabricating such a detector.

## SECTION 6

### BUBBLE MEMORY DEVICES AND EXERCISER

Although no device development was carried out during this phase of the program, several bubble devices are provided to demonstrate the feasibility of the temperature compensated permanent magnet bias structure. First the chip is discussed and operational data taken in a test coil and in the temperature compensated bias structure are presented. Next the bias/drive structure and its characteristics are discussed and lastly the exerciser provided to operate the memory chips is described.

#### 6.1 MAGNETIC BUBBLE MEMORY CHIP

##### 6.1.1 Chip Description

A 10 Kb device (actually 10,240 bits) designed on in-house programs was chosen as the demonstration vehicle. An overall view of the device with inserts showing detailed features is shown in Figure 6-1. The chip size is approximately 200 x 90 mils and the pattern period is 24  $\mu$ m. The device is fabricated on YEuTm<sub>65</sub>GaIG bubble material which has an average temperature coefficient of -0.11 percent/ $^{\circ}$ C over the range 0 $^{\circ}$ C to 50 $^{\circ}$ C (Appendix D).

The main storage region of the device is composed of T-bar propagation elements (see insert Figure 6-1). This pattern design is considered to be a relatively good propagation design and it also has optimum bit density, in this case 10<sup>6</sup> bits/in.<sup>2</sup>. The gaps in the pattern which are 1.5 to 2  $\mu$ m are the most critical dimensions of the pattern. Linewidths are about 4  $\mu$ m. Fabrication of the device is discussed in Para 6.1.2.

Chevron propagation elements are employed in the region where read, write, and erase functions are performed. The generator (write) and the annihilator (erase) circuits are conductor loops located in the gap between chevron columns (insert, Figure 6-1). Annihilation is accomplished by a current pulse which generates a local magnetic field in the center of the loop that adds to the c-c bias field. The bias field is locally raised above the collapse field value, thus collapsing the stripe domain within the loop.

The detector is a conductor shorted thick chevron stretcher<sup>(14)</sup> detector of approximately 15 chevron elements stretch. The conducting path zig-zags through the chevron column providing a longer current path than provided by a fishbone detector.<sup>(15)</sup> A reference detector element is provided which is connected in a bridge configuration with the bubble sensing element in order to provide common

---

<sup>14</sup>T. T. Chen, P. K. George, L. R. Tocci, and J. L. Archer, "Study of the Thick Film Chevron Detector," Paper 2B-5 Presented at the 19th Conf on Magnetism and Magnetic Materials, Boston, 1973

<sup>15</sup>A. H. Bobeck, "Recent Developments in Magnetic Bubble Technology," Presented at the National Meeting of the Electrochemical Society, Houston, May 1972

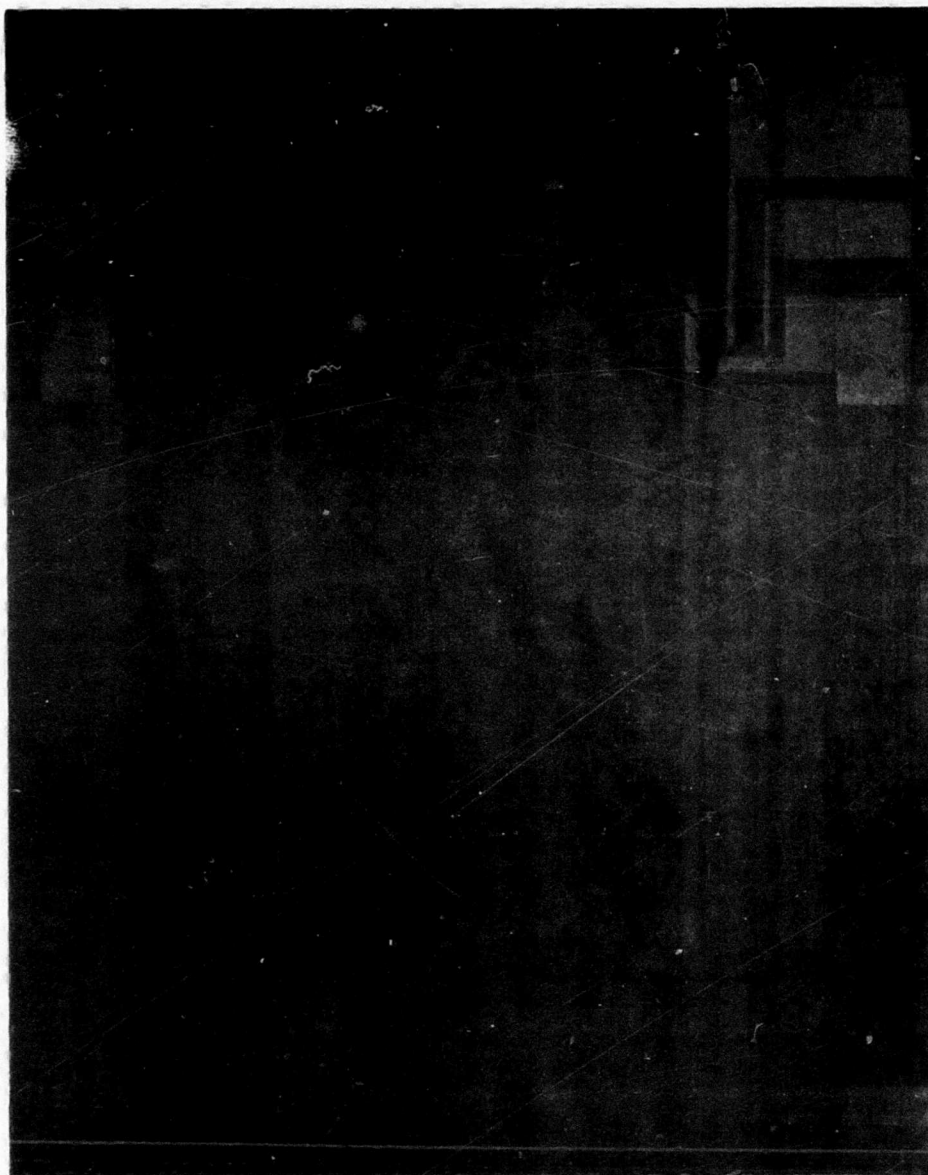


Figure 6-1. 10 K Bit Bubble Shift Register (24  $\mu\text{m}$  Period) (a)

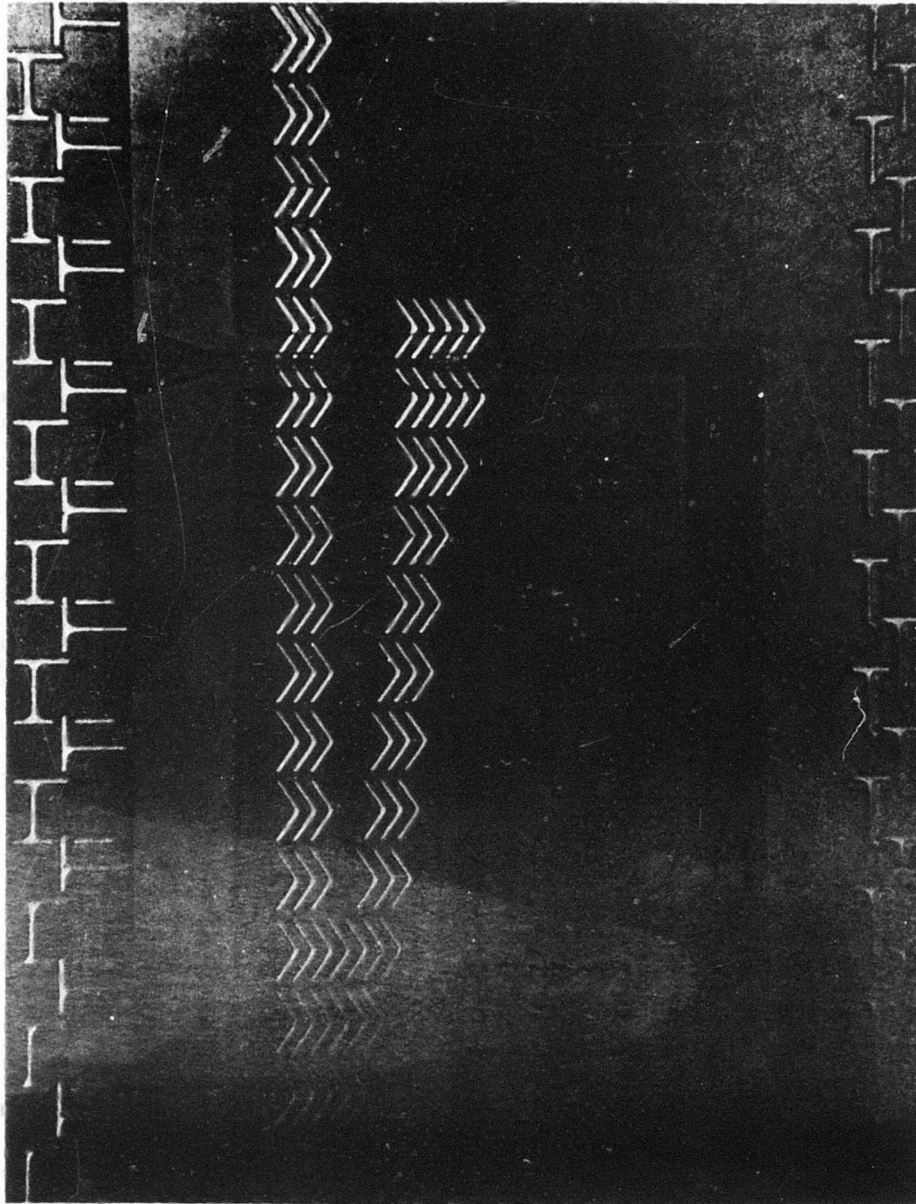


Figure 6-1. (Cont) (b)



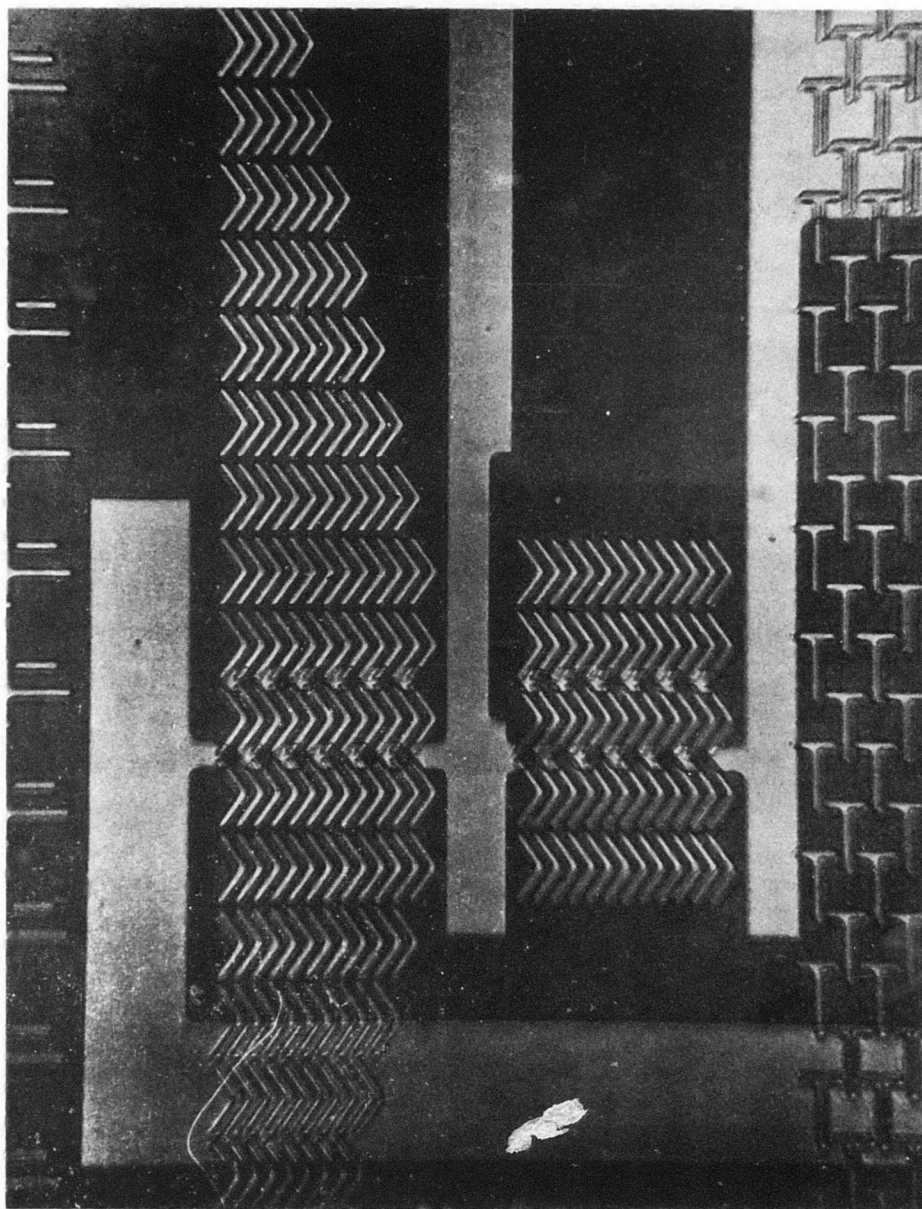


Figure 6-1. (Cont) (c)

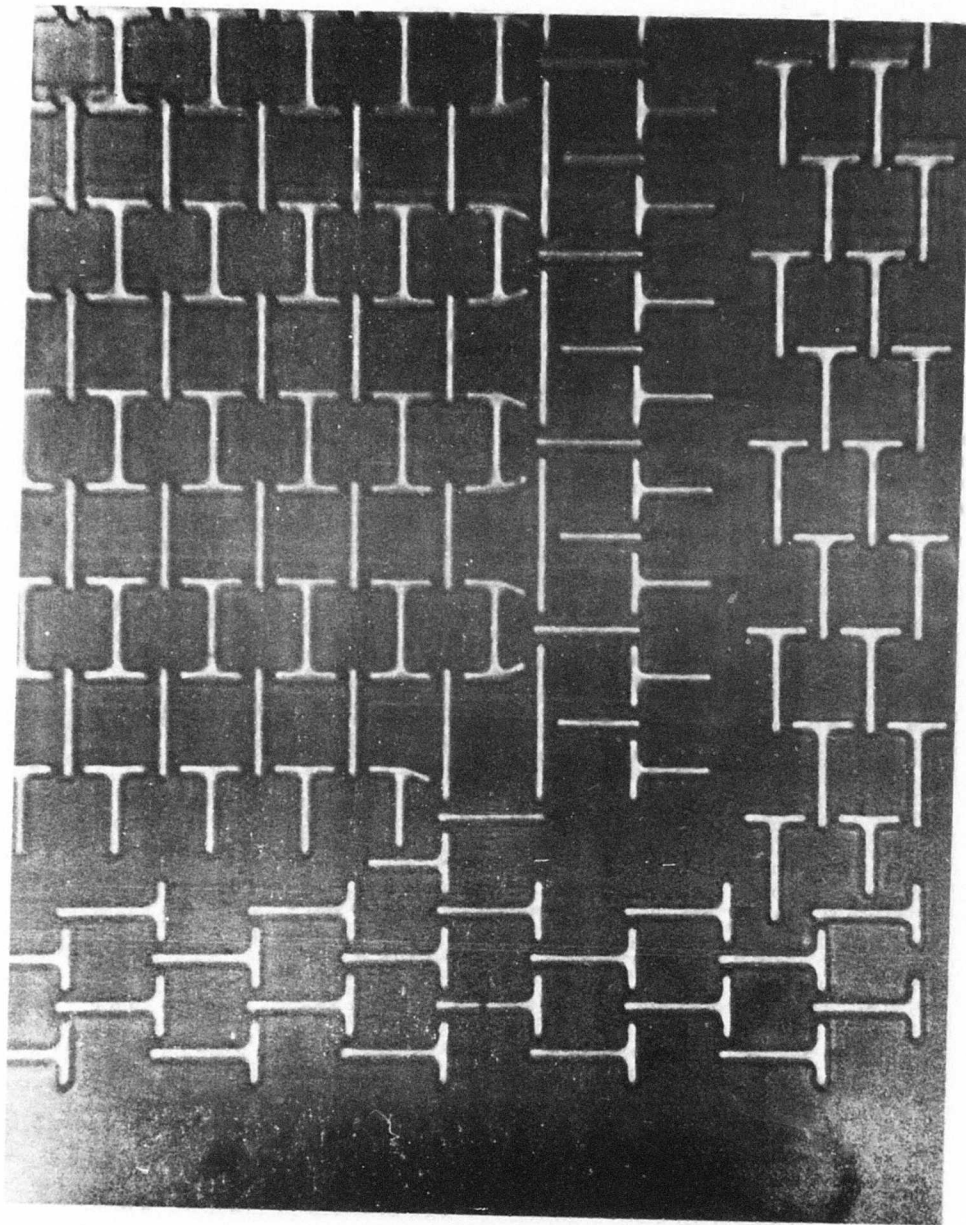


Figure 6-1. (Cont) (d)

mode noise rejection. The bridge outputs are amplified by a differential IC chip amplifier located on the device board (Figure 6-2). A bridge balance input is provided for  $d\phi/dt$  noise cancellation and d-c balancing. A picture of a typical device board with a 10 Kb chip is shown in Figure 6-3. The board is made of common epoxy glass printed circuit board shaped to fit a bias/drive coil structure described in Para 6.2.

Surrounding the entire device is a guard rail comprised of T type propagation elements. These elements are arranged so that propagation is away from the device area. Thus, spurious bubbles outside the device area (possibly generated by edge defects) cannot cause errors in the stored data by migrating into the device area.

### 6.1.2 Device Fabrication

This 10 Kb device is fabricated on garnet using a conductor first fabrication technique. The generator and annihilator conductor circuitry are deposited and defined first directly on the garnet. This conductor level is typically 3500Å thick. An SiO<sub>2</sub> spacer film about 1.2 to 1.4 μm thick is deposited next which decouples the propagation circuit from the bubble field. Next the permalloy (80 Ni-20Fe) propagation pattern is deposited and defined. This layer is approximately 3500Å thick. Finally, another gold conductor level is deposited and defined to provide connection to the magnetoresistive sensor. In order to make connection to the lower conductor level, the SiO<sub>2</sub> layer is partially stripped away. All film depositions are made using the rf sputtering technique. Standard photolithographic techniques are used to define all patterns and chemical etching is used to etch all gold patterns while ion beam milling is used to etch the permalloy pattern.

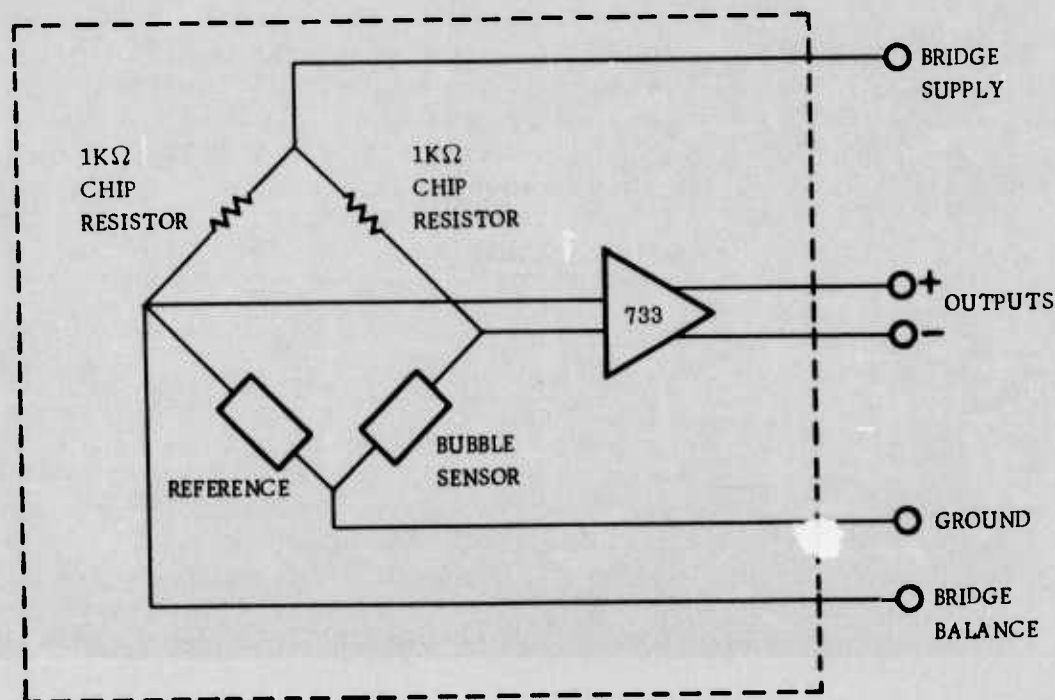


Figure 6-2. Device Board Detector Electronics

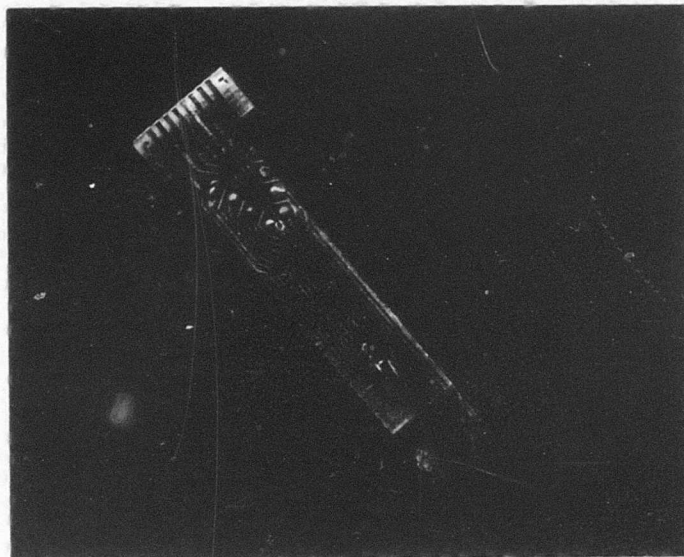


Figure 6-3. Device Board with 10 Kb Chip

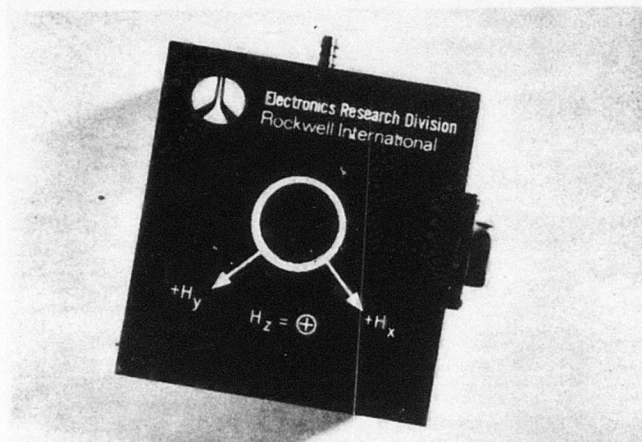
#### 6.1.3 Device Operating Characteristics

Although the EuTm<sub>65</sub> material has been operated up to 200 kHz the intrinsic data rate for this device is 100 kHz and all the following characteristics are taken at this frequency. The primary reason for this is the desire to have a wide operating temperature range. Since the mobility decreases with temperature (Appendix D) the lower temperature end for device operation is determined by mobility limitation. The device is characterized in a drive structure utilizing an electromagnetic Z-bias coil so that the bias field can be conveniently varied (Figure 6-4). (A coil similar to that shown in the figure is provided on this program along with the permanent magnet bias structures.)

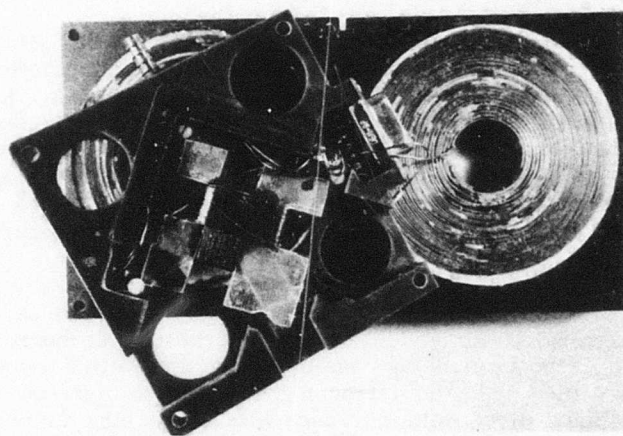
Figure 6-5 shows the consecutive bit propagation margin for several operating temperatures for a typical 10 Kb device. The temperature was monitored with a thermistor that was placed as close as possible to the device in the coil. The temperature was varied by cooled or heated nitrogen gas which was injected in the coil structure. The minimum drive field increases with decreasing temperature which is consistent with the fact that the mobility is decreasing. The bias margin is relatively constant with temperature being about 7 Oe for an in-plane drive field of 40 Oe.

The margin vs temperature for a fixed drive field of 40 Oe is shown in Figure 6-6. The margin closes up very abruptly at about -10°C indicating that the mobility is inadequate with this drive field to provide the required velocity for 100 kHz operation. Also the bubble coercivity is increasing with decreasing temperature which effectively decreases the driving force on the bubble for a fixed in-plane drive field. The center





(a) ASSEMBLED



(b) OPEN

Figure 6-4. Electromagnetic Z-Bias/Drive Structure

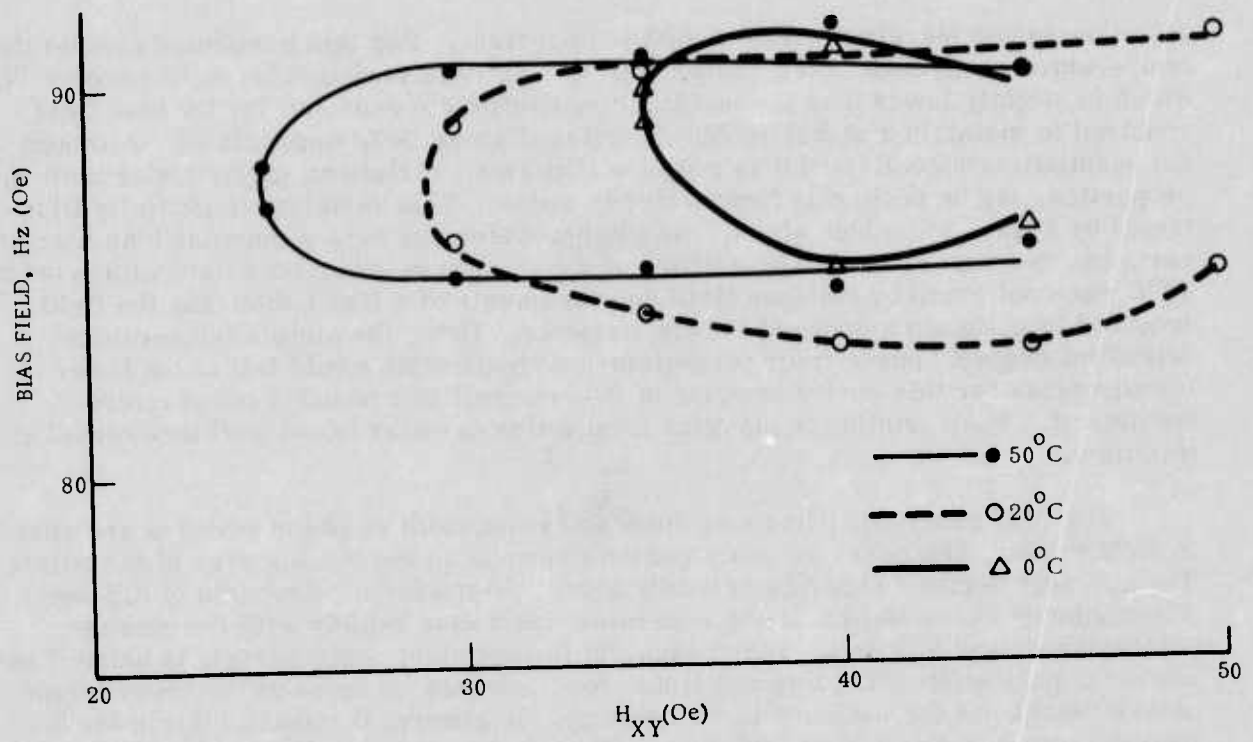


Figure 6-5. Consecutive Bit Propagation Margins

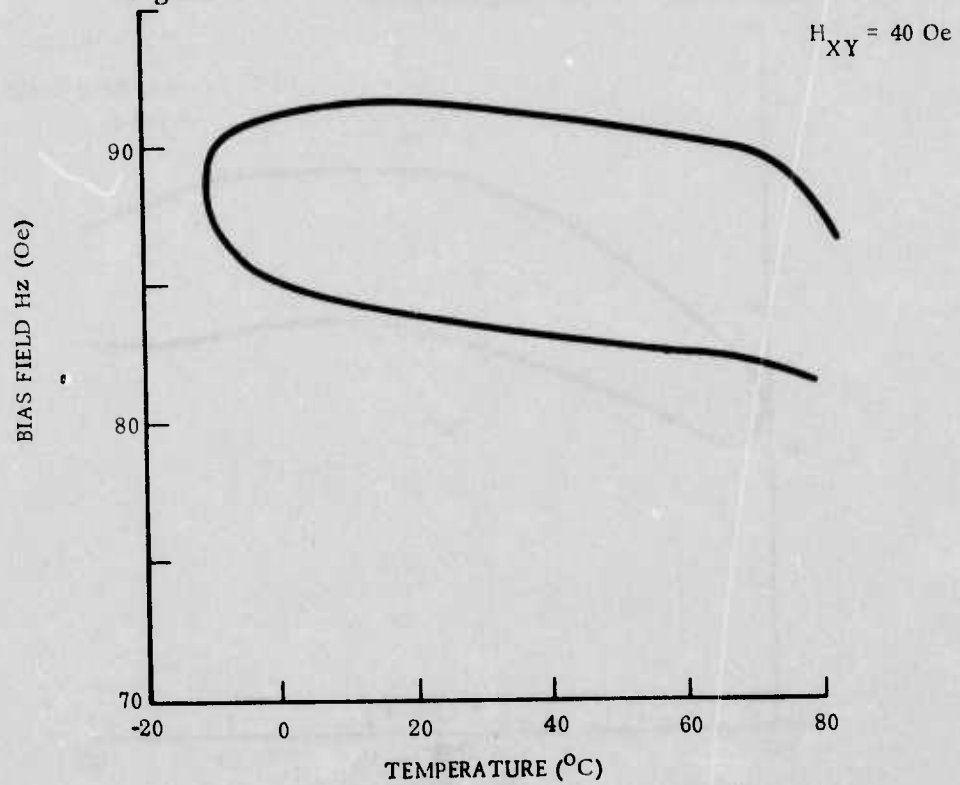


Figure 6-6. Consecutive Bit Propagation Margins vs Temperature ( $H_{xy} = 40$  Oe)

of the operating margin decreases with temperature. For this particular sample the temperature coefficient of the center margin bias field variation is  $-0.07$  percent/ $^{\circ}\text{C}$  which is slightly lower than the temperature coefficient expected for the bias field required to maintain a stable bubble diameter (Figure D-3, Appendix D). Although not quantitatively confirmed it is possible that small variations in particular material properties may be occurring from wafer to wafer. This variation is partially illustrated by Figure 6-7 which shows that another wafer can have a peculiar bias margin variation vs temperature. The shifting of the margin to lower bias field values below  $30^{\circ}\text{C}$  was confirmed by collapse field measurements of a free bubble and the field required to maintain a constant bubble diameter. Using the simple temperature dependent magnet approach for temperature compensation would fail at the lower temperatures for this device because of the reversal to a positive temperature coefficient. The variation in margins from wafer to wafer is not well understood at this time.

The loop generator pulse amplitude and pulsewidth vs phase margins are shown in Figure 6-8. The phase is measured with respect to the leading edge of the pulse. The generator begins to operate reliably above  $250$  ma for a pulsewidth of  $0.5$  sec. The minimum pulse amplitude for generation increases rapidly with decreasing pulsewidth (below  $0.5$  sec). The pulsewidth for optimum phase margin is below  $1$  sec however, pulsewidth and pulse amplitude requirements increase at the lower temperatures because of the increase in wall energy. In general the phase margin for the loop generator is greater than  $90$  deg. Although the pulse amplitude is high the loop generator is a relatively good generator because of its simplicity and reliability. No seed bubble is required for this type generator.

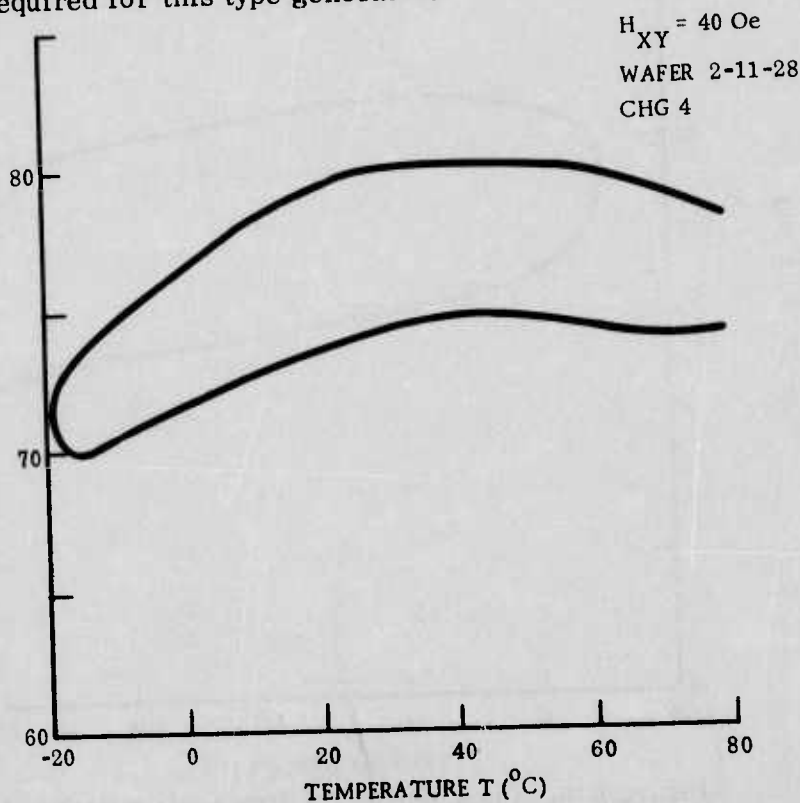


Figure 6-7. Operating Margin vs Temperature of a Device from a Different Bubble Wafer

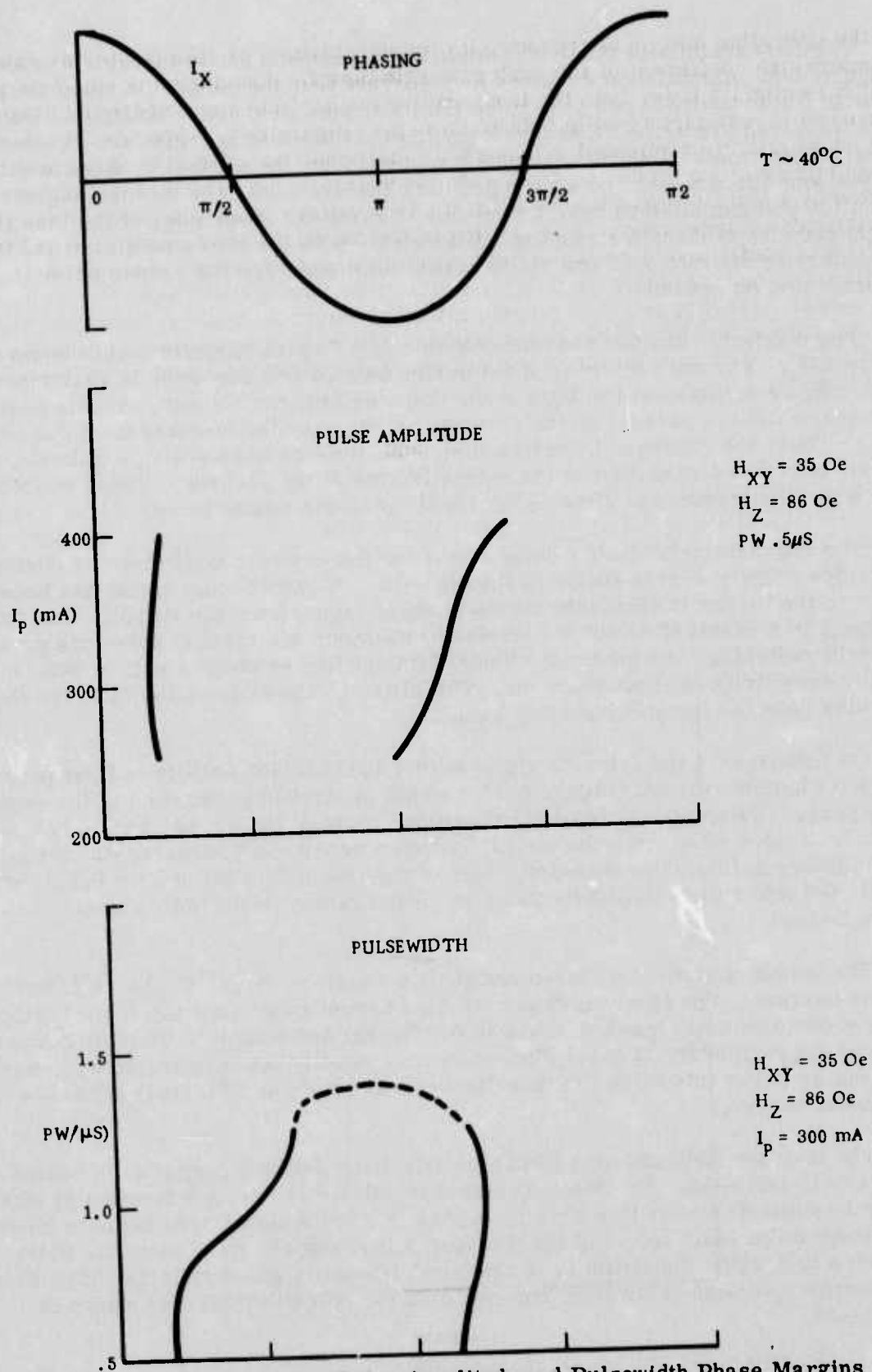


Figure 6-8. Generator Pulse Amplitude and Pulsewidth Phase Margins



The loop annihilator pulse amplitude and pulsewidth phase margins are shown in Figure 6-9. Annihilation requires less current than the generator since the pulse magnetic field required need only raise the local bias field above collapse. Pulsewidths required are around 1 sec or less. Again the phase margins are greater than 90 deg. This type annihilation is much improved over the permalloy (bubble eater) pad type annihilators because no trapped domains exist near the storage region. Permalloy pad annihilators have a tendency to raise the lower edge of the bias field margin because of domain stripping. In general, both the loop annihilator and the loop generator operate over the entire bias field margin for the proper pulse amplitude and pulsewidth.

The conductor shorted chevron detector has a characteristic double bump output (Figure 6-1). For each detector of the bridge by itself, a decrease in resistance occurs when a stripe is at the edge of the detector chevron column. At this position the in-plane field is parallel to the chevron and opposes the in-plane field due to the stripe. Thus, the decrease in resistance of the chevron when a stripe is in the detector is due to a reduction of the magnetization of the chevron. These reductions occur when the stripe is at either edge resulting in the double bump.

The characteristic double bump signal for the detector and reference elements in a bridge (Figure 6-2) is shown in Figure 6-10. A cancellation signal has been applied to the bridge to eliminate the  $d\phi/dt$  noise signal from the output. The remaining signal is a result of detector/reference unbalance and random noise due primarily to domain switching. As the bridge signal is amplified by about a gain of 800, the detector sensitivity is about  $32 \mu\text{V}/\text{ma}$ . The ultimate signal-to-noise ratio for this particular detector is approximately 8 dB.

On Figure 6-11 the detector signal with a 10111001101 pattern is first passed through a clamping circuit (Figure 6-11a) which is strobed at the time of the expected bubble peak. Clamping reduces the background noise at the times when no bubble is expected. It also eliminates the signal drift as a result a-c averaging which depends on the number of bits being detected. The sense amplifier digitizes the bubble signal which is fed into a Data Output Register resulting in the usable logic signal (Figure 6-11c).

The bubble-no bubble difference signal is shown in Figure 6-12 as a function of detector current. The curve is linear for the current range shown. Joule heating effects occur around 15 ma (not shown in the figure) and complete detector burnout occurs at approximately 25 ma. The detector is usually never operated with more than 8 ma as above this value the detector current begins to adversely affect the propagation margin.

The in-plane field and bias field also effect the detector output as indicated in Figures 6-13 and 6-14. The detector signal is relatively flat as a function of bias field up to about 90 Oe for this device. Above this value the stripes begin to shrink (sometimes to bubbles) reducing the detector output signal. Increasing the drive field helps in keeping the stripe fully extended; however, for very large drive fields the chevrons approach saturation thus reducing the detector output as shown in Figure 6-14.

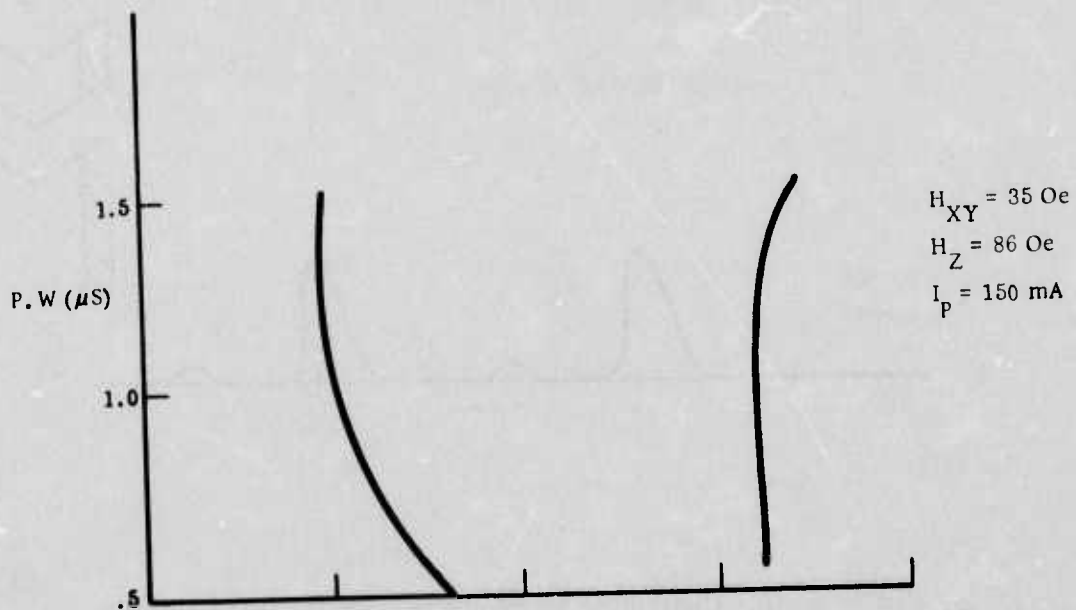
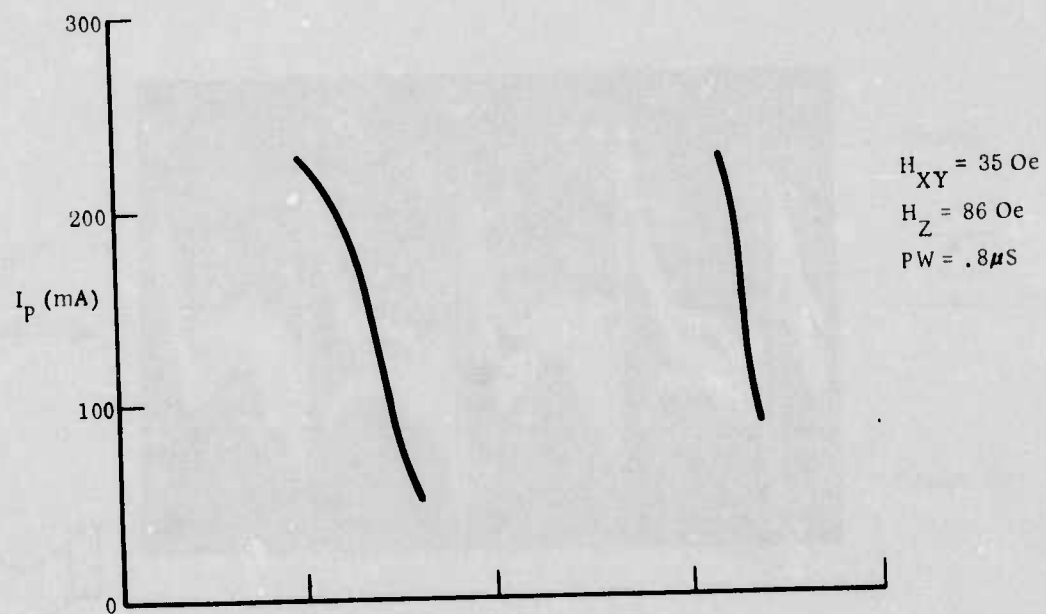
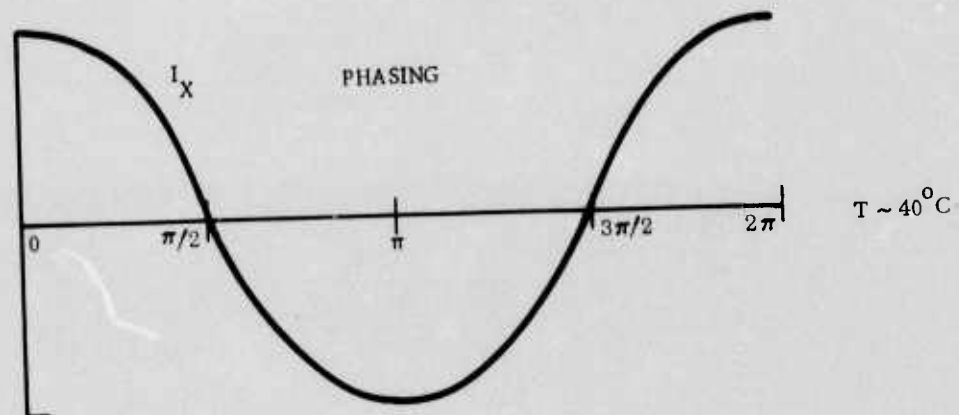


Figure 6-9. Annihilator Pulse Amplitude and Pulsewidth Phase Margins

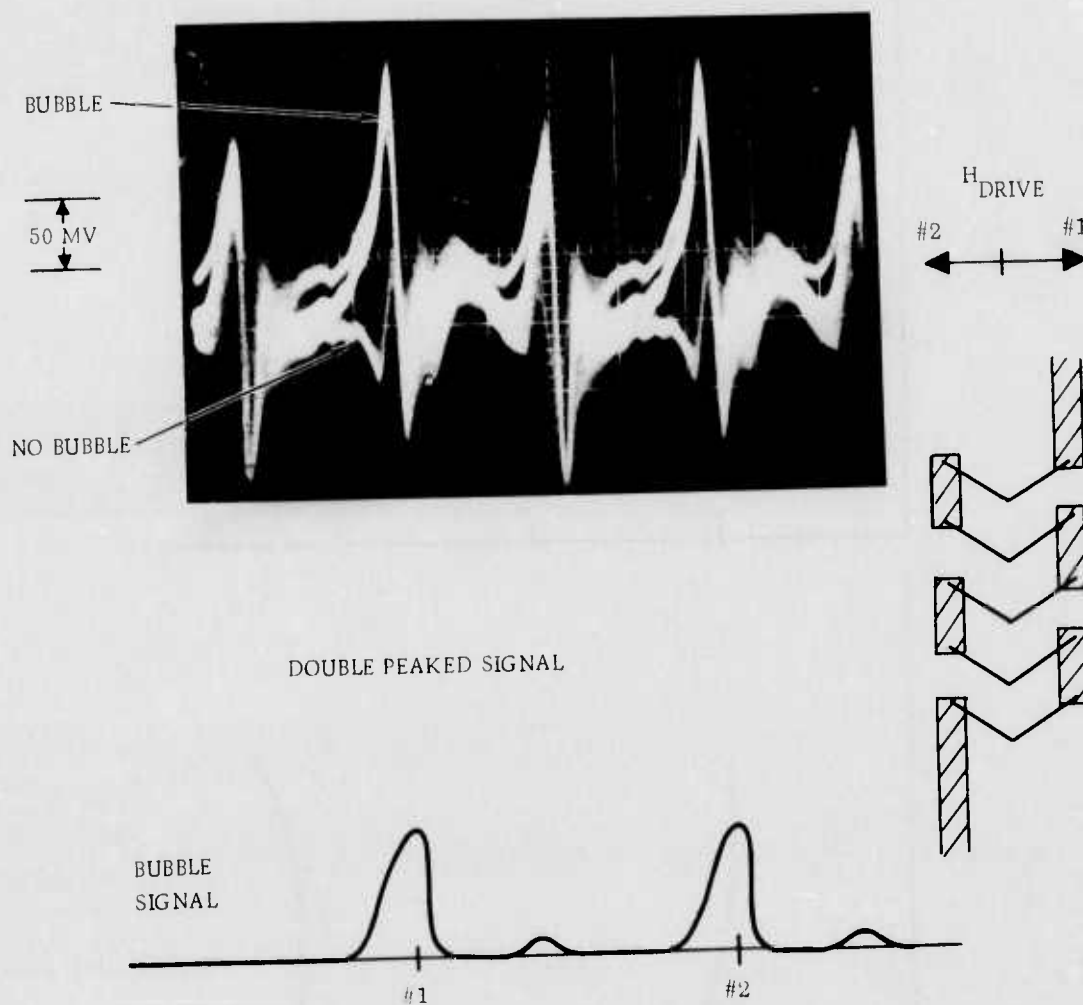
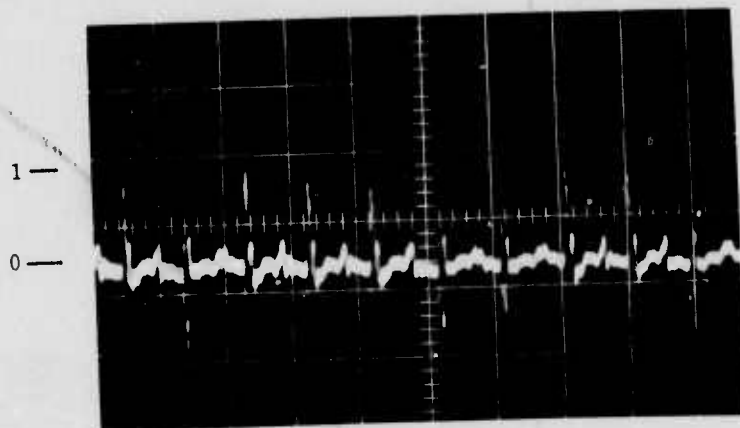


Figure 6-10. Conductor Shorted Chevron Detector Output Signal; Bubble and No-Bubble

PATTERN 10111001101

a. CLAMPED AND STROBED  
SIGNAL

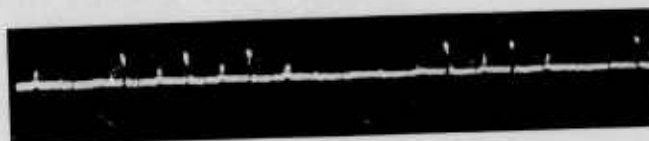
(SENSE AMP 50 MV/DIV  
INPUT X10)



b. SENSE AMP  
OUTPUT

500 MV/DV

1  
0

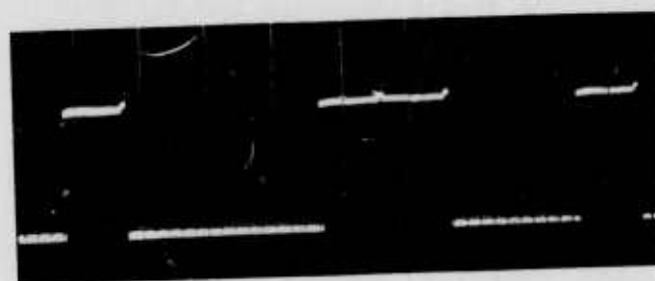


c. DATA OUTPUT

2 V/DIV

0

1



1 0 1 1 1 0 0 1 1 0 1

Figure 6-11. Detector Signal at Various Stages of Signal Processing



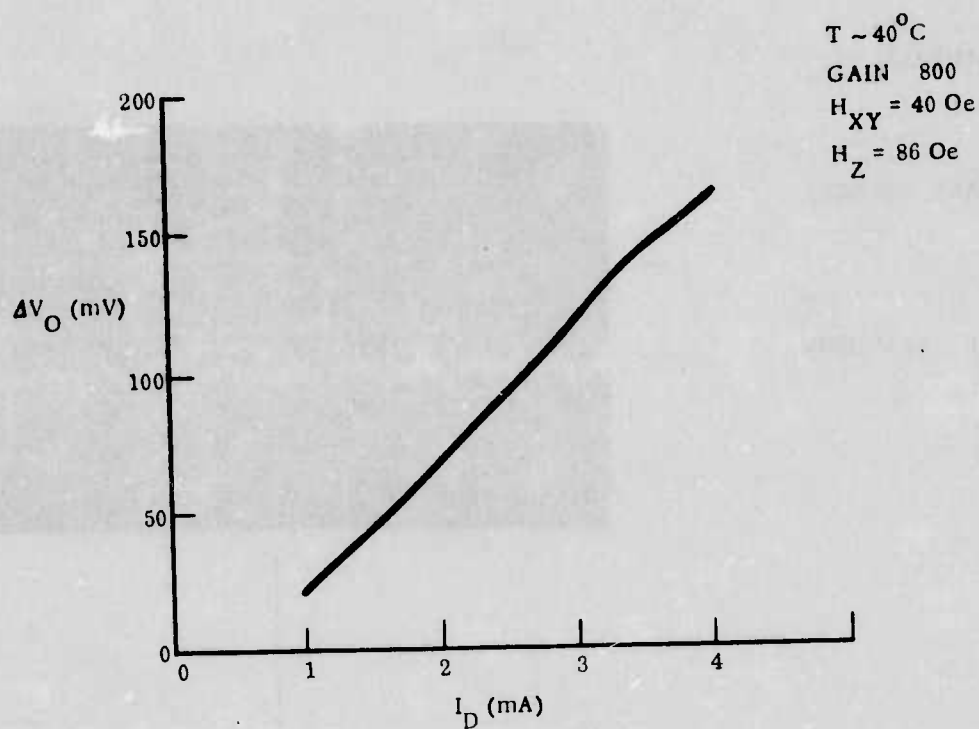


Figure 6-12. Detector Signal vs Current

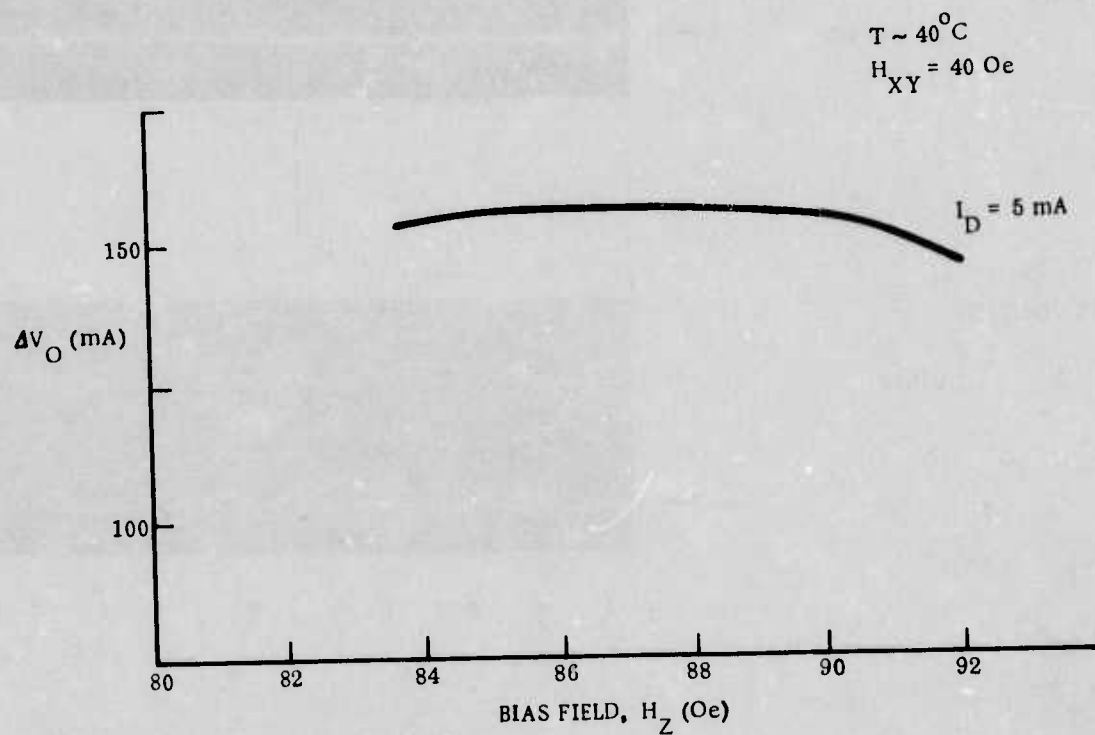


Figure 6-13. Detector Signal vs Bias Field

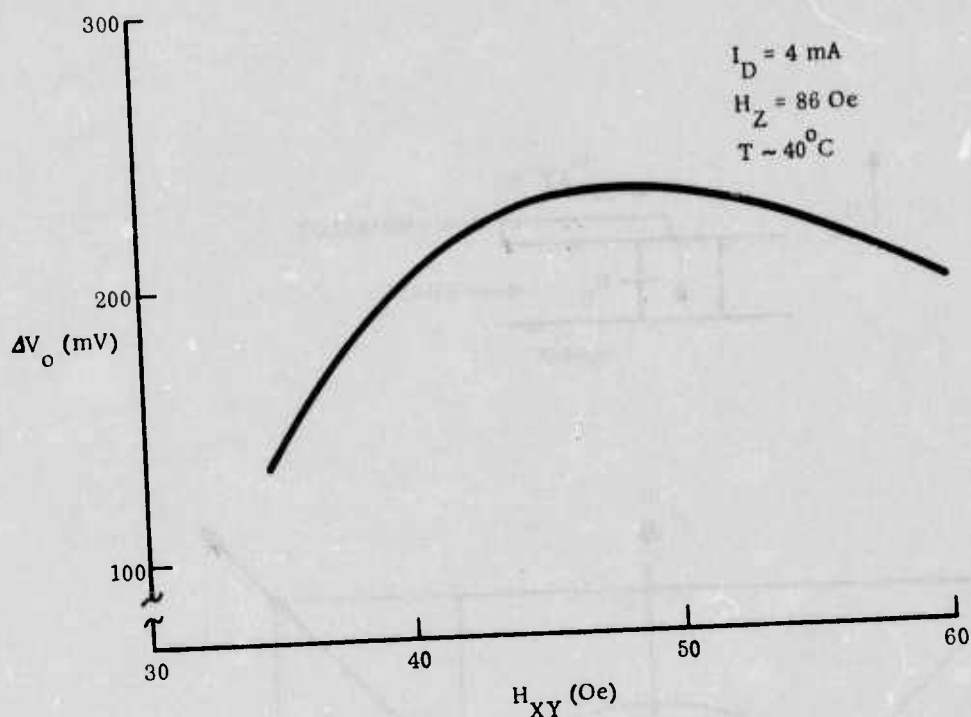


Figure 6-14. Detector Signal vs Drive Field

All the previous characterization results were taken for the device in continuous operation. However, in order to demonstrate non-volatility it is necessary to stop propagation. Certain areas of the pattern however are sensitive to the start-up and shut down field direction. (The start-up and shutdown electronics are discussed in Para 6.3.) The bias margin in this mode is shown in Figure 6-15 vs the start-up and shut-down direction. The largest margin occurs at 0 deg in the figure. No reliable gated device operation is obtained between 90 and 180 deg. The weakest point in the 10 Kb pattern as far as the start-up and shut-down mode is the inside T-bar corner included in Figure 6-15. For the shut-down direction between 0 and 180 deg the bubble must stop at the end of the T near the pusher bar. However, for a bubble stopping at this position it is either collapsed or kicked off the pattern causing errors in the data storage. Another weak point in the pattern is the T-Bar to chevron merge where the bubble has a tendency to move down the diagonal bar of the merge and collapse. Some margin still exists for the field shutting down at 270 deg which puts the bubble in this failure mode.

## 6.2 TEMPERATURE COMPENSATED BIAS/DRIVE STRUCTURE

In this section a temperature compensated bias structure is described which was designed to be used with the  $\text{YEuTm}_{.65}\text{GaG}$  bubble composition (Appendix D). This structure was designed using the principles and methods described in Para 3.3 and Appendices C and F. The rotating field is provided by an orthogonal pair of air core coils. A picture of this structure is shown in Figures 6-16 and 6-17, partially dismantled. This structure was not designed for maximum bits/volume but is designed to demonstrate the feasibility of temperature dependent magnet bias compensation.

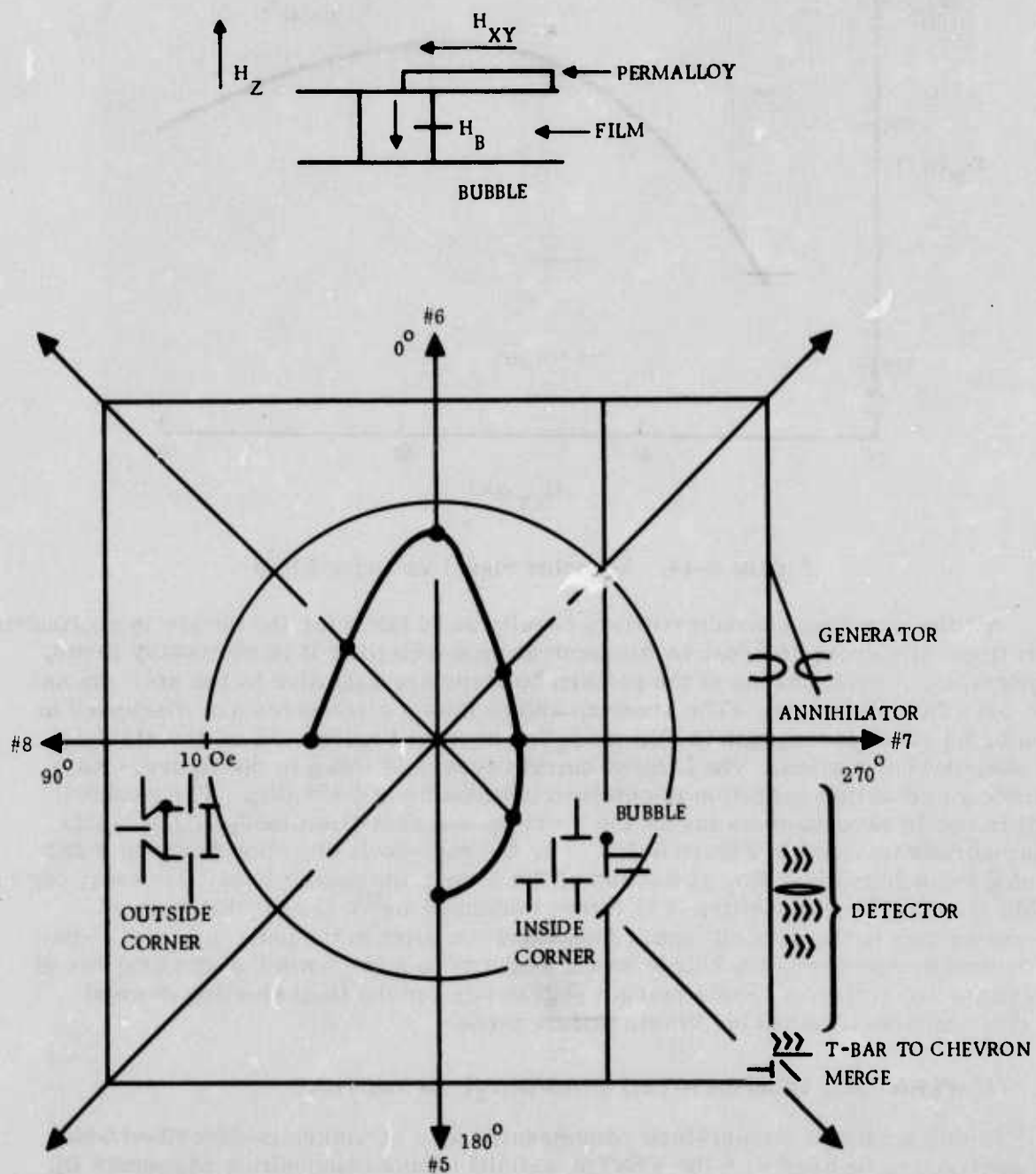


Figure 6-15. Propagation Margin vs Start-up and Shutdown Direction

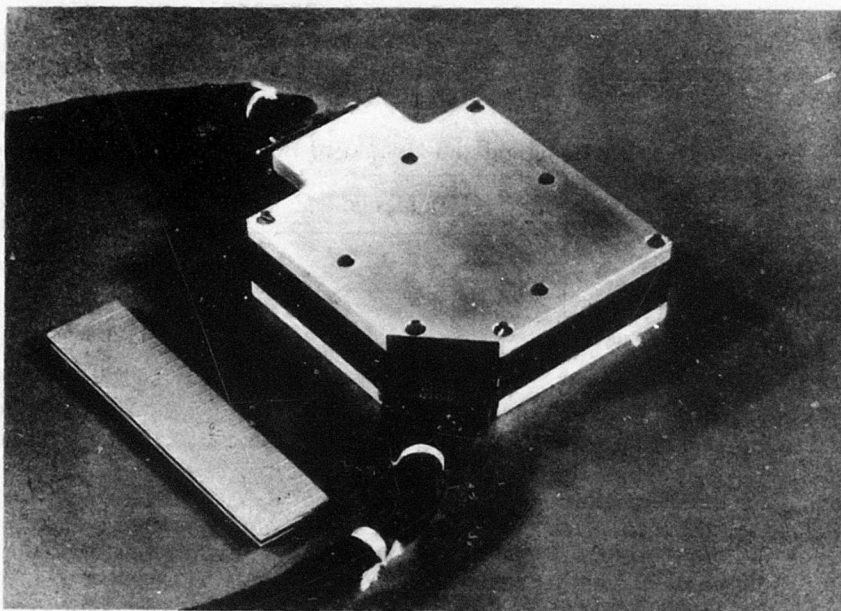


Figure 6-16. PM Bias/Drive Structure

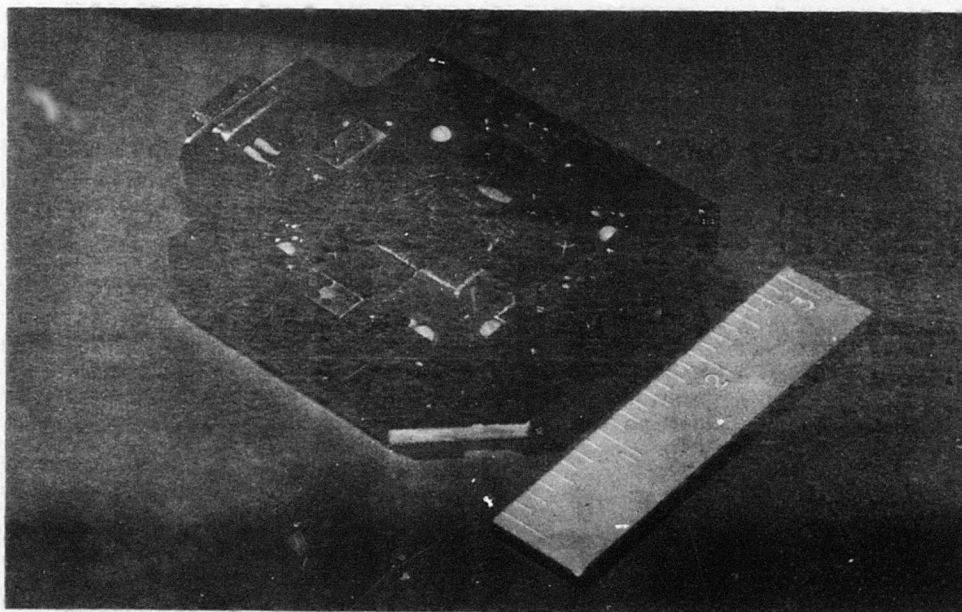


Figure 6-17. PM Bias/Drive Structure with Top Cover and Plate Removed



### 6.2.1 PM Bias Structure

Table 6-1 lists the design coils and measured parameters of the PM bias structure.

Table 6-1. Designed and Measured Bias Parameters

Parameter	Designed	Measured
Bias Field (without shunts)	130 Oe	140 Oe
Coarse Tuning (per shunt)	5 Oe	5.5 Oe
Fine Tuning (12 turns/screw)	7 Oe	7 Oe
Uniform Region	0.25 x 0.25 x 0.25 in. <sup>3</sup>	0.5 x 0.5 x 0.45 in. <sup>3</sup>
Temperature Coefficient	-0.11 %/°C	-0.12 %/°C

The structure dimensions were determined using the results of Appendix F and the methods outlined in Appendix C. From the size of X-Y coil to be used (Para 6.2.2) the plate separation was chosen to 0.5 in. and based on the size of the magnets required for the magnetic field magnitude and uniformity and overall size of the structure was chosen to be approximately 3.3 in.

The bias assembly without the top plate, X-Y coil, and base is shown in Figure 6-18. Four magnets (0.25 x 0.25 x 0.15 in.<sup>3</sup>) located between magnet spacers at each edge of the structure provide the magnetic field. Parallel mu metal plates (0.050 in. thick) on the top and bottom distribute the field and provide uniformity over the device region. Gross shunt plates attached to the sides of each magnet reduce the maximum obtainable magnetic field from 140 Oe to 120 Oe (Figure 6-18). Coarse tuning (shunt pins) and fine tuning (screws) are provided at each magnet location. (Figure 6-18 shows one shunt pin at each location).

The z field variation between the plates is shown in Figure 6-19 for several shunt pin locations. A sketch of the top plate showing the shunt pin locations and numbering system is shown in Figure 6-20. Excluding Curve D which is an extremely unbalanced pin arrangement, the field variation is less than 0.5 Oe over a region  $\pm 0.25$  in. about the sample center. Thus, it appears that the bias field variation is moderately insensitive to the pin arrangement and is in general less than  $\pm 0.6$  percent.

Less important than the uniformity of bias field is the component of the bias field that is in the X-Y plane. Since the in-plane rotating field is 30 Oe or greater as much as 3 Oe ( $\sim 3$  percent) of this component can be tolerated. From Figure 6-21 the maximum in-plane component of the designed bias structure is less than 0.8 percent.

The measured coarse and fine tuning variations are shown in Figure 6-22. Each pin provides about 5.5 Oe coarse tuning. Each screw takes approximately six turns before it penetrates into the field region. After this point the turning sensitivity varies from -0.1 Oe/turn to -0.6 Oe/turn with a total field variation of approximately 3 Oe per screw. Thus, very accurate tuning of the bias field can be obtained using this simple coarse/fine tuning arrangement.

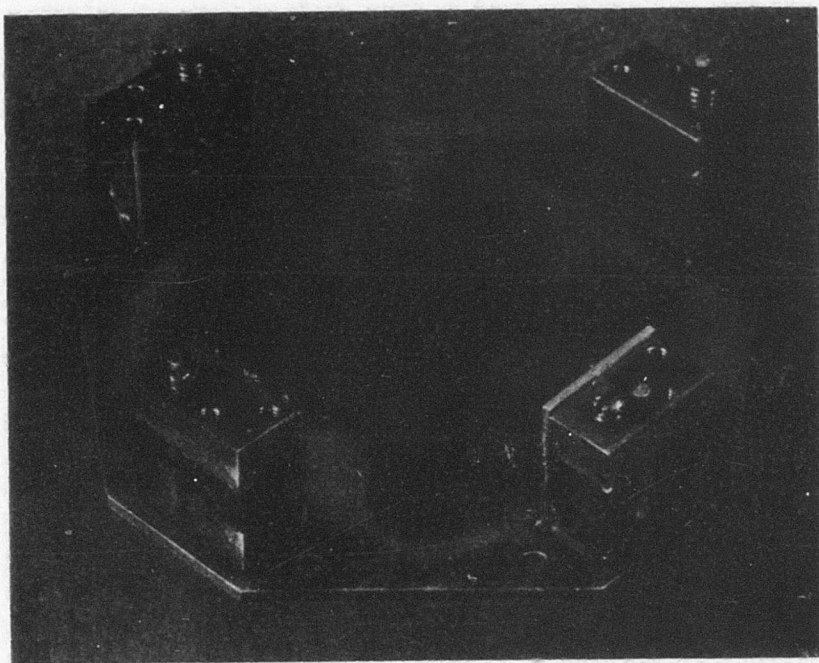


Figure 6-18. PM Bias Assembly With Top Plate

In Para 6.2.2 ferrite plates will be discussed which are used to decouple the X-Y field from the bias plates to improve the high frequency coil characteristics. The plates located between the coil and each mu metal plate have some effect on the bias field variation as shown in Figure 6-23. Scans 1 and 2 correspond to Curves B and E in Figure 6-19 for the bias assembly without these ferrite plates. Although the field variation is now greater with the plates the uniformity is still better than  $\pm 0.4$  percent because the bias field for the same tuning arrangement is higher. Thus, the ferrite plates increase the field sensitivity and additional shunt pins will have to be added to reduce the field.

The ferrite plates also effect the in-plane field component of the bias field, increasing it slightly. However, as indicated in Figure 6-24 this component is still less than 1.5 percent of the bias field and less than the 3 Oe maximum even at the 105 Oe bias field value. Most of the in-plane component occurs at the ferrite plate edge, well away from the device region.

The bias structure employs RARNET rare earth magnets ( $T_C \cong -0.11$  percent/ $^{\circ}\text{C}$ ) to provide the temperature compensation needed to operate a bubble device on  $\text{YEuTm}_{.65}\text{GaIG}$  ( $T_C^{\text{av}} \cong -0.09$  percent/ $^{\circ}\text{C}$ ) over a wide temperature range. The temperature coefficient of the completed PM bias structure is shown in Figure 6-25. The smaller value is probably due to the slight difference in magnet composition over the one measured to obtain the data in Figure 3-8. The device operation using this temperature compensated structure is discussed in Para 6.1.

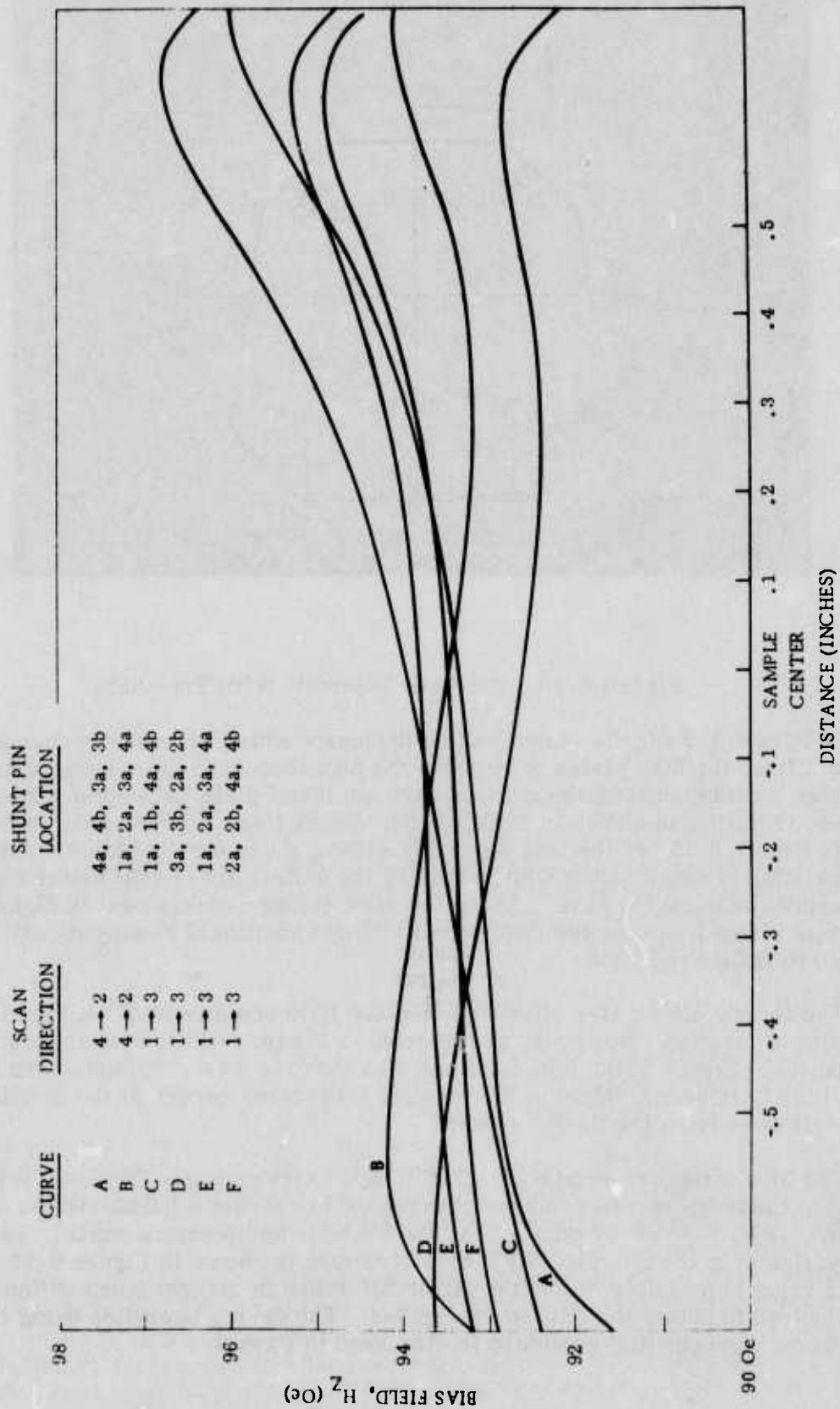


Figure 6-19. Field Variation for Various Shunt Pin Arrangements

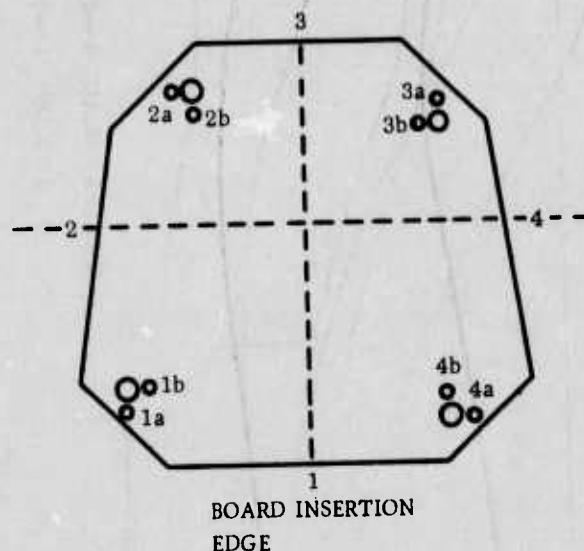


Figure 6-20. Shunt Pin Locations

#### 6.2.2 In-Plane Field Coil

The in-plane field coil is used to provide the uniform rotating field required to actuate the permalloy propagating pattern. Peak magnetic field magnitudes between 25 to 40 Oe must be attainable using the lowest power possible to prevent excessive heating in the coil. In general, the in-plane field is generated by a pair of orthogonal coils driven sinusoidally and 90 deg out of phase. This provides a circularly polarized field over a region near the center of the coil. As no sophisticated packaging is required in this phase of the program an air core coil of moderate size is used which accepts a printed circuit board carrying the bubble device through an opening in the coil windings (Figure 6-17).

Table 6-2 lists two types of air core coils and their parameters. These coils are 1/2 in. in width, with both solid windings and spaced windings for visual access. For the device board used these coils are about the smallest that can be used and still achieve field uniformity over the 10 Kb device area. The smallest coil is desirable to minimize losses at high data rates and to minimize the coil inductance which keeps the current precharge time for coil start-up small.

The field uniformity of the planar components of the in-plane field are not critical since small variations (e.g. < 4 Oe) will usually not effect device operation depending on the initial operating point. The directional uniformity of these in-plane component is also not critical as long as the in-plane field is circularly polarized. Although the effects of elliptically polarized field have not been quantified, some margin degradation occurs especially if the ellipticity is a result of non-orthogonality



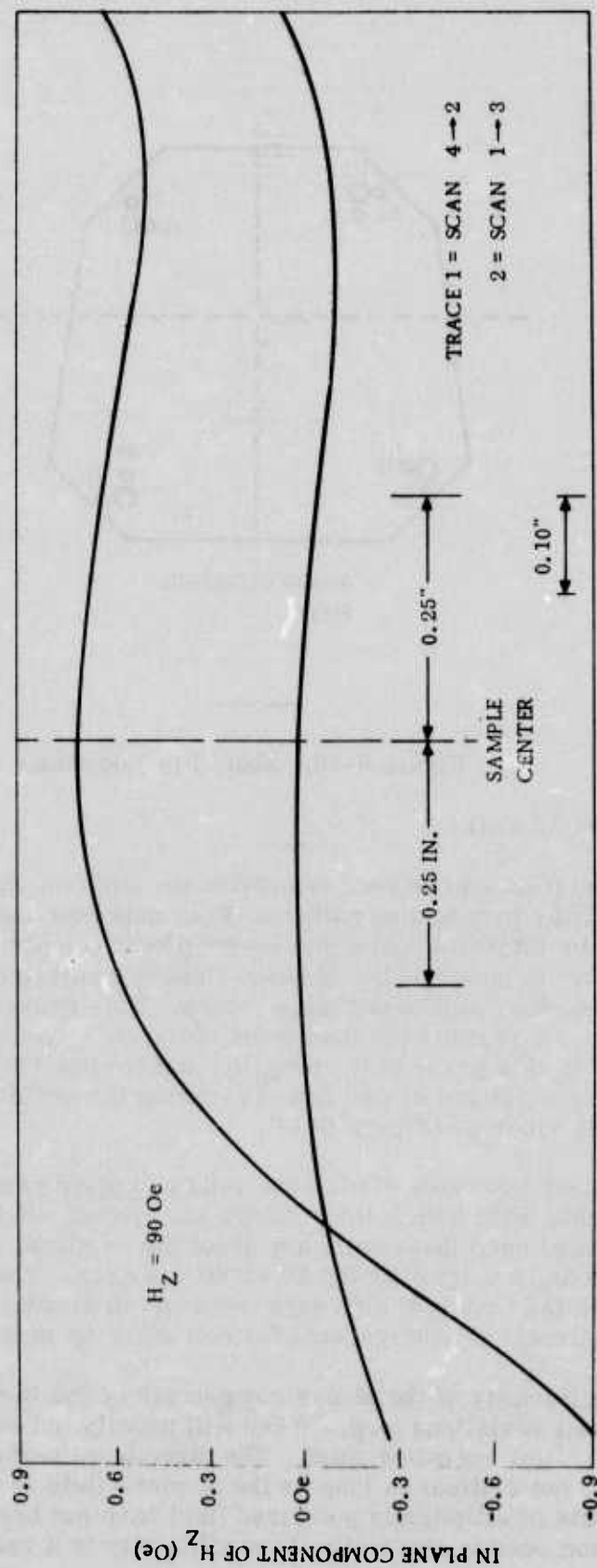


Figure 6-21. In-Plane Field Component of the Bias Field

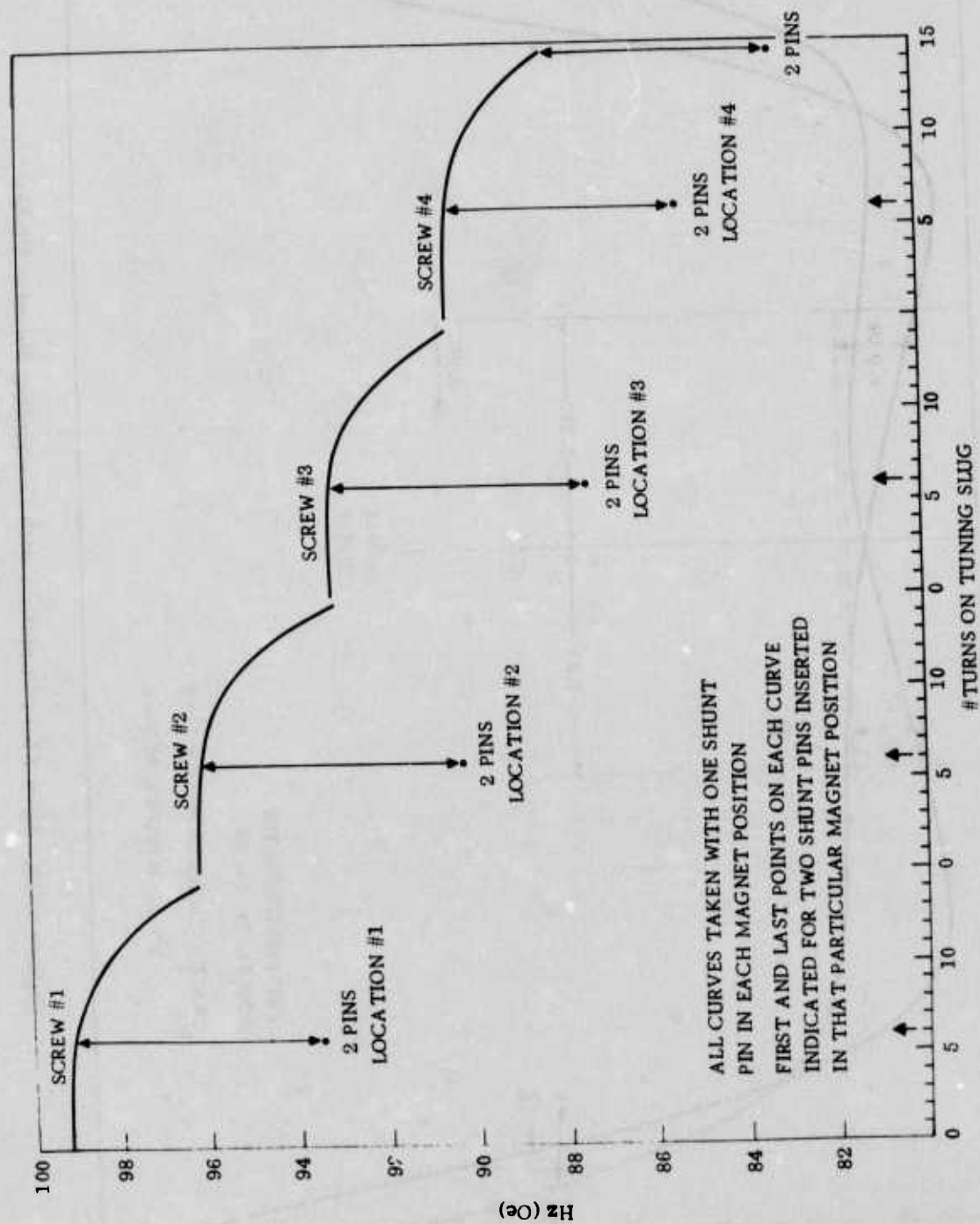


Figure 6-22. Coarse/Fine Tuning

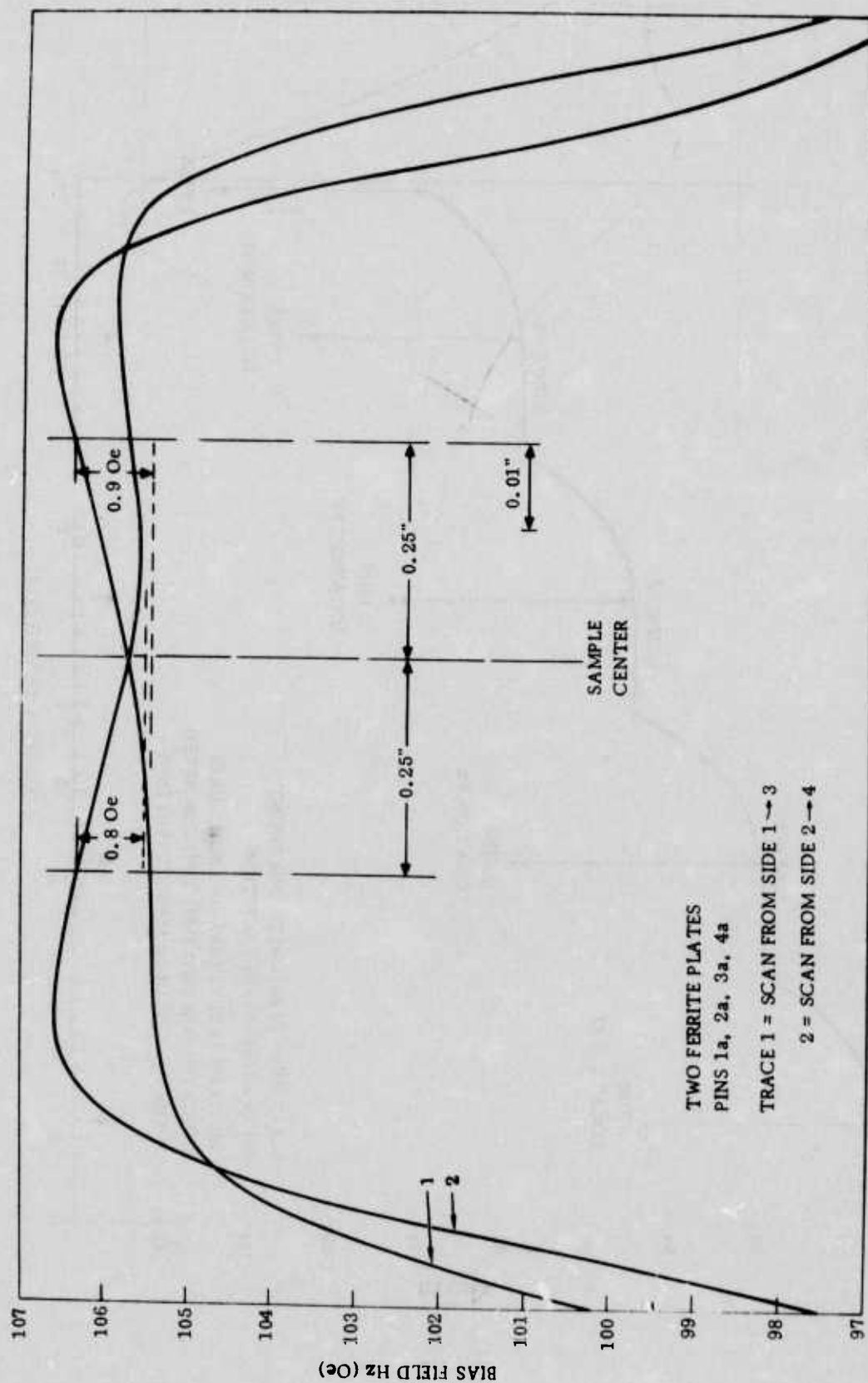


Figure 6-23. Bias Field Variation with Decoupling Ferrite Plates

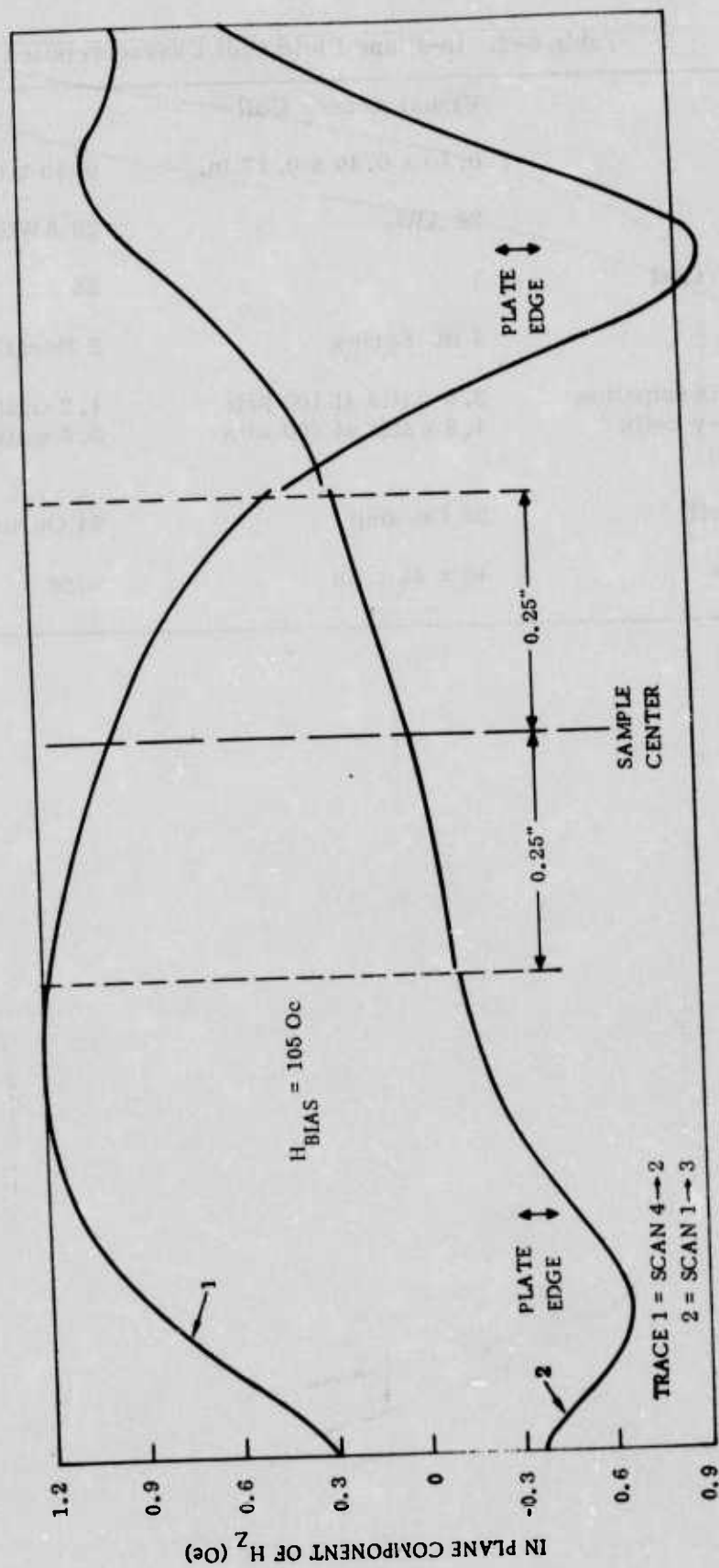


Figure 6-24. In-Plane Component of the Bias Field with Ferrite Plates



Table 6-2. In-Plane Field Coil Characteristics

	Visual Access Coil	
Dimensions	0.40 x 0.40 x 0.17 in.	0.40 x 0.40 x 0.13 in.
Wire Gauge	28 AWG	28 AWG
Turns/Layer/Coil	7	28
Layers/Coil	4 in. Series	2 Parallel
Total Power Dissipation at $H_D = 40$ (x-y coils continuous op)	2.0 watts at 100 kHz 4.8 watts at 400 kHz	1.2 watts at 100 kHz 3.6 watts at 500 kHz
Sensitivity/Coil	20 Oe/amp	24 Oe/amp
Aperture Size	45 x 45 mils	none

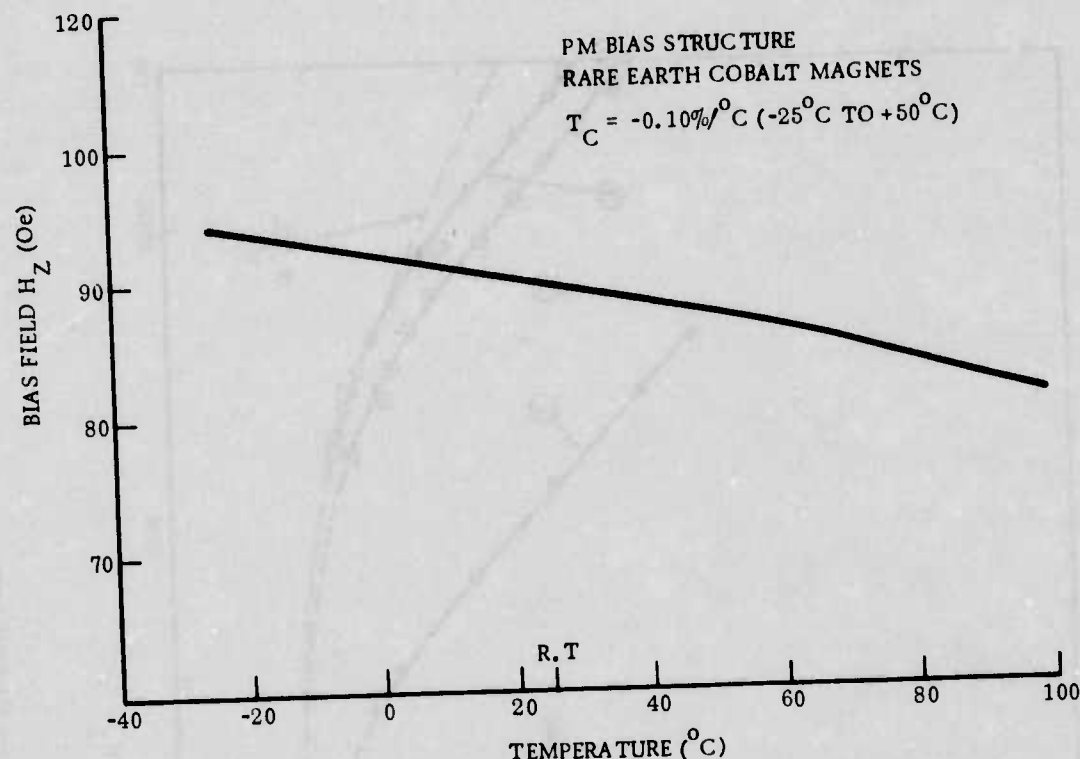


Figure 6-25. Temperature Variation of this PM Structure Bias Field

of the in-plane field components. The most critical variation associated with the in-plane field coil is the z-component caused by a tilting of the in-plane field with respect to the bias field or the device plane. In any case this sinusoidally varying component can severely degrade the operating margin because of its sensitivity to the z directed bias field. For an in-plane field of 30 Oe a 6 deg tilt can cause as much as  $\pm 3$  Oe variation in the bias field reducing the operating margin by 6 Oe.

In the PM drive structure provided on this program ferrite plates are placed between the in-plane coil and bias plates. The ferrite plates decouple the high frequency in-plane field from the magnetic ferrous plates and decrease the losses at high frequencies due to hysteresis effects. Figure 6-26 shows the magnitude of the coil impedance for several conditions. Curve (1) is the impedance magnitude for the untuned coil not assembled in the bias structure. Above 3 kHz the impedance begins to rise rapidly due to the inductance and other frequency dependent losses.

In practice the coils are operated in resonance in order to reduce the voltage requirements of the generator source. Starting and stopping of the rotating field in the resonance mode can still be accomplished in a controlled manner as discussed in Para 6.3.

Curve (2) is the impedance for coil with the inductance tuned out by a parallel capacitor. The impedance remaining is due to coil losses and contributes to coil heating. These losses begin to rise rapidly after 100 kHz and are not solely due to the skin effect since these losses rise faster than  $f^{-1/2}$ . The losses also contain

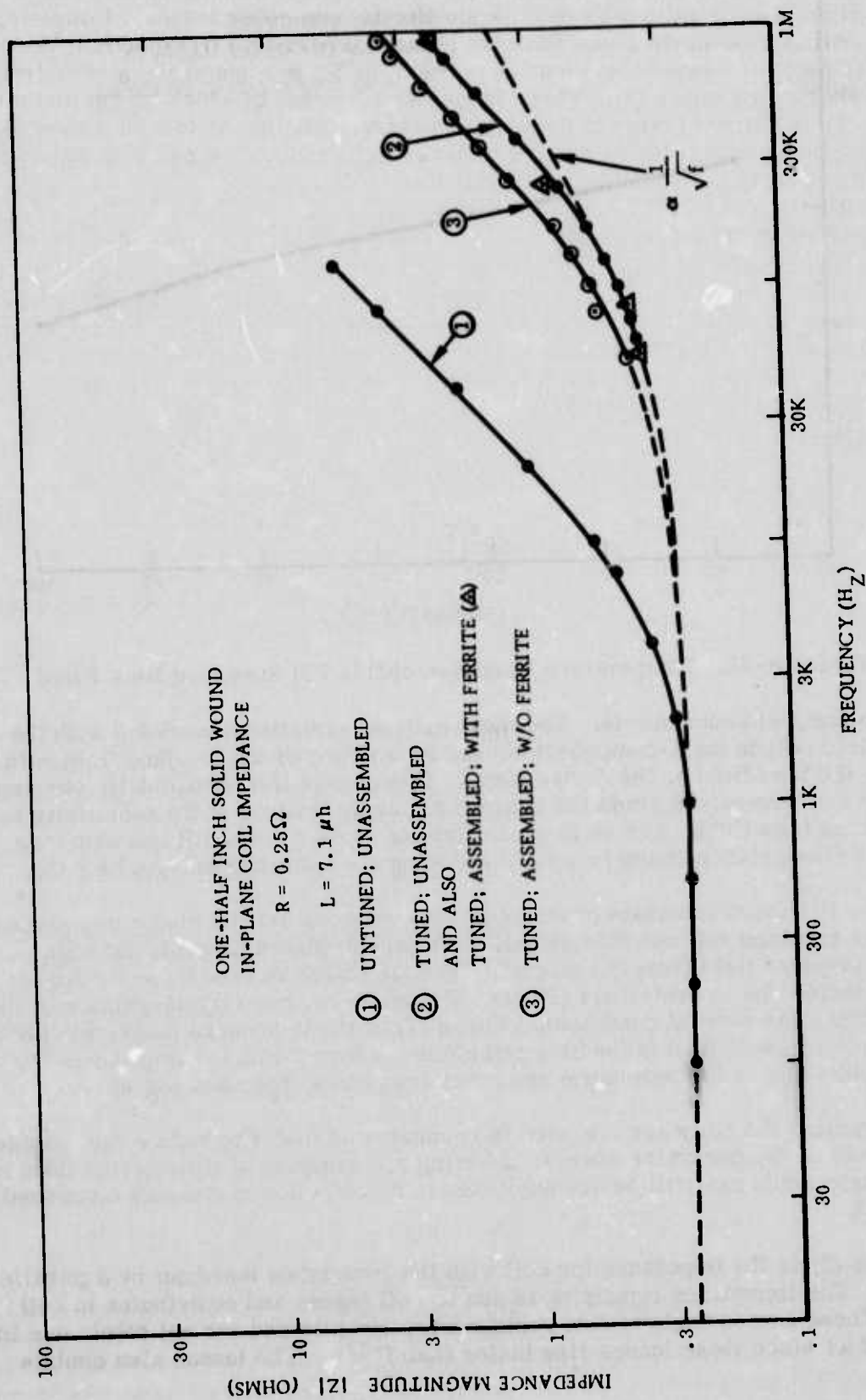


Figure 6-26. Coil Impedance vs Frequency

components due to coupling between the layers of one coil winding which results in a redistribution of current in the windings similar to skin effect losses. However, when the coil is assembled in the PM bias structure (without ferrite plates) the coil power dissipation increases by about 40 percent to 50 percent at the higher frequencies as indicated by Curve (3). These losses are a result of eddy current and magnetic losses in the mu-metal plates of the bias structure. Adding the ferrite plates effectively decouples the coil field from the plates which reduces the coil impedance to that obtained for an unassembled tuned coil (Curve 2).

### 6.3 BUBBLE MEMORY EXERCISER

The bubble domain memory exerciser provided on this program was developed on in-house programs. It is designed to be versatile and usable for future generation bubble device characterization and exercising. The unit uses modular design having three basic modules which are the following:

1. Timing Generator
2. Data Processor
3. Interface Unit

Refer to Figures 6-27, 6-28, 6-29 and 6-30 for front panel layouts and general block diagram. A picture of the exerciser is shown in Figure 6-31.

#### 6.3.1 Timing Generator

The timing generator will generate four sine wave voltages 90 deg apart and generate four clock phase gates from the zero voltage crossings of two of the sine wave voltages and also generate a clock pulse at each sine wave zero voltage crossing time. For manual rotation of the x-y field, the outputs of a sine-cosine potentiometer are selected to provide two of the sine waves and unit gain operational amplifier inverters provide the other two. For rotation of the x-y field at 1 Hz to 100 kHz in five decade ranges, the outputs of two phase locked integrated circuit sine wave generators are selected. These sine waves are produced by diode function generator modification of triangular waves generated by charging and discharging capacitors with constant current generators. The sine waves are phase locked 90 deg apart, using a digital phase detector to compare the control flip-flop output of one sine wave generator with a zero crossing detector operating from the other and using the integrated phase detector output to control the constant current control input of one of the sine wave generators. For rotation of the x-y field at 100 kHz to 1 MHz in two ranges, the buffered outputs of two series tuned LC circuits (excited by zero crossing detectors operating from the LC circuit outputs) are selected. Automatic gain control circuitry is used to maintain the amplitudes of the buffered, tuned circuit voltages at the same amplitudes as those from the sine-cosine potentiometer and from the integrated circuit sine wave generators.

The four clock phase gates are generated by decoding the outputs of zero crossing voltage level detectors operating from two of the sine wave voltages 90 deg apart. The clock pulses are generated by firing univibrator circuits at the appropriate transitions of the decoded output voltages. A combined clock pulse, which operates at four times the sine wave (or rotating field) frequency, is produced as an "or" function of the four individual clock pulses.



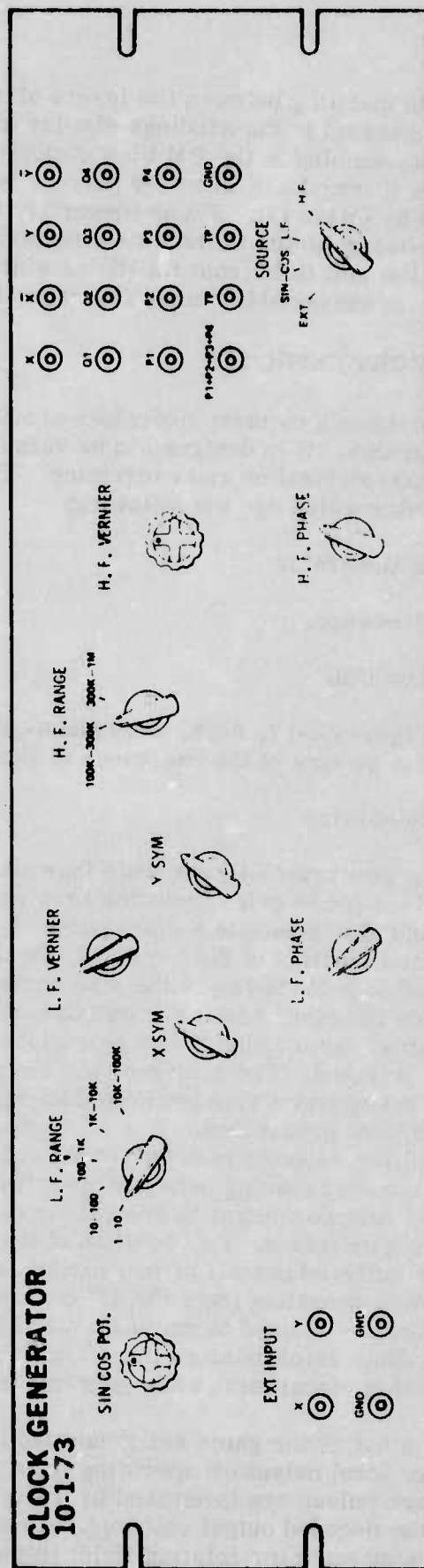


**Figure 6-27. Front Panel Layout of the Clock Generator Bubble Domain Memory Exercisor**



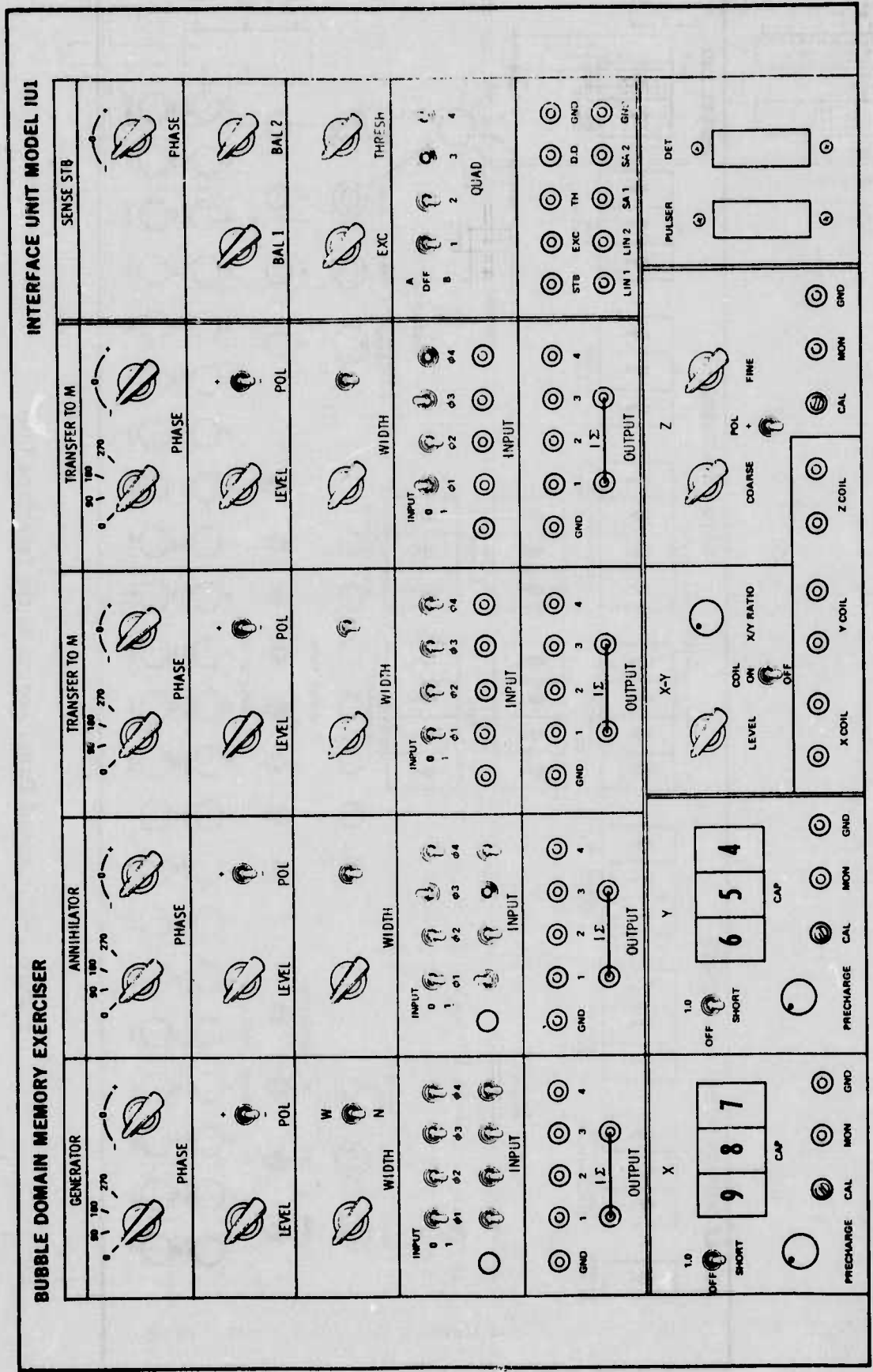


Figure 6-29. Front Panel Layout of the Data Processor Section

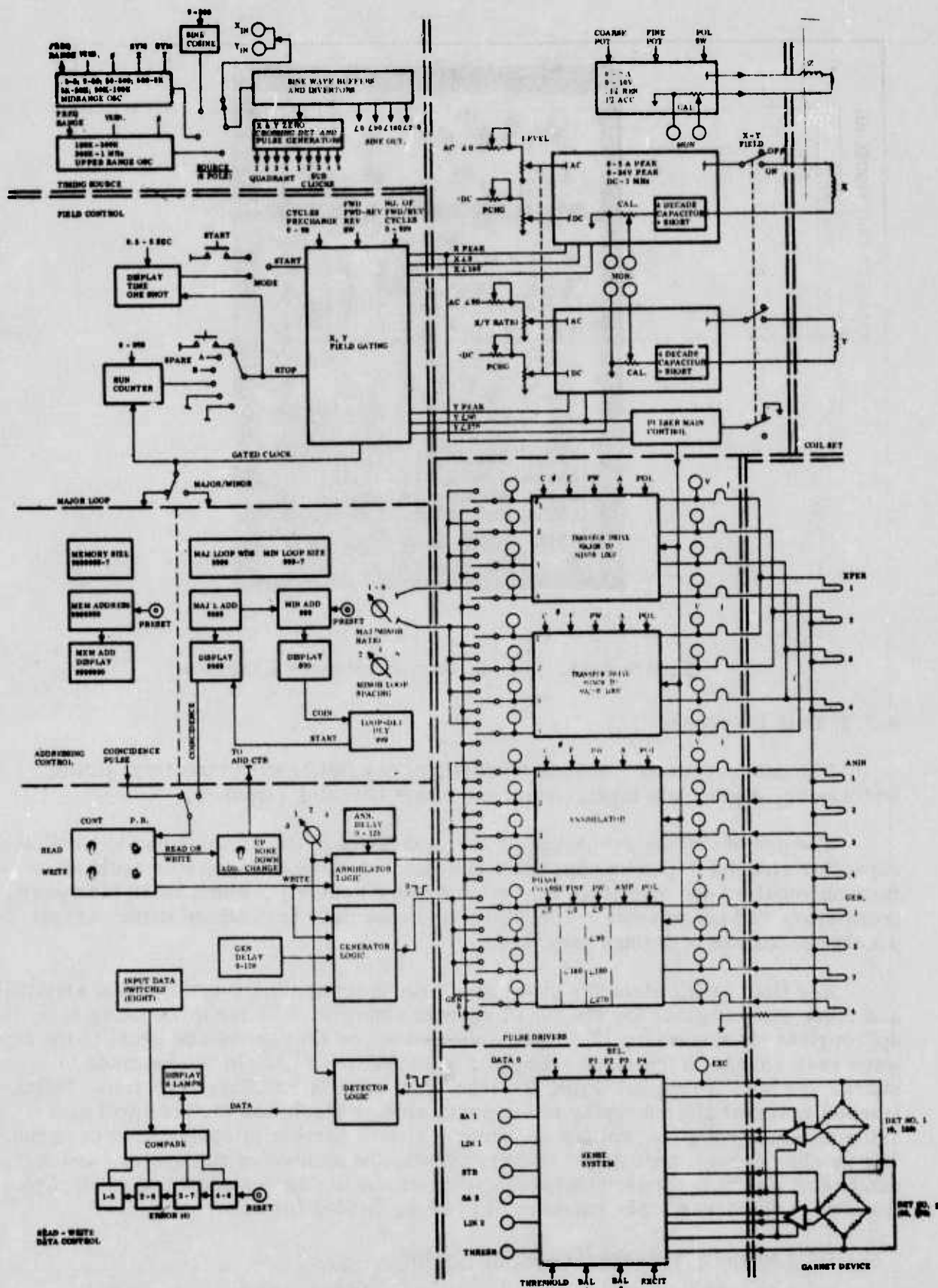


Figure 6-30, Bubble Domain Device Memory Exerciser Block Diagram



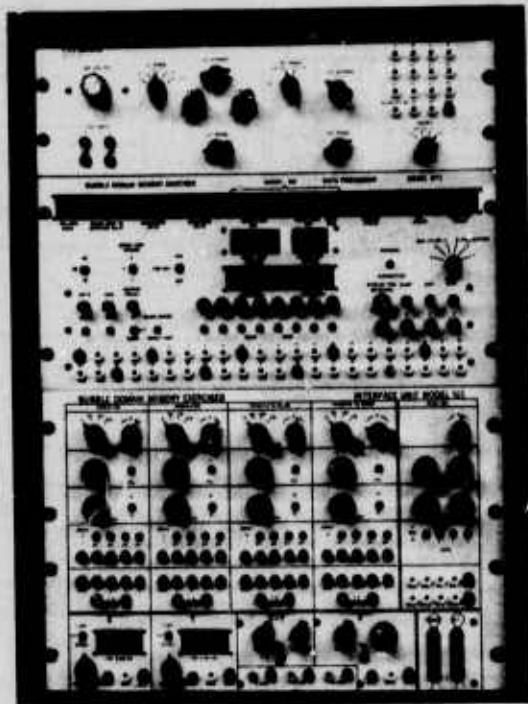


Figure 6-31. Bubble Domain Memory Exercisor

### 6.3.2 Data Processor

The data processor consists basically of x-y field gating circuitry, timing, addressing, digital data input, output and error checking circuitry.

The use of voltage precharge on the capacitors in the series tuned x-y coil and capacitor circuits to provide peak coil current within the first quarter cycle after turn-on requires use of voltage levels (above about 200 kHz) which available power transistors will not tolerate. Therefore, the exercisor is designed using current precharge instead of voltage precharge.

X-y field gating circuitry generates three gates for the x-coil current amplifier and three similar gates for the y-coil current amplifier. These three gates apply the appropriate (1) sine wave, (2) inverted sine wave, or (3) d-c voltage equal to the sine wave peak voltage to the x and y amplifiers so that the x-y field can be made to pre-charge and hold at the peak value and then start rotation in either direction. Instantaneous reversal after stopping at the peak value or discharge to zero level under automatic electronic control can be effected after a number of cycles have been run. The number of precharge and discharge cycles, the number of run cycles, and the number of alternate forward/reverse cycles can be set as desired using control panel thumbwheel switches. The numbers of cycles provided for are:

1. 1 to 100 Precharge/Discharge Cycles
2. 1 to 1000 Run Cycles
3. 1 to 1000 Forward/Reverse Cycles

Forward/reverse control is achieved by selecting the forward, the reverse or the forward/reverse mode. The forward/reverse mode is needed when visual observation of bubble domain propagation is desired for margin characterization of the register performance. The field can be started manually using a start pushbutton, or can be restarted automatically after a panel controlled off time (0.5 to 5 sec) for visual observation of bubble domains. The field can be stopped manually, using a STOP pushbutton or can be stopped automatically after the preset number of RUN cycles or after one cycle through the entire memory register.

The timing and addressing circuitry consists basically of a bit time counter, a word time counter, and address counter, memory size and address coincidence gates and control logic circuitry. The bit time and word time counters count the rotations of the x-y field so that the exerciser maintains synchronism with actual bubble positions. The period of the bit time and word time counters can be set to correspond with the memory track by using the memory size switches. These switches have a capacity for 1 to 9,999,999 eight-bit words, plus one to eight extra bits to provide for registers which are not an even multiple of eight bits.

The address counter can be preset to select any eight-bit word address to be read or written. It can be made to increment up or down (or not increment) each time a word is used, so that an automatic sweep through the memory is possible. The contents of the address counter are displayed on the front panel. Writing or reading of eight-bit words can be done one at a time using the WRITE or READ push-buttons or continually using the CONT. WRITE and/or CONT. READ SWITCHES.

The digital data input, output and error checking circuitries consist of: input, output and shift registers; delay circuits to allow for variations in the relative positions of annihilator, generator and detector on various register designs; and error detector and display circuits. Eight-bit parallel data from control panel toggle switches (or from a connector on the rear of the Data Processor chassis) is parallel loaded into a continually shifting 8-bit input data register each time a write pulse occurs. The memory input data shifted out of this register is distributed, in the Interface Unit, to appropriate bubble memory register chips. The write pulse is delayed by an amount preset in three octal digit control panel thumbwheel switches to allow for the bit distance from the detector to the generator loop. Maximum delay is 177 octal (127 steps). The write pulse is also delayed in a similar set of three octal digit control panel switches to allow for the bit distance from the detector to the annihilator loop. Each of these delayed write pulses generates an annihilator gate which generates eight annihilator pulses in the Interface Unit. Memory output data from the detector amplifier(s) are shifted into another 8-bit register continually and the resulting parallel data are parallel loaded into an output data register each time a delayed read pulse occurs. The contents of the output register are displayed on the control panel by eight binary LED indicators and these data are also available at a connector on the rear of the data processor chassis.

For single phase (single register) operation, the input and output data shift registers step at the field rotation rate. For two-phase (register in each of two quadrants) operation the input and output data shift registers a step at twice the field rotation rate and an 8-bit word consists of four bits from each of two quadrants. For four phase (register in each of four quadrants) operation, the input and output data shift registers step at four times the field rotation rate and an 8-bit word consists of 2-bits from each of four quadrants.

Each time an 8-bit word is read, continuously, the read data are compared, bit-for-bit with that which was written. Error signals set flip-flops which turn on error lights. Four error lights with a common reset are provided to indicate errors in bits 1 or 5, 2 or 6, 3 or 7, and 4 or 8. In the four-phase mode, each error light displays errors from a different quadrant. In the two-phase mode, even bit errors are from one quadrant and odd bit errors are from the opposite quadrant.

### 6.3.3 Interface Unit

The Interface Unit consists of the x-y coil current waveform multiplexers and amplifiers, the annihilator and generator loop current pulse generators and the detector signal amplifiers. In the coil driver section, gate voltages from the Data Processor control the x and y drive amplifiers. The x amplifier selects either; a 90 deg sine wave; a 270 deg sine wave; or a peak d-c voltage. The x and y amplifiers use current feedback to generate x and y coil currents (0 to about 5A peak) proportional to the selected (multiplexed) amplifier inputs. The x-peak and y-peak voltages are derived from x-y gain potentiometers on the same shafts as the potentiometers that the sine waves are obtained from so that peak voltages selected will match the peaks of the sine waves selected at the amplifier inputs.

In the pulse driver section, the Interface Unit generates annihilator and generator loop current pulses for each of four bubble memory register quadrants. The amplitudes, pulsewidths and phase times for each of the eight pulse generators required are controllable from the Interface Unit Control Panel. The memory input data shifted from the Data Processor input shift register are distributed to the four generator loop pulse generators by the clock phase gates from the Timing Generator and by the 1, 2 or 4-phase mode control voltages from the Data Processor turns on the four annihilator pulse generators. Phase times for the pulse generators are derived from level detectors operating from the sine waves from the Timing Generator.

In the sensing section, special detector cards are used for each type of operation. For single-phase operation, the detector element is used in a bridge circuit with a dummy detector element. For two-phase operation, the detector element for the quadrant 1 register is in the same bridge circuit as the detector element for the quadrant 3 register and one preamplifier generates pulses of one polarity for quadrant 2 bubbles. For four-phase operation, a second preamplifier serves quadrants 2 and 4 as the first preamplifier serves quadrants 1 and 3. The Interface Unit provides panel controls for bridge supply voltages, bridge balance voltages and threshold control. The preamplifier typically has a voltage gain of 80. Pulse amplifiers following the preamplifiers raise signals to logic levels. D-c restoration is provided and sampling phase time is controllable from the panel. Detector outputs are combined logically as determined by the 1, 2 or 4-phase mode control and fed to the Data Processor for serial to parallel conversion and transfer to the data output register at the appropriate times.

## SECTION 7

### REFERENCES

1. A. Gangulee, "The Structure of Electroplated and Vapor-Deposited Copper Films," J.A.P. 43 (1972).
2. A. Gangulee, "The Structure of Electroplated and Vapor-Deposited Copper Films, II Effects of Annealing," J.A.P. 43 (1972).
3. A. A. Thiele, "The Theory of Cylindrical Magnetic Domains," BSTJ 48 3287 (1969).
4. R. K. Tenzer, "Temperature Effects on the Remnance of Permanent Magnets," ASD-TDR-63-500 Aeronautical System Division, Air Force Systems Command, Wright-Patterson Air Force Base, Ohio.
5. A. A. Rifkin, "A Practical Approach to Packaging Magnetic Bubble Devices," IEEE Trans Magnetic MAG 9, 429 (1973).
6. P. C. Michaelis and P. I. Bonyhard, "Magnetic Bubble Mass Memory - Module Design and Operation," IEEE Trans Magnetic MAG 9, 436 (1973).
7. G. S. Almasi, W. G. Bouricilus, and W. C. Carter, "Reliability and Organization of a 108-Bit Bubble Domain Memory," AIP Conf Proc., Magnetism and Magnetic Materials - 1971, p 225, Amer. Inst. of Physics, New York, 1972.
8. T. T. Chen, P. K. George, L. R. Tocci, and J. L. Archer, "Study of the Thick Film Chevron Detector," Paper 28-5 presented at the 19th Conf. on Magnetism and Magnetic Materials, Boston 1973.
9. J. L. Archer, L. Tocci, P. K. George and T. T. Chen, "Magnetic Bubble Domain Devices," IEEE Trans on Mag. 8, 695 (1972).
10. L. R. Tocci, P. K. George and J. L. Archer, "High Speed Characteristics of a Chevron Stretcher Detector," AIP Conference Proceedings 10, 197 (1972).
11. A. H. Bobeck, I. Danylchuk, F. C. Rossol and W. Strauss, "Evolution of Bubble Circuits Processed by a Single Mask Level" IEEE Trans on Mag. 9, 474 (1973) (Paper 26.1 Presented with slightly different than published version and described a serial register with the outside corner).
12. W. Strauss, A. H. Bobeck and F. J. Ciak, "Characteristics of a Detection-Propagation Structure for Bubble-Domain Devices," AIP Conference Proceedings 10, 202 (1972).
13. A. H. Bobeck, "Recent Developments in Magnetic Bubble Technology," presented at the National Meeting of the Electrochemical Society, Houston, May 1972.
14. T. T. Chen, P. K. George, L. R. Tocci, and J. L. Archer, "Study of the Thick Film Chevron Detector," Paper 2B-5 Presented at the 19th Conf. on Magnetism and Magnetic Materials, Boston, 1973.
15. A. H. Bobeck, "Recent Developments in Magnetic Bubble Technology," presented at the National Meeting of the Electrochemical Society, Houston, May 1972.



## APPENDIX A

### BUBBLE MATERIAL OVERVIEW

Although bubble materials work was not carried out on this contract, a brief review is included for completeness of the report. This section begins with a discussion of bubble material properties needed to meet the overall goals of this program, followed with a review of current bubble compositions and concluded with comments on the directions of research on bubble materials.

#### A.1 BUBBLE MATERIAL PARAMETERS

The device goals of this program include a bit density of  $1\text{M bit/in.}^2$ , a data rate of 1 MHz, and an operating temperature range of  $25 \pm 50^\circ\text{C}$ .

##### A.1.1 Bit Density

The first goal, a bit density of  $1\text{M bit/in.}^2$ , is realized by  $6\mu\text{m}$  bubbles propagating on a pattern with a  $24\mu\text{m}$  period (P). This bubble size can be produced in most garnet systems by adjustments in magnetization, anisotropy, film thickness and bias field. Thus, bubble size by itself is not a limiting factor but certain device operation constraints make it a little more difficult to attain. For example, a magnetization ( $4\pi\text{M}$ ) of  $\sim 175\text{G}$  is desirable for ease of detection, and the operating margins (separation of bias field values for bubble run-out and collapse) should be as large as possible. From Thiele's theory, the largest margins occur when the bubble diameter is  $8l$  in a film of  $4l$  thickness, where  $l$  is the characteristic length. Thus, from  $\sigma_w = 4\pi M^2 l$ , where  $\sigma_w$  wall energy, a  $6\mu\text{m}$  bubble in a  $3\mu\text{m}$ -thick film with a  $4\pi\text{M}$  of  $175\text{G}$  has a wall energy of  $0.18\text{ erg/cm}^2$ .

##### A.1.2 Data Rate

The second goal, a data rate (S) of 1 MHz, requires a bubble velocity (v) of  $2400\text{ cm/sec}$  from  $v = SP$ . By employing bubble circuits in quadrature, a more realistically attainable v of  $600\text{ cm/sec}$  is required for S of  $250\text{ kHz}$ . From

$v = \frac{\mu_w}{2} (\Delta H - \frac{8}{\pi} H_c)$ , the wall mobility ( $\mu_w$ ) may be estimated for a gradient across a bubble ( $\Delta H$ ) and coercivity ( $H_c$ ). Assuming  $\Delta H$  is  $3\text{ Oe}$  and  $H_c$  is negligibly small,  $\mu_w$  is  $400\text{ cm/sec-Oe}$ . These values for v and  $\mu_w$  are average values; maximum values required by some portions of device circuitry may be twice as large. In addition, at low temperatures  $\mu_w$  decreases and  $H_c$  increases so that for operation over the temperature range, the room temperature  $\mu_w$  should be over two times the average value or about  $1000\text{ cm/sec-Oe}$ .

Anomalous dynamic and static behavior occurs with "hard" bubbles which can introduce errors in the data stream of a bubble device. In particular, these bubbles exhibit lower mobilities than normal bubbles and may propagate at some angle to the gradient field. Also, bubble collapse takes place over a large range of bias fields. These hard bubble properties are attributed to the presence of a number of alternating Neel and Bloch segments in the domain wall. Hard bubble suppression techniques have been developed which involve "capping" the bubble film with another layer so as to limit the number of Neel and Bloch transitions to two. Typically, the cap is produced by ion implantation or an additional garnet or permalloy film.

Another problem in operating a bubble device at a high data rate is dynamic conversion. This term is used to describe the erratic behavior of a bubble driven faster than a critical velocity ( $v_p$ ) which results in the bubble moving either at a reduced velocity or at some angle (other than parallel) to the field gradient. Such behavior may also introduce errors in the data stream of a bubble device. Dynamic conversion is associated with the configuration of the bubble domain wall spin structure but is independent of hard bubble suppression. Since bubble behavior is predictable below  $v_p$ , it is necessary to operate a device at velocities below this value.

### A.1.3 Extended Temperature Range

The next program goal is that of operating over the temperature range of  $25 \pm 50^\circ\text{C}$ . Since the bubble diameter must remain in proportion to the spacing of the propagation pattern for the device to operate, the bubble size must be approximately constant during temperature excursions. The memory will employ a permanent magnet structure to provide the bias field. Inasmuch as both bubble domain material and permanent magnet material properties change with temperature, the temperature coefficients of magnetization of the bubble material and the permanent magnet material must be closely matched over the temperature range.

Another aspect of reliable device operation over the temperature range is that  $\sigma_w$  must be sufficiently great. In instances where  $\sigma_w$  is low, uncontrolled bubble generation and collapse occurs. The problem is prevalent in materials with low values of uniaxial anisotropy and low Neel temperatures.

## A.2 CURRENT BUBBLE COMPOSITIONS

Table A-1 lists bubble compositions which have been considered for use in devices during the past year. The material parameter values listed are typical but may be altered slightly by changes in composition, growth conditions or film thickness. All of these films are nominally  $6\mu\text{m}$  thick with a  $4\pi\text{M}$  of 175G.

Table A-1. Room Temperature Properties of Current Bubble Materials

Nominal Composition	$\mu_w$ cm/sec-Oe	$\sigma_w$ erg/cm <sup>2</sup>	$T_N$ °C	$v_p$ (calc) cm/sec
$\text{Y}_{2.5}\text{Eu}_{0.5}\text{Ga}_{1.1}\text{Fe}_{3.9}\text{O}_{12}$	500	0.17	135	1000
$\text{Y}_{2.1}\text{Eu}_{0.6}\text{Tm}_{0.3}\text{Ga}_{1.1}\text{Fe}_{3.9}\text{O}_{12}$	400	0.18	142	800
$\text{Y}_{1.6}\text{Eu}_{0.8}\text{Tm}_{0.6}\text{Ga}_{1.0}\text{Fe}_{4.0}\text{O}_{12}$	300	0.23	148	900
$\text{Y}_{2.6}\text{Sm}_{0.4}\text{Ga}_{1.2}\text{Fe}_{3.8}$	200	0.17	124	750
$\text{Y}_{1.6}\text{Lu}_{0.3}\text{Eu}_{0.1}\text{Ca}_{1.0}\text{Ge}_{1.0}\text{Fe}_{4.0}\text{O}_{12}$	2500	0.14	183	2300

The first three bubble materials contain Y and Eu with increasing amounts of Eu and Tm. The first compositions with the highest  $\mu_w$ , suffers from a slightly low  $\sigma_w$  and a low (or positive) magnetostriction constant so that hard bubble suppression by ion implantation is not practical. The third composition has the highest  $\sigma_w$  and  $T_N$  of the three and provides relatively stable properties over the temperature range.

The next composition containing Y and Sm has a low  $\sigma_w$  and  $T_N$  so that high temperature operation is limited. The low  $\sigma_w$  also limits operation at low temperatures.

The last composition has been investigated least extensively but its high  $\mu_w$ ,  $T_N$  and  $v_p$  make it quite attractive. The low  $\sigma_w$  may be adequate for high temperature operation as  $T_N$  is so high. This appears to be the only composition in Table A-1 with the potential of meeting all of the material goals.

### A.3 DIRECTION OF RESEARCH AND DEVELOPMENT IN BUBBLE MATERIALS

In order to meet and extend device performance goals, new bubble compositions will continue to be evaluated for higher bit density, higher data rate and extended temperature range. To carry this out, smaller diameter bubbles, higher  $\mu_w$  and  $v_p$ , and higher  $T_N$  will be sought. In addition, hard bubble suppression techniques will be optimized.

Besides improving bubble material properties there will be an effort to reduce chip costs further. This involves the continuing development of procedures for producing numbers of very low defect count films of uniform composition and thickness which have sufficiently similar properties to operate in the same bias field. A necessary requirement is that substrate size increase while substrate crystal quality and surface finish remain at least as good as at present.

## APPENDIX B

### BUBBLE MATERIAL CONSIDERATIONS FOR CONSTANT BUBBLE DIAMETER

Since bubble materials are in general temperature sensitive, bias field compensation techniques (Para 3.2 and 3.3) must be employed to increase the operating temperature range of magnetic bubble devices. The bubble diameter is the only material/device parameter that can be controlled by this technique where it is desired to hold it constant over the operating temperature range. The other parameters such as wall mobility  $\mu_w$ , wall energy  $\sigma_w$ , magnetization  $4\pi M$  and the characteristic length  $l$  are not affected by the bias field variation and are controlled by the material composition alone. In this appendix the material considerations required to maintain a constant bubble diameter using practical bias field variation techniques are discussed. The actual growth and composition requirements of the material are not covered in this appendix.

The starting point is the stability condition for bubble domains

$$\frac{l}{h} + \frac{H}{4\pi M} \left( \frac{d}{h} \right) - F \left( \frac{d}{h} \right) = 0 \quad (B-1)$$

where  $F(d/h)$  is the magnetostatic force function derived by Thiele,<sup>1</sup>  $l$  is the characteristic length, and  $d$  is the domain diameter in a film of thickness  $h$  under a bias field  $H$ . Differentiating with respect to temperature and collecting terms yields

$$\frac{4\pi M}{H(d/h)} \frac{d(l/h)}{dT} + \frac{4\pi M}{H(d/h)} \left\{ \frac{H}{4\pi M} - \frac{dF}{d(d/h)} \right\} \frac{d(d/h)}{dT} + \frac{1}{H} \frac{dH}{dT} - \frac{1}{M} \frac{dM}{dT} = 0 \quad (B-2)$$

The term in braces contains the quantity  $H/4\pi M$  which is greater than the slope of  $F$  in graphical solutions of Eq (B-1) up to the collapse field at which point the quantities become equal. Thus, for bubbles in stable equilibrium, the term in braces is always a positive quantity which will be represented by the symbol  $S$ . Equation (B-2) may now be rewritten using an abbreviated notation for temperature coefficients, e.g.,

$$H_T = \frac{1}{H} \frac{dH}{dT} \text{ and cancelling out the film thickness terms}$$

$$\frac{4\pi M}{Hd} l_T + \frac{4\pi MS}{H} d_T + H_T - M_T = 0. \quad (B-3)$$

Since this relationship contains four temperature coefficients, four cases may be considered for determining the requirements on the behavior: (1) of the bias field, and (2) of the bubble domain material to produce constant bubble diameter during temperature excursions.

<sup>1</sup>A.A. Thiele, "The Theory of Cylindrical Magnetic Domains," B.S.T.J. 48 3287 (1969).



## B.2. CASE I: CONSTANT BIAS FIELD

With a constant bias field, the conditions for a constant bubble diameter are solely dependent on material properties, for  $H_T$  is zero. Thus

$$\frac{4\pi MS}{H} d_T = M_T - \frac{4\pi M}{Hd} l_T. \quad (B-4)$$

Through the characteristic length, the bubble domain diameter is influenced by the wall energy  $\sigma_w$  in addition to the magnetization, as shown by the definition

$$l = \sigma_w / 4\pi M^2. \quad (B-5)$$

Differentiating this expression with respect to temperature and utilizing the abbreviated notation yields

$$l_T = \sigma_{wT} - 2M_T. \quad (B-6)$$

Substitution of (B-6) into (B-4) and collecting terms yields

$$\frac{4\pi MS}{H} d_T = \left(1 + \frac{2\sigma_w}{MHd}\right) M_T - \frac{\sigma_w}{MHd} \sigma_{wT}. \quad (B-7)$$

Since  $\sigma_w = 4(AK_u)^{1/2}$  for 180 deg walls in uniaxial materials,  $\sigma_{wT}$  is negative because both the exchange constant  $A$  and the anisotropy constant  $K_u$  decrease with increasing temperature. The quantities  $\sigma_w$ ,  $M$ ,  $H$  and  $d$  are all positive so that the sign of the temperature dependence of domain diameter is controlled by the  $M_T$  term. Thus:

1. If  $M_T$  is positive or zero,  $d_T$  is positive and the domain diameter will increase with increasing temperature.
2. If  $M_T$  is negative,  $d_T$  can be either positive or negative depending on the relative magnitudes of  $M_T$  and  $\sigma_{wT}$ . The point at which  $d_T = 0$  is given by

$$M_T = \frac{\sigma_w}{MHd + 2\sigma_w} \sigma_{wT}. \quad (B-8)$$

Using typical values of  $\sigma_w = 0.20 \text{ erg/cm}^2$  and  $4\pi M = 175 \text{ gauss}$  in Eq (B-5) yields  $l = 0.82 \text{ } \mu\text{m}$ . For  $d = 8l = 6.6 \text{ } \mu\text{m}$  and  $H = 0.3 (4\pi M) = 52 \text{ Oe}$ , Eq (B-8) reduces to  $M_T \approx 0.23 \sigma_{wT}$ . Assuming a linear decrease in  $\sigma_w$  between 25°C and the Neel temperature of 150°C gives a  $\sigma_{wT}$  of

$$\sigma_{wT} = \frac{1}{\sigma_w} \frac{\Delta \sigma_w}{\Delta T} = \left(\frac{1}{0.20}\right) \left(\frac{-0.20}{125^\circ\text{C}}\right) = -0.80 \text{ Percent/}^\circ\text{C}.$$

The temperature coefficient of magnetization required for constant bubble diameter is thus typically  $M_T = (0.23) (-0.80 \text{ Percent/C}^\circ) = 0.18 \text{ Percent/C}^\circ$ . Hence, for the case of a constant bias field, the magnetization vs temperature characteristic must have a small negative slope if the bubble diameter is to remain reasonably constant.

### B.3 CASE II: CONSTANT CHARACTERISTIC LENGTH

In order for the characteristic length to remain constant with temperature, Eq (B-6) shows that the temperature coefficients of wall energy and magnetization must be related as

$$\sigma_{wT} = 2M_T. \quad (B-9)$$

Since  $\sigma_{wT}$  is always negative, it is obvious that  $M_T$  must also be negative to fulfill the requirements of this Case.

When  $\ell_T$  is zero, Eq (B-3) becomes

$$\frac{4\pi MS}{H} d_T = M_T - H_T. \quad (B-10)$$

In this Case for  $d_T = 0$ , the temperature coefficient of magnetization which is required to meet the condition of Eq (B-9), must be matched by the temperature coefficient of the bias field. Thus, the temperature coefficient of bias field must also be negative.

### B.4 CASE III: CONSTANT MAGNETIZATION

Although the temperature interval over which a bubble material may have a constant magnetization is quite limited, this Case may be of interest in special situations. Thus, for an  $M_T$  of zero, Eq (B-3) becomes

$$\frac{4\pi M \ell}{Hd} \ell_T + \frac{4\pi MS}{H} d_T + H_T = 0. \quad (B-11)$$

For  $d_T = 0$ , the required temperature coefficient of bias field is given by

$$H_T = -\frac{4\pi M \ell}{Hd} \ell_T. \quad (B-12)$$

Using the numerical values employed in Case I gives  $H_T = -0.42 \ell_T$ . From data published by Smith and Anderson<sup>2</sup> on four bubble garnet compositions, in the neighborhood of  $M_T = 0$  values of  $\ell_T$  are found to range from -0.6 to -1.3 Percent/C<sup>o</sup>. Thus, the required bias field behavior in the region of constant magnetization is  $H_T = +0.25$  to  $+0.55 \text{ Percent/C}^\circ$ .

<sup>2</sup>D. H. Smith and W. A. Anderson, AIP Conf. Proc 5, 185 (1972)

## B.5 CASE IV: NONE OF THE VARIABLES HELD CONTANT

The bias field behavior required for constant bubble diameter from Eq (B-3) is given by

$$H_T = M_T - \frac{4\pi M}{Hd} \ell_T. \quad (B-13)$$

Since  $\ell$  is a function of  $M$ , a more explicit relation is obtained by substituting Eq (B-6) into Eq (B-13) to yield

$$H_T = \left(1 + \frac{2\sigma_w}{MHd}\right) M_T - \frac{\sigma_w}{MHd} \sigma_{wT}. \quad (B-14)$$

As before,  $\sigma_w$ ,  $M$ ,  $H$  and  $d$  are positive, while  $\sigma_{wT}$  is negative. Hence the sign of the bias field coefficient required to make  $d_T = 0$  depends on the sign of  $M_T$ . Thus, there are two possible conditions:

1. If  $M_T$  is positive,  $H_T$  must equal the sum of two positive terms.
2. If  $M_T$  is negative,  $H_T$  can be either positive or negative depending on the relative magnitudes of  $M_T$  and  $\sigma_{wT}$ .

Of the four cases presented, Case II in which the characteristic length is held constant is the most desirable for obtaining the widest operating temperature range using bias field variation techniques. Maintaining a constant  $\ell$  results in a temperature independent bubble collapse field  $H_{coll}$ . If the stability margin also remains constant then a constant operating bubble diameter can be maintained without approaching the collapse or stripout points at either temperature extreme. Of course in this case the operating temperature limits will be determined by the bubble mobility (affects data rate) at the low temperature end and the wall energy (affects spontaneous nucleation and stripping) at the upper temperature end.

## APPENDIX C.

### METHOD OF DETERMINING THE MAGNETIC FIELD OF A PARALLEL PLATE STRUCTURE

Standard magnetic circuit mathematical techniques<sup>(1)</sup> are used to solve this structure (Figure C-1). This is not a simple magnetic circuit and approximations given below are used to calculate the permeance  $P$  of the various magnetic paths.

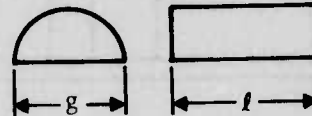
#### Flux Corridor Shapes <sup>(1)</sup>

Semi Circular Cylinder:

$$\langle l \rangle = 1.22g$$

$$\langle A \rangle = 0.322 g$$

$$P = 0.26\mu l$$



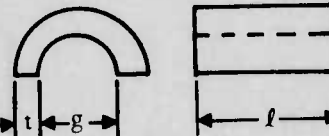
(C-1)

Half Annuli:

$$\langle l \rangle = \pi \left( \frac{g+t}{2} \right)$$

$$\langle A \rangle = t l$$

$$P = 0.64 \frac{\mu l}{g/t + 1}$$



(C-2)

when

$$g < 3t$$

$$P = \frac{\mu l}{\pi} \ln \left( 1 + \frac{2t}{g} \right)$$

(C-3)

Spherical Quadrant:

$$\langle l \rangle = 1.3g$$

$$\langle A \rangle = 0.1g^2$$

$$P = 0.077\mu g$$



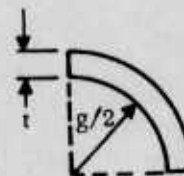
(C-4)

Quadrant of Spherical Shells:

$$\langle l \rangle = \pi/2 (t + g)$$

$$\langle A \rangle = \frac{\pi}{8t} (t + g)$$

$$P = \frac{\mu t}{4}$$



(C-5)

The total flux  $\phi$  from the magnet is equal to the flux in the air gap between the parallel plates

$$B_m A_m = F B_g A_g$$

(C-6)

<sup>(1)</sup>H. C. Roters, Electromagnetic Devices, John Wiley and Sons, New York, 1942



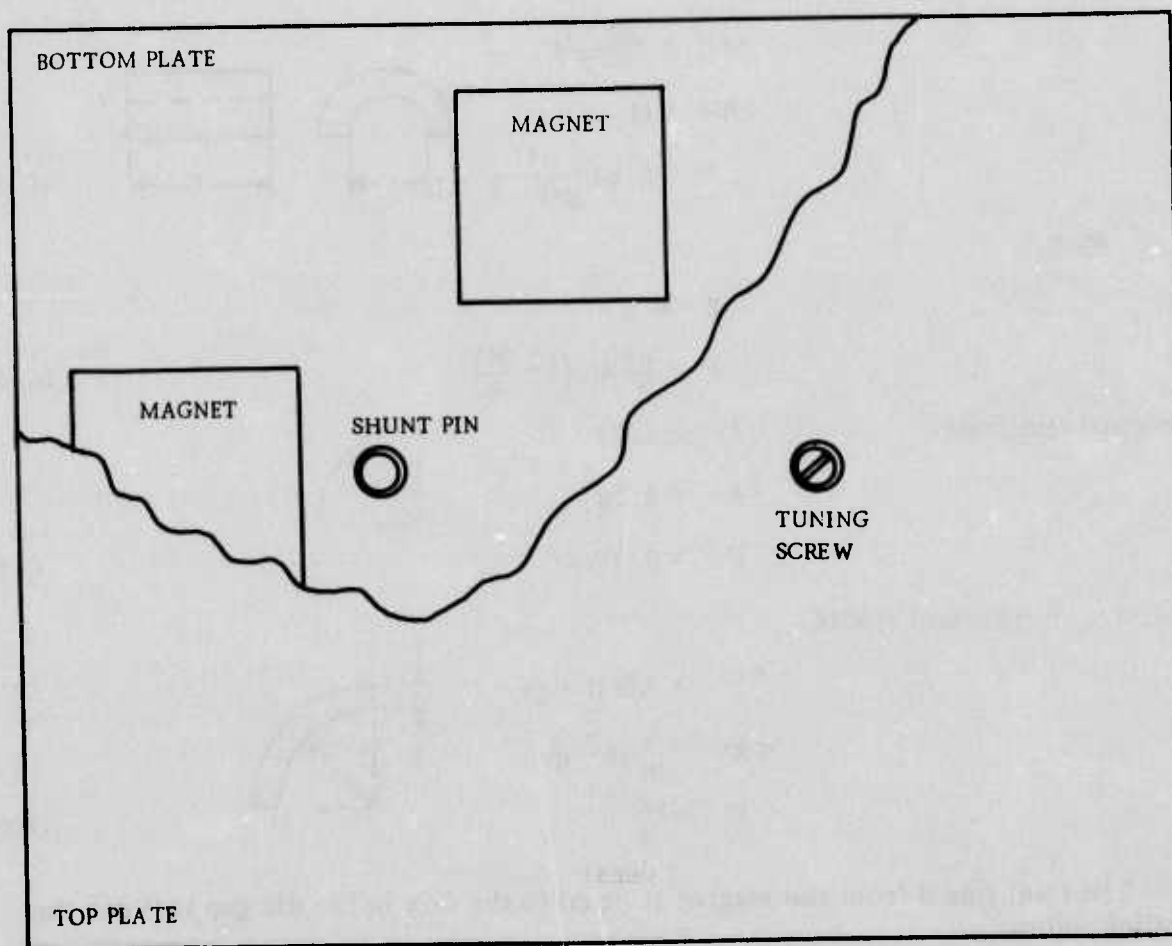
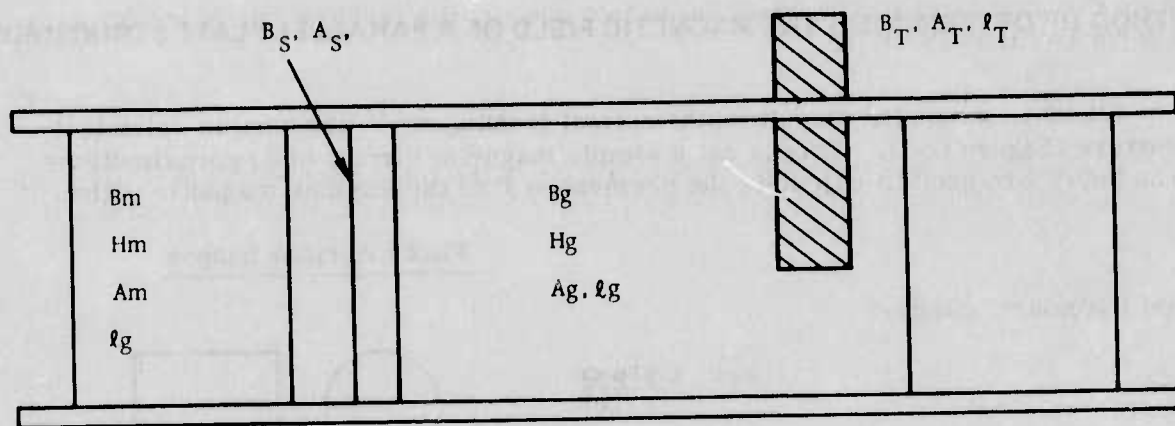


Figure C-1. Parallel Plate Magnetic Circuit with Tuning Screw and Shunt Pin

F in Eq C-6 is a form factor which takes into account the leakage flux of the structure. The form factor is given by

$$F = \frac{P_g}{P_T} \quad (C-7)$$

where  $P_g$  is the permeance of the air gap and  $P_T$  is the total permeance of the structure. The permeance for a simple path (between parallel surfaces) of permeability  $\mu$  and length  $l$  and area  $A$  is given by

$$P = \frac{\mu l}{A} \quad (C-8)$$

Using Eqs (C-1) through (C-5) for the more complex path  $P_g$  and  $P_T$  for the structure can be determined to approximately 10 percent accuracy.

The permeance of the high permeability parallel plates is assumed to be negligible. As long as the plates are not saturated anywhere this assumption is true. The highest flux density in the plates occurs just above the magnets. An estimate of the required thickness can be made by the following equation

$$B = \frac{B_m A_m}{t_p \cdot D} < B_{sat} \quad (C-9)$$

where  $D$  is the perimeter of the magnet and  $t_p$  is the thickness of the plates. Using Gauss' law  $\oint \vec{H} \cdot d\vec{l} = 0$

$$H_m l_m = H_g l_g \quad (C-10)$$

where  $H_m$ ,  $l_m$  and  $H_g$ ,  $l_g$  are the magnetic field and length of the magnet and air gap respectively. Combining Eqs (C-6) and (C-9)

$$\frac{B_m}{H_m} = F \frac{A_g}{A_m} \frac{l_m}{l_g} \quad (C-11)$$

where  $\frac{B_m}{H_m}$  is the effective permeability (or demagnetization factor) for the magnet.

The simultaneous solution of this equation with the demagnetization curve of the magnet (Figure C-2) gives values for  $B_m$  and  $H_m$  respectively. Using these values in Eq (C-6) determines the magnetic field in the air gap  $H_g$ .

Shunt pins which divert flux away from the air gap can be used for coarse tuning. If the pins are saturated when placed between the parallel plates, they essentially subtract from the area of the magnets such that the effective area of the magnets becomes

$$A_m^{eff} = A_m \left( 1 - \frac{B_s}{B_m} \frac{A_s}{A_m} \right) \quad (C-12)$$

where  $B_s$  and  $A_s$  are the saturation flux density and area of the shunt.

Fine tuning can be effected by a high permeability screw. The tuning range can be determined by recalculating  $H_g$  with the screw inserted into the air gap. The total permeance now includes the permeance of the tuning screw so that

$$\Delta H_{tuning} = H_g - H'_g \quad (C-13)$$

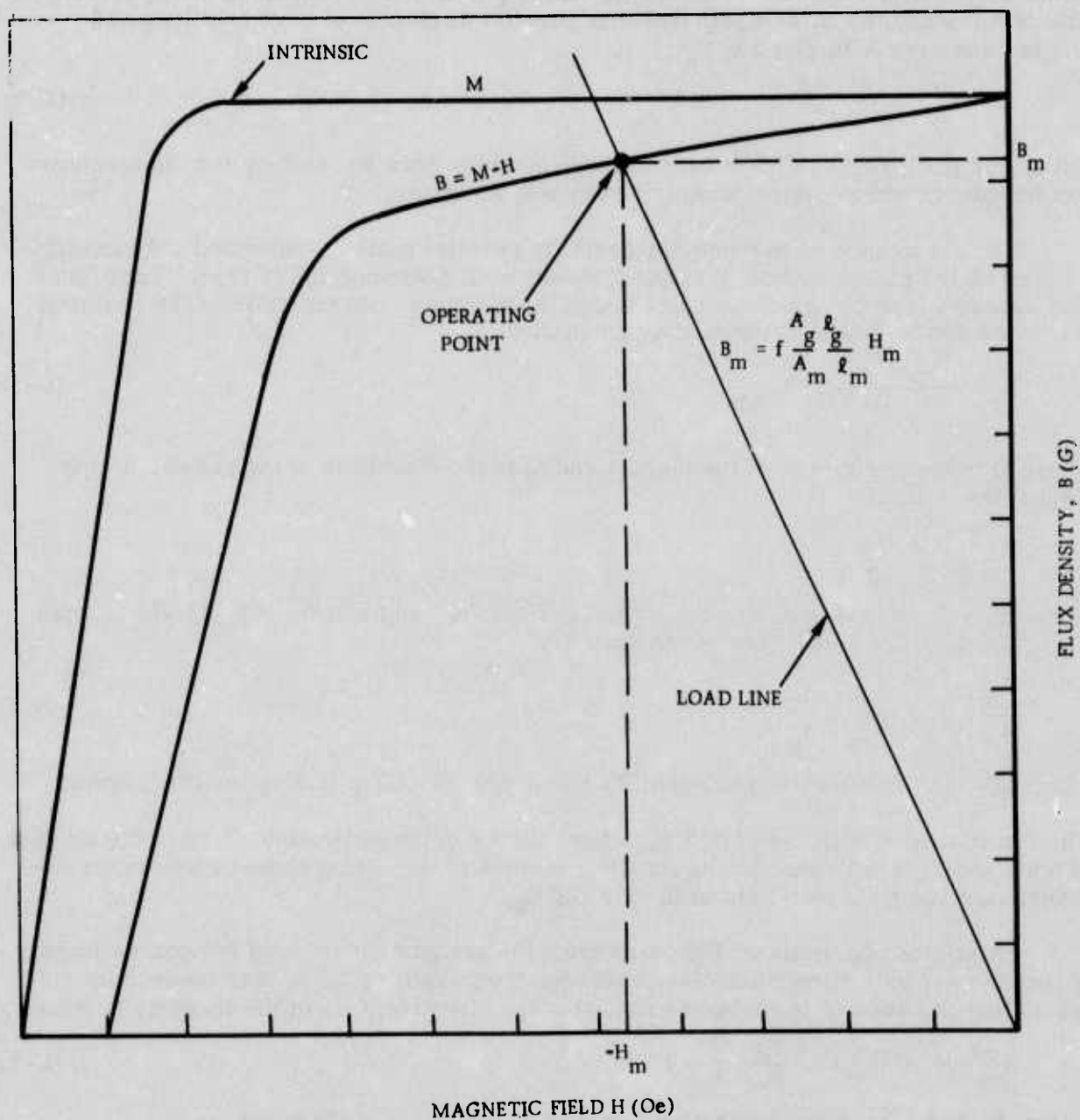


Figure C-2. Typical Permanent Magnet Demagnetization Curve Showing the Load Line

## APPENDIX D

### TEMPERATURE PROPERTIES OF $\text{Y}_{1.7}\text{Tm}_{0.65}\text{Eu}_{0.65}\text{Ga}_{1.06}\text{Fe}_{3.94}\text{O}_{12}$

In this phase of the program the bubble material  $\text{Y}_{1.7}\text{Tm}_{0.65}\text{Eu}_{0.65}\text{Ga}_{1.06}\text{Fe}_{3.94}\text{O}_{12}$  has been chosen to be used for the deliverable magnetic bubble memory devices (Para 6.1). Also the temperature compensated bias structure (Para 3.3 and 6.2) has been designed to match the temperature variation of this material. In this appendix the temperature properties of this material are presented for comparison and completeness; several other bubble materials have been included. A general overview of present bubble materials and their properties is given in Appendix A.

The stability range for a free bubble (not trapped under a permalloy pattern) is shown versus temperature in Figure D-1. The collapse field is not constant with temperature as desired (see Para 3.1 or Appendix B) since the characteristic length  $\ell$  is not temperature independent (Figure D-2). However, for a constant bubble diameter of  $7.5\text{ }\mu\text{m}$  and as long as the mobility permits, there is no problem in operating this material over a temperature range of at least  $0^\circ\text{C}$  to  $70^\circ\text{C}$  because the collapse or stripout regions are not approached too closely. (This particular sample has a strip width a little too large for a  $24\text{ }\mu\text{m}$  pattern.

The variation of the bias field necessary to maintain a constant bubble diameter with temperature is shown in Figure D-3. This information is the most important as far as the temperature compensated bias technique is concerned. The average temperature coefficient of this material is  $-0.99$  percent/ $^\circ\text{C}$  between  $0^\circ\text{C}$  and  $80^\circ\text{C}$ .

The same curve is shown in Figure D-4 for a  $\text{SmYIG}$  material and a  $\text{EuTm}_{.3}$  composition. The  $\text{Sm}$  sample has a temperature coefficient three times that of the  $\text{EuTm}_{.65}$  and would require a different magnet composition (e.g., barium ferrite, Table 3-3) to maintain temperature compensation. The  $\text{EuTm}_{.3}$  temperature coefficient is slightly greater than that of  $\text{EuTm}_{.65}$ ; due partially to the lower bias field required for this particular sample.

The magnetization temperature dependence is shown in Figure D-5. It is smallest for the  $\text{EuTm}_{.65}$  composition.

The bubble velocity versus drive field at three temperature for the  $\text{EuTm}_{.65}$  composition is shown in Figure D-6. Although the mobility for this particular sample is lower than the nominal mobility for this composition ( $\sigma_w \sim 300\text{ cm/sec-Oe}$ ), this sample will apparently operate satisfactorily down to  $0^\circ\text{C}$  at a data rate of  $100\text{ kHz}$  on a  $24\text{ }\mu\text{m}$  pattern if the drive field is  $5\text{ Oe}$  or higher. (It is assumed here that a peak velocity about twice the average velocity of a bubble under these conditions is required). It is estimated from device modeling work being carried out in this laboratory that these drive fields are nominal for field access circuits.

Finally, the wall energy variation is shown in Figure D-7. The wall energy is well above the  $0.1\text{ erg/cm}^2$  lower limit requirement (Para 3.1.1) at  $70^\circ\text{C}$  and thus can be expected to operate satisfactorily up to this temperature limit.



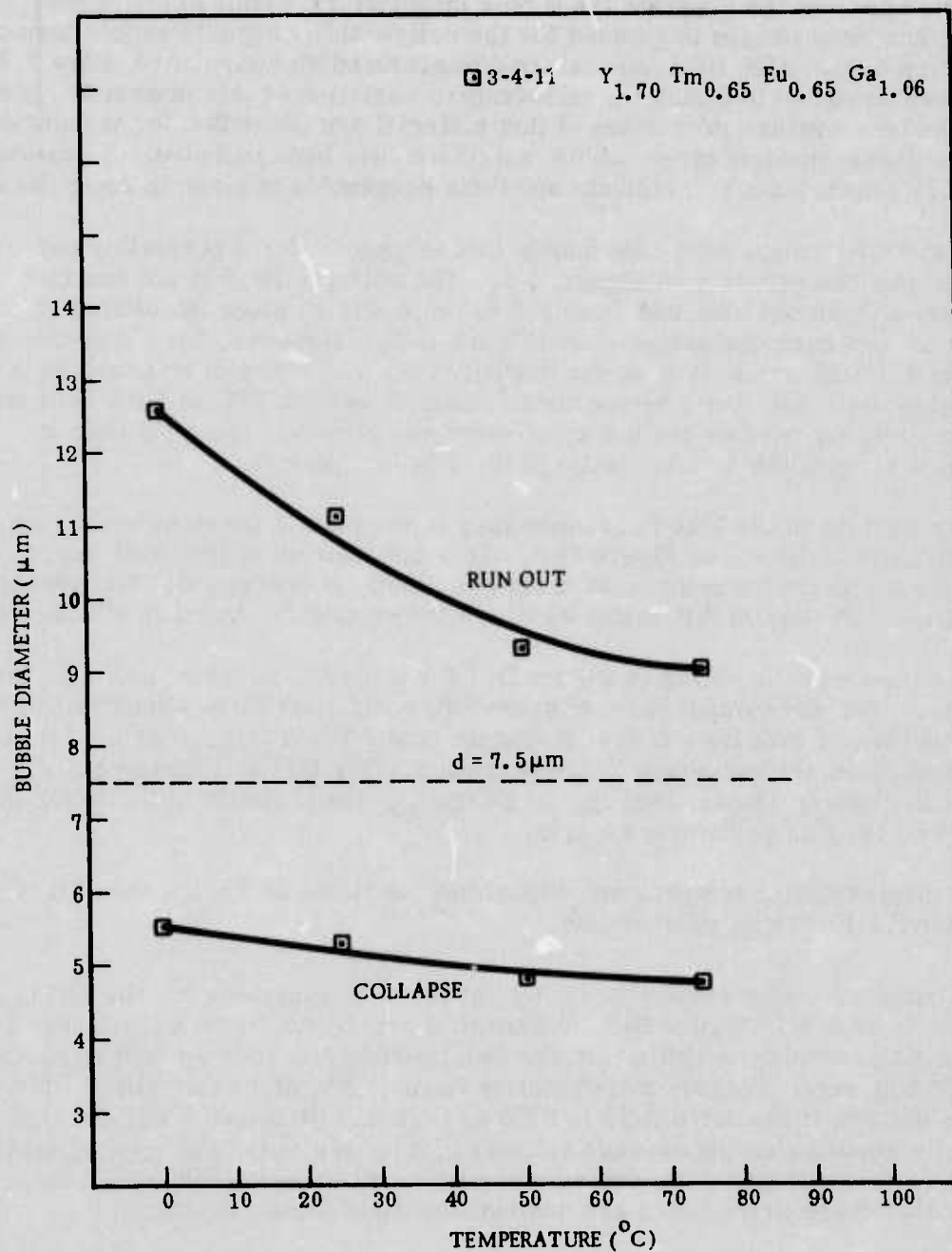


Figure D-1. Bubble Stability Range vs Temperature for EuTm<sub>0.65</sub>

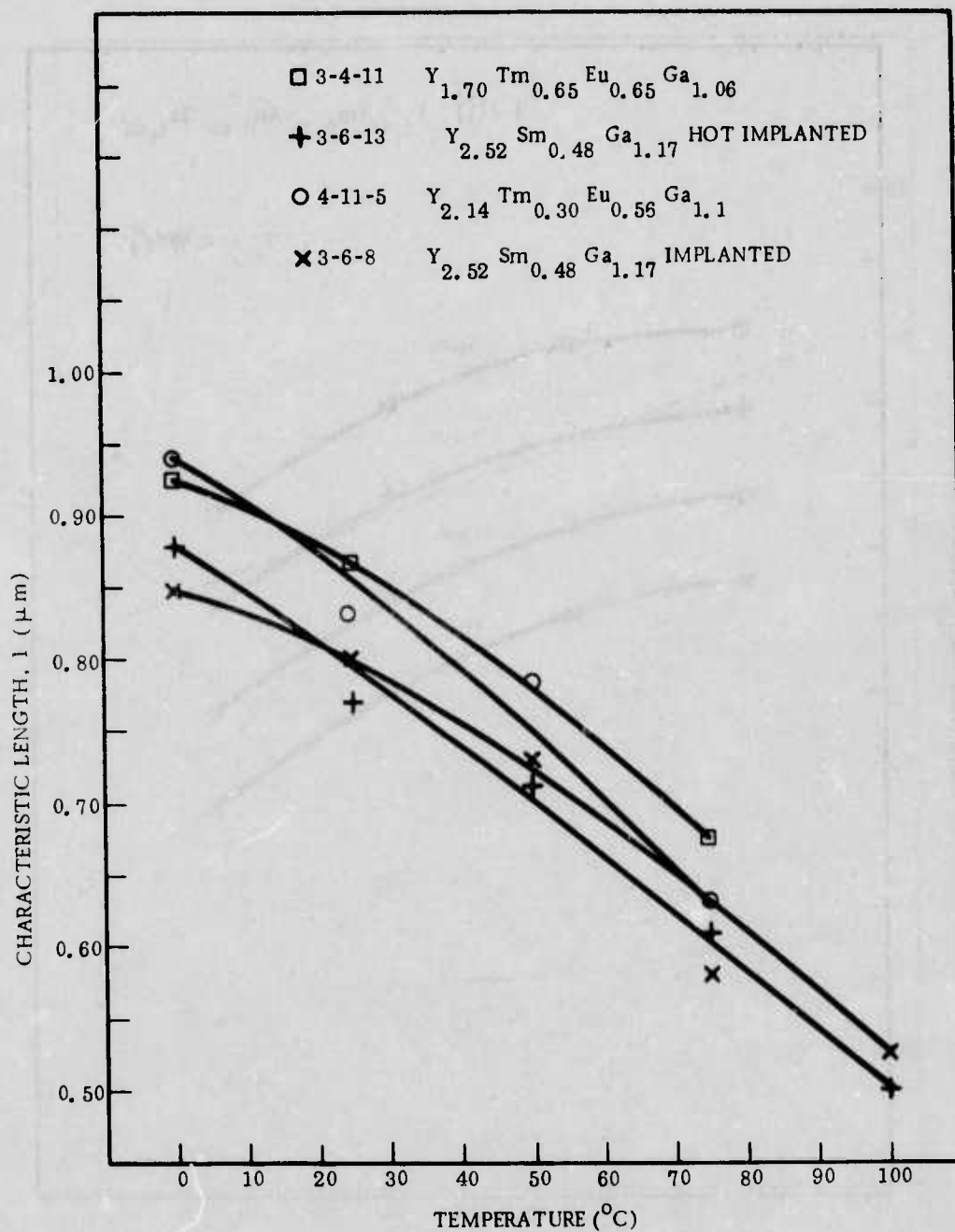


Figure D-2. Characteristic Length vs Temperature

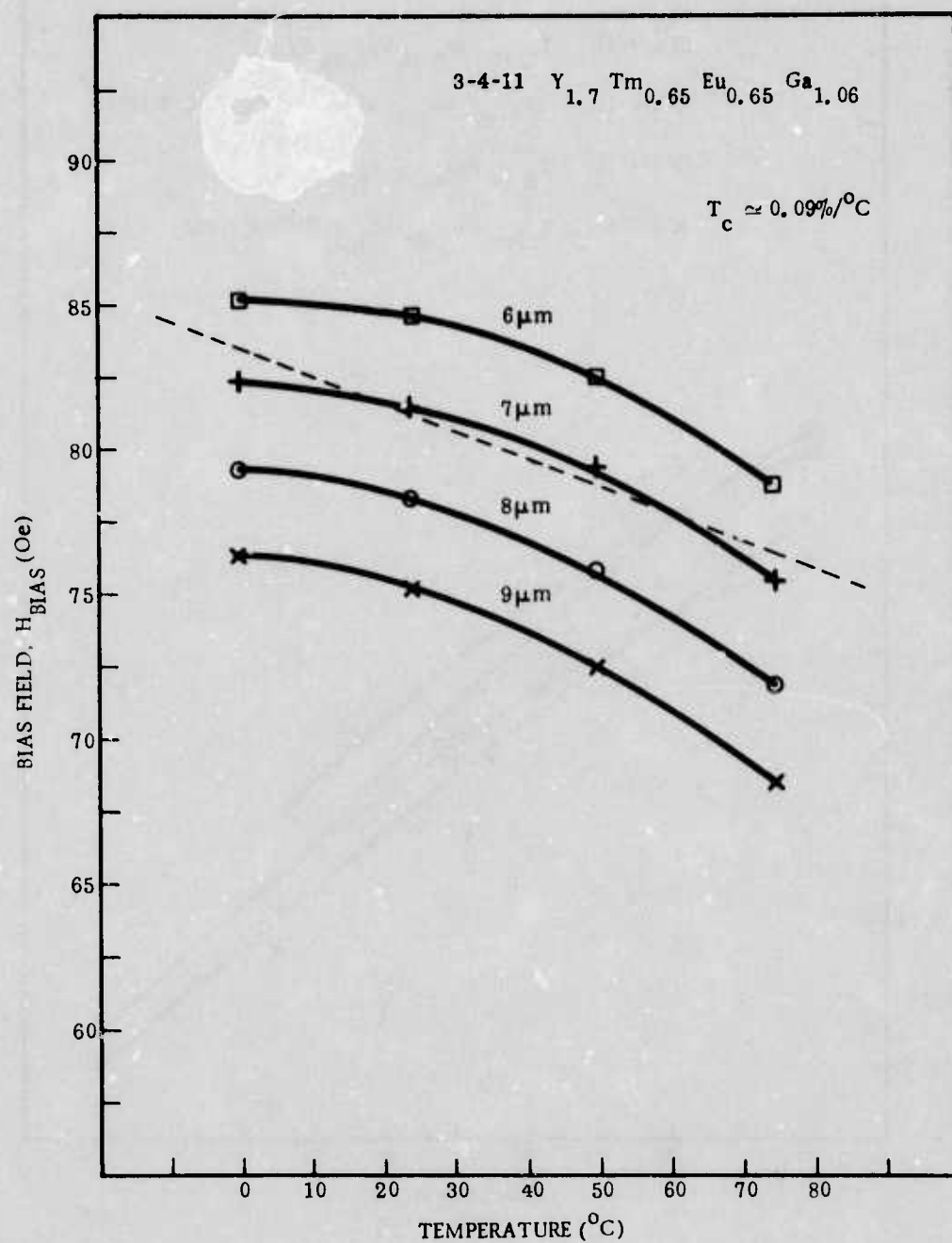


Figure D-3. Bias Field Required to Maintain a Constant Bubble Diameter for  $EuTm_{0.65}$  Composition

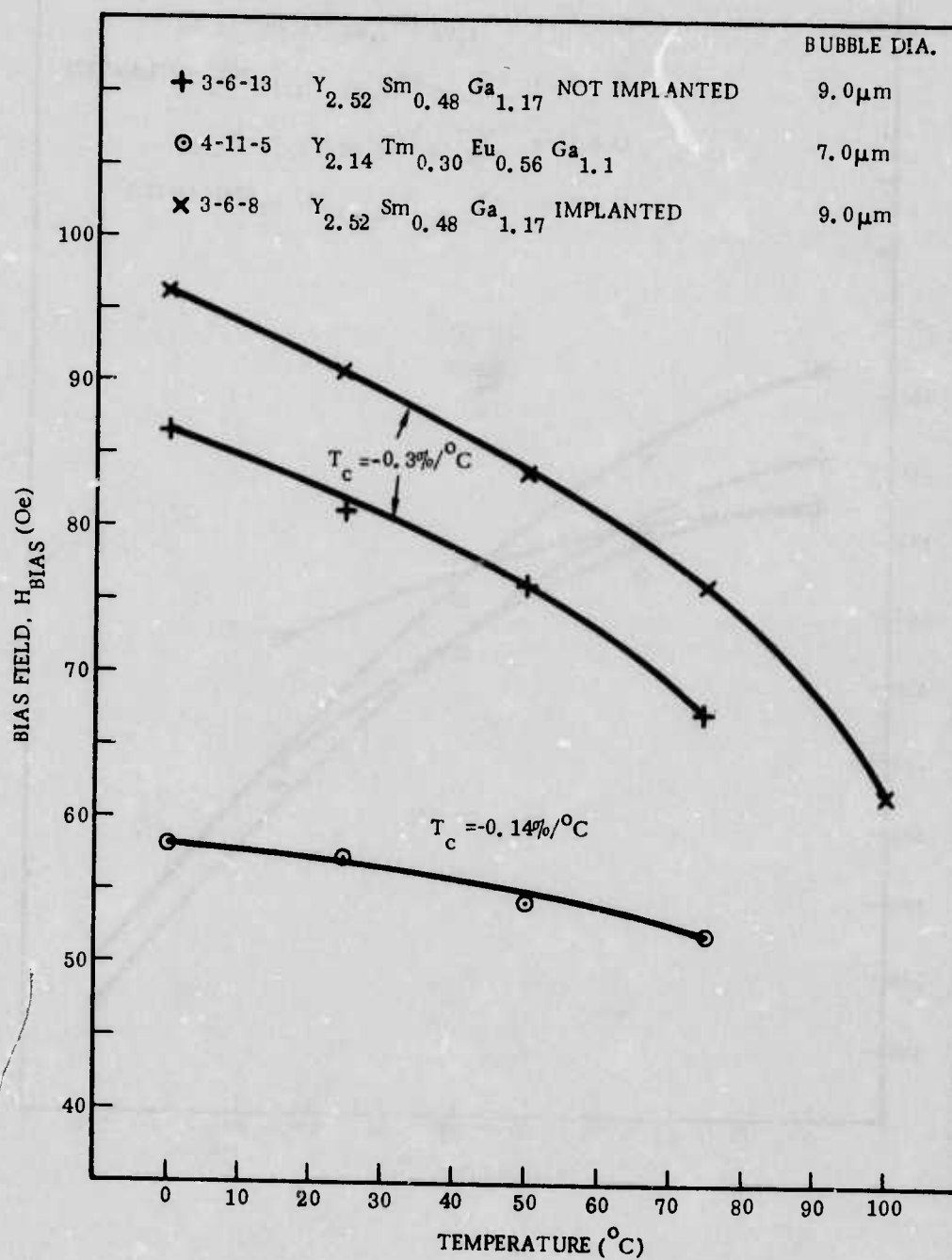


Figure D-4. Bias Field Required to Maintain a Constant Bubble Diameter for SmYIG and EuTm<sub>0.3</sub> Compositions



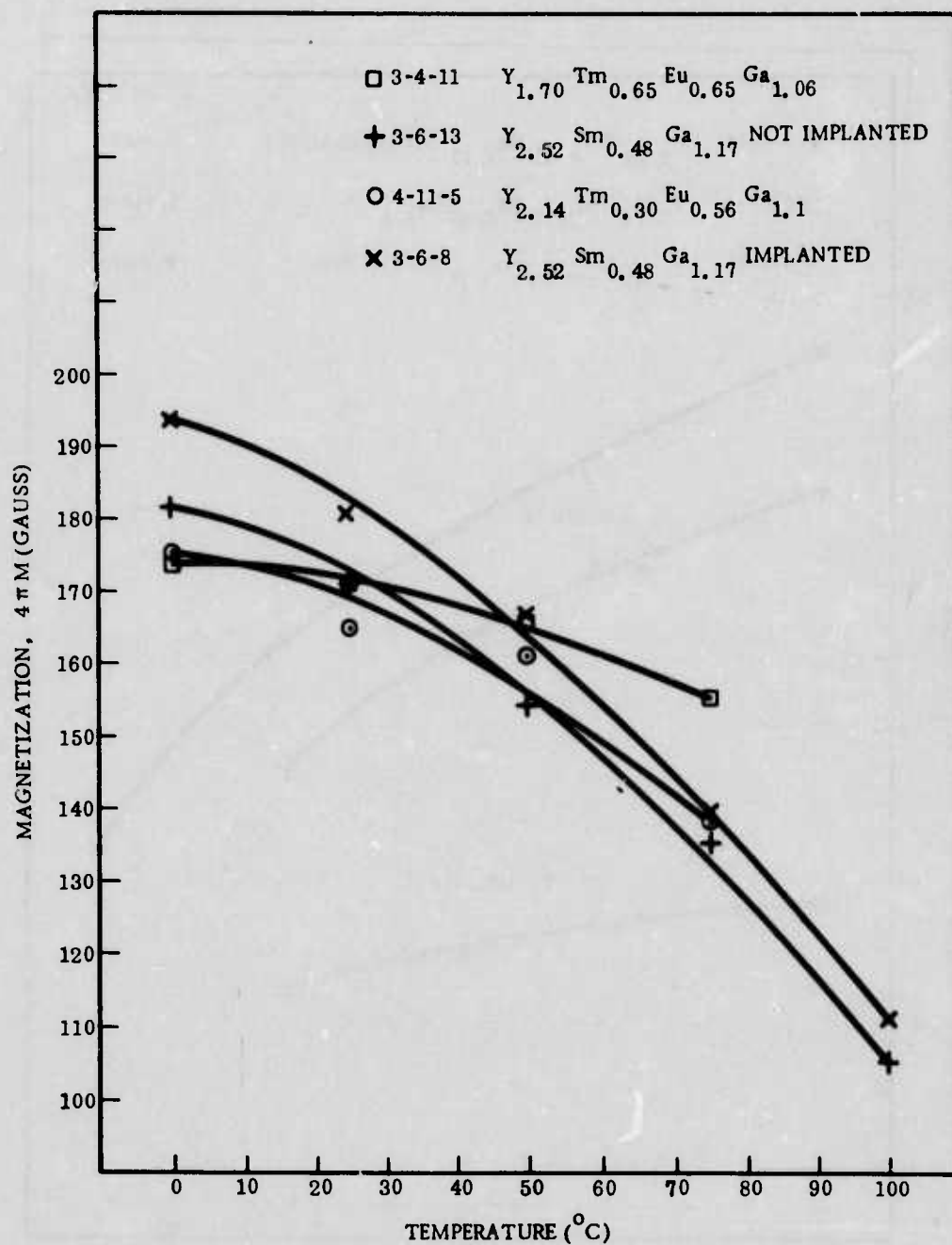


Figure D-5. Magnetization Temperature Dependence

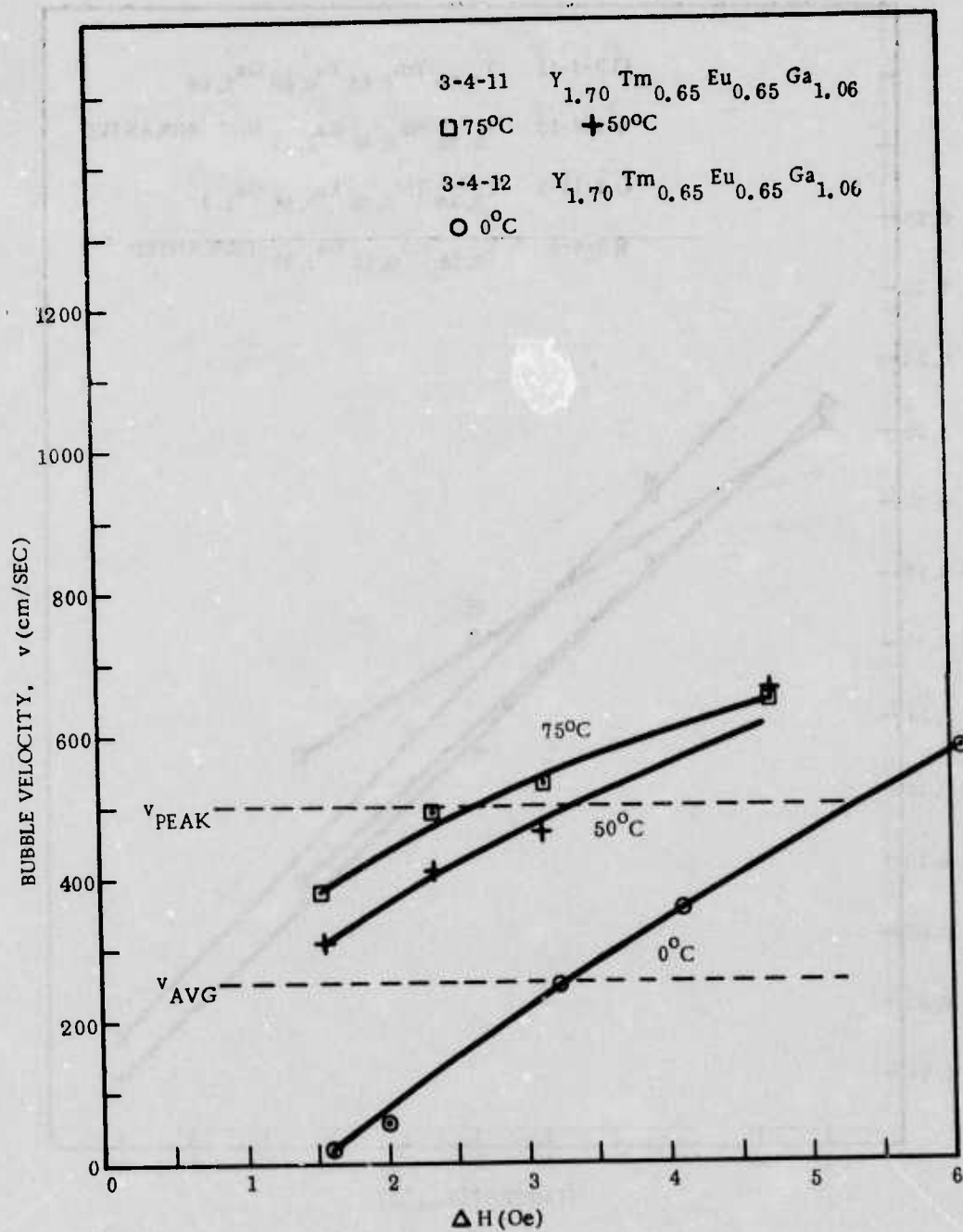


Figure D-6. Bubble Velocity vs Drive for  $EuTm_{0.65}$  at 0°C, 50°C and 75°C

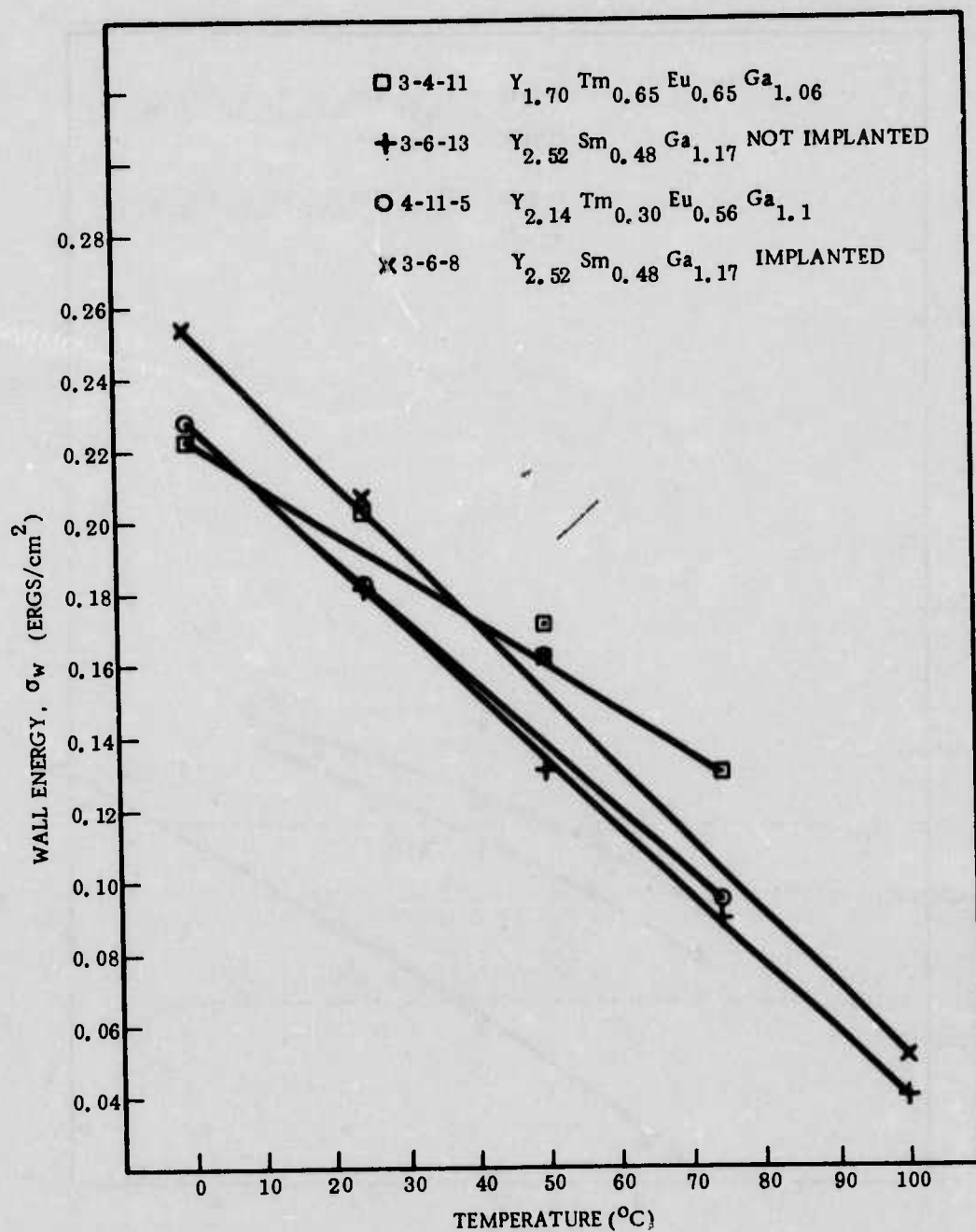


Figure D-7. Wall Energy Temperature Dependence